2017

VALIDATION, OPTIMIZATION, AND IMAGE PROCESSING OF SPIRAL CINE DENSE MAGNETIC RESONANCE IMAGING FOR THE QUANTIFICATION OF LEFT AND RIGHT VENTRICULAR MECHANICS

Gregory J. Wehner
University of Kentucky, wehnergj@gmail.com
Author ORCID Identifier:
https://orcid.org/0000-0003-2983-2524
Digital Object Identifier: https://doi.org/10.13023/ETD.2017.409

STUDENT AGREEMENT:

I represent that my thesis or dissertation and abstract are my original work. Proper attribution has been given to all outside sources. I understand that I am solely responsible for obtaining any needed copyright permissions. I have obtained needed written permission statement(s) from the owner(s) of each third-party copyrighted matter to be included in my work, allowing electronic distribution (if such use is not permitted by the fair use doctrine) which will be submitted to UKnowledge as Additional File.

I hereby grant to The University of Kentucky and its agents the irrevocable, non-exclusive, and royalty-free license to archive and make accessible my work in whole or in part in all forms of media, now or hereafter known. I agree that the document mentioned above may be made available immediately for worldwide access unless an embargo applies.

I retain all other ownership rights to the copyright of my work. I also retain the right to use in future works (such as articles or books) all or part of my work. I understand that I am free to register the copyright to my work.

REVIEW, APPROVAL AND ACCEPTANCE

The document mentioned above has been reviewed and accepted by the student's advisor, on behalf of the advisory committee, and by the Director of Graduate Studies (DGS), on behalf of the program; we verify that this is the final, approved version of the student's thesis including all changes required by the advisory committee. The undersigned agree to abide by the statements above.

Gregory J. Wehner, Student

Dr. Brandon Fornwalt, Major Professor

Dr. Abhijit Patwardhan, Director of Graduate Studies

VALIDATION, OPTIMIZATION, AND IMAGE PROCESSING OF SPIRAL CINE DENSE MAGNETIC RESONANCE IMAGING FOR THE QUANTIFICATION OF LEFT AND RIGHT VENTRICULAR MECHANICS

DISSERTATION

A dissertation submitted in partial fulfillment of the
requirements of the degree of Doctor of Philosophy in the
College of Engineering
at the University of Kentucky

By

Gregory James Wehner

Lexington, Kentucky

Co-Directors: Dr. Brandon Fornwalt, Assistant Professor of Biomedical Engineering
and Dr. Abhijit Patwardhan, Professor of Biomedical Engineering

Lexington, Kentucky

2017

ABSTRACT OF DISSERTATION

VALIDATION, OPTIMIZATION, AND IMAGE PROCESSING OF SPIRAL CINE DENSE MAGNETIC RESONANCE IMAGING FOR THE QUANTIFICATION OF LEFT AND RIGHT VENTRICULAR MECHANICS

Recent evidence suggests that cardiac mechanics (e.g. cardiac strains) are better measures of heart function compared to common clinical metrics like ejection fraction. However, commonly-used parameters of cardiac mechanics remain limited to just a few measurements averaged over the whole left ventricle. We hypothesized that recent advances in cardiac magnetic resonance imaging (MRI) could be extended to provide measures of cardiac mechanics throughout the left and right ventricles (LV and RV, respectively).

Displacement Encoding with Stimulated Echoes (DENSE) is a cardiac MRI technique that has been validated for measuring LV mechanics at a magnetic field strength of 1.5 T but not at higher field strengths such as 3.0 T. However, it is desirable to perform DENSE at 3.0 T, which would yield a better signal to noise ratio for imaging the thin RV wall. Results in Chapter 2 support the hypothesis that DENSE has similar accuracy at 1.5 and 3.0 T.

Compared to standard, clinical cardiac MRI, DENSE requires more expertise to perform and is not as widely used. If accurate mechanics could be measured from standard MRI, the need for DENSE would be reduced. However, results from Chapter 3 support the hypothesis that measured cardiac mechanics from standard MRI do not agree with, and thus cannot be used in place of, measurements from DENSE.

Imaging the thin RV wall with its complex contraction pattern requires both three-dimensional (3D) measures of myocardial motion and higher resolution imaging. Results from Chapter 4 support the hypothesis that a lower displacement-encoding frequency can be used to allow for easier processing of 3D DENSE images. Results from Chapter 5 support the hypothesis that images with higher resolution (decreased blurring) can be achieved by using more spiral interleaves during the DENSE image acquisition.

Finally, processing DENSE images to yield measures of cardiac mechanics in the LV is relatively simple due to the LVs mostly cylindrical geometry. Results from Chapter 6 support the hypothesis that a local coordinate system can be adapted to the geometry of the RV to quantify mechanics in an equivalent manner as the LV.

In summary, cardiac mechanics can now be quantified throughout the left and right ventricles using DENSE cardiac MRI.

KEYWORDS: Magnetic Resonance Imaging, Displacement Encoding with Stimulated Echoes, Cardiac Mechanics

Gregory James Wehner

June 14, 2017
Date

VALIDATION, OPTIMIZATION, AND IMAGE PROCESSING OF SPIRAL CINE DENSE MAGNETIC RESONANCE IMAGING FOR THE QUANTIFICATION OF LEFT AND RIGHT VENTRICULAR MECHANICS

By

Gregory James Wehner

Dr. Brandon Fornwalt, MD, PhD
Co-Director of Dissertation

Dr. Abhijit Patwardhan, PhD
Co-Director of Dissertation

Dr. Abhijit Patwardhan, PhD
Director of Graduate Studies

June 14, 2017
Date

To Eleni

ACKNOWLEDGMENTS

I want to thank my wife, Eleni, for her continuous support and tolerance for the better part of a decade and especially during graduate school. I want to also thank my family for their unending support.

I also want to thank...

1. Brandon Fornwalt for seeking out "quantitative-minded" students, inviting them to a dinner that they couldn't have deserved, and ultimately taking a chance with one of them. I can't think of anyone who has more energy or who is more relentless as a physician scientist. You cannot help but be motivated in his presence. As students, we were encouraged to learn, discover, and push ourselves to think critically and challenge accepted dogma. The road ahead is long, and I am fortunate to have gotten a unique and powerful start.

2. Jonathan Suever for his tireless pursuit of excellence in every project he touches and the many times we were able to work closely together to develop new and more accurate research tools. I am especially thankful for the synergy we had between developing theories of imaging or mechanics and subsequent simulations and experiments to test them, even if others were at best "less excited".

3. Chris Haggerty for always being there to help at any level with any projects from getting me started on my very first imaging project (scanning volunteers at MRISC), to being an effective communicator between me and clinical data scientists, to providing frustratingly good comments and suggestions on presentations/manuscripts.

4. Sean Hamlet for being on this journey with me as a fellow graduate student. I can't imagine going through these four years without your help and support,

even (or especially) if it was just being a good listener as I rattled on for days. I am so grateful that we were both able to finish this small part of our journeys together.

5. David Powell for everything MRI-related from basic theory to sequence optimization, to figuring out what on earth those error messages could possibly mean. None of our MRI work would have been possible without him at the MRISC keeping the system alive. I am very grateful for having him on our team and even more fortunate to have him as a friend.

6. Jonathan Grabau for both his extensive help on multiple projects and for being a great friend. He may have bitten off more than he wanted to by befriending me, but at least I am truly looking forward to the next couple years together as I lean on him during medical school.

7. The remaining Fornwalt lab members both past and present for their guidance and friendliness. As great as Brandon may have been, success would not have been possible without the fantastic atmosphere that everyone created to work within. It was a real blessing to be a part of this wonderful team.

8. Susan Smyth for her outstanding leadership of the MD/PhD program that I am so fortunate to be a part of. As students, we can count on her constant support and passion for having each and every one of us succeed.

9. Therese Stearns for always having her door open and always being willing and able to fight for what her students need. As administrator of the MD/PhD program, we could always count on her regardless of the situation or how frustrated she must have been dealing with all of us.

10. The MD/PhD program students for accepting me as one of their own and being there as friends. I received so much support and advice along the way. I can

only hope that I am passing on fraction of it to others as they join.

11. Darin Cecil and Tanya Graf for all of their help (and it was a lot) in making my trajectory through graduate school possible. Their administrative efforts made it possible for me to continue my work with extremely minimal effort on my part, and it certainly did not have to be that way. I (and my family) are so fortunate to have had them as friends.

12. Moriel Vandsburger for his wide array of advice on topics ranging from MRI expertise to life in general, but also for his leadership and support that made my graduate school trajectory possible. I am lucky to have had him as a friend and I look forward to when our paths cross again.

13. Abhijit Patwardhan for his leadership as DGS of the BME department, for his service as co-chair of my graduate committee, but mostly for being someone I could always turn to for advice as the trajectory of my graduate school career played out. In addition, I am especially thankful for his Signal Processing course, which opened my eyes to a real problem I was having in my imaging data and led to a new and successfully completed project.

14. The BME program including the students and administrators for welcoming me and fostering a professional and fun environment. Now that I am at the end, I'm sad to think about missing the Friday afternoon seminars.

15. Vince Sorrel and Steve Leung for their clinical cardiac imaging expertise and strong support of clinical research at the Gill Imaging Center. I was fortunate to have them in my corner during graduate school and I look forward to learning more from them in medical school.

16. Fred Epstein and Xiaodong Zhong for their unending support and development of MRI solutions and their guidance as we adopted them. Without their efforts,

my projects simply would not have existed.

17. Jonathan Wenk for both his expertise in deformation mechanics and for being a great friend. I have been lucky to have him as I journeyed through the realm of cardiac mechanics and was fortunate to collaborate on multiple projects that combined cardiac imaging and mechanical properties.

18. Les Kirchner, Neil Manus, and Joe Leader for their data science support at the Geisinger Health System. I learned a great deal about clinical data and was extremely fortunate to have so much support (and so much data!) available at the click of a button.

19. Christopher Good for his clinical echocardiography expertise. As I started to dive into the realms of clinical cardiac imaging, I was fortunate to have him to turn to as I inevitably ran into questions about the definitions and clinical significance of various echocardiographic terms.

TABLE OF CONTENTS

LIST OF TABLES

LIST OF FIGURES

CHAPTER 1

BACKGROUND

1.1 Heart Disease

Heart disease is both highly prevalent and a leading cause of death worldwide. In patients with known or suspected heart disease, left ventricular ejection fraction (LVEF) has historically been the most common metric of cardiac function.[1] LVEF is the percentage of blood that is ejected from the left ventricle during each heartbeat, and is easy to measure from cardiac imaging such as echocardiography and magnetic resonance imaging (MRI). Importantly, while LVEF is associated with mortality [1], experts recognize that LVEF is largely a measure of convenience, and thus, more advanced quantifications have long been desired. Specifically, LVEF is a global measure of left ventricular function. It is expected that probing the regional function of the cardiac tissue, rather than the bulk flow of blood, would provide a more sensitive measure of heart function.

1.2 Advanced Measures of Heart Function: Cardiac Mechanics

Starting in the 1980s, new imaging technology aimed to develop more sensitive measures of cardiac function based on quantifying the relative shortening or lengthening (strain) and twisting or torsion of the cardiac tissue at a regional level.[2] These measures were made possible due to advances in both image acquisition and image post-processing technology. Since then, thousands of studies have reported on the merits of strain for both distinguishing between categories of patients and predicting patient outcomes. A systematic review and meta-analysis comparing the prognostic implications of strain and LVEF demonstrated that a particular strain metric, global longitudinal strain (GLS), is more closely related to mortality than LVEF.[3] The results from one such study are typical of the rest and

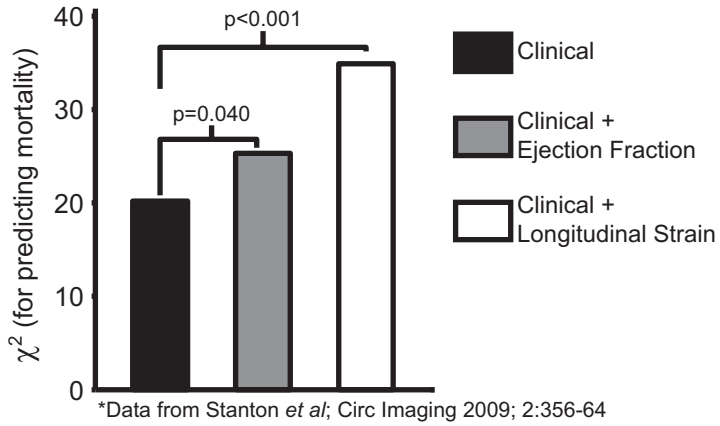

Figure 1.1: Measuring cardiac strains dramatically improves the ability to predict mortality.

showed that the ability to predict mortality is significantly higher when using GLS (Figure 1.1).[4]

However, GLS is similar to LVEF in that it is a global measure of function due to averaging the longitudinal strain values across all cardiac regions. Indeed, most studies of cardiac mechanics have focused on such global measures largely because averaging smooths over noise in the measurements while providing an easily comprehensible single number. In addition, few studies have considered the right ventricle (RV), which is difficult to image due to its thin wall and irregular geometry relative to the LV, which is readily modeled as a prolate spheroid. Fortunately, recently developed MRI technology has shown promise for accurately measuring regional LV mechanics, and it may be extensible for measuring the same metrics in the RV.

1.3 Displacement-Encoded Cardiac MRI

MRI uses large magnetic fields and non-ionizing radio waves to generate medical images. Due to the unique physics of MRI compared to other imaging modalities (*e.g.* ultrasound, radiography, computed tomography), it is well-known for producing anatomical images with high contrast between different tissues and

pathologies. However, the same underlying principles also allow MRI to generate images that contain information beyond gross anatomy. In particular, displacement-encoded MRI is a technology whereby the intensity of the image (*i.e.* the brightness or darkness) is directly related to tissue motion.[5] This provides the exact motion information that is needed to calculate cardiac mechanics.

Spiral cine Displacement ENcoding with Stimulated Echoes (DENSE) is the latest implementation of displacement-encoded MRI, and it operates by directly encoding the displacement of the myocardial tissue into the phase of the resulting images.[6] Important features of spiral cine DENSE include high spatial and temporal resolutions, high signal-to-noise ratio (SNR), and the ability to make complete three-dimensional (3D) measurements of tissue displacement. Spiral cine DENSE has been validated and used often for studies of LV function.[7, 8] Limited studies of the RV suggest the potential for fully extending the acquisition and post-processing of spiral cine DENSE to quantify mechanics throughout both ventricles.[9]

1.4 The Need for Quantifying Right Ventricular Mechanics

Many studies have used LV mechanics to characterize different disease states, and a subset have demonstrated the added value that LV mechanics provide beyond traditional clinical measures.[3] However, the role of RV mechanics is less clear despite the existence of many RV pathologies such as arrhythmogenic right ventricular cardiomyopathy (ARVC), RV hypertrophy, pulmonary hypertension, and congenital heart disease. Given the insight and added value that LV mechanics have contributed, it is likely that similarly useful information is stored within RV mechanics. In particular, these sensitive measures of RV function may provide better insight into disease progression and may allow for early detection of subclinical phenotypes.

The inherent advantages of spiral cine DENSE can likely be harnessed to overcome

the difficulties of measuring RV mechanics. The thin RV wall requires both high spatial resolution and high SNR, both of which spiral cine DENSE provides. Similarly, the complex shape and motion of the RV precludes standard two-dimensional (2D) analyses and requires complete 3D measurements of displacement, which is well-supported by spiral cine DENSE.[6, 10]

1.5 Specific Aims

Despite the inherent advantages of spiral cine DENSE, several extensions are required before the goal of reliably quantifying mechanics throughout both the LV and RV can be realized. These extensions were performed via the following specific aims.

1. **Compare mechanics derived from spiral cine DENSE to those derived from standard clinical imaging.** While spiral cine DENSE is recognized as a gold-standard measure of cardiac motion and mechanics, commercial software exists to estimate those measures from standard clinical MRI, which is widespread and requires less expertise to perform. Analyses were performed on 89 volunteers with both spiral cine DENSE and standard clinical MRI. *Successful completion of this aim demonstrated that estimated mechanics from standard clinical MRI do not agree with, and thus cannot be used in place of, mechanics from spiral cine DENSE.*

2. **Validate the accuracy of spiral cine DENSE at 3.0 T.** While spiral cine DENSE has been well-validated at a magnetic field strength of 1.5 T, imaging at 3.0 T would provide better SNR, which would be advantageous for imaging the thin RV wall. Analyses were performed on ten healthy subjects at both field strengths. *Successful completion of this aim demonstrated that spiral cine DENSE has similar accuracy at both 1.5 and 3.0 T.*

3. **Determine the appropriate value for the spiral cine DENSE**

displacement encoding frequency. The displacement encoding frequency is primarily responsible for linking the amount of tissue displacement to the intensity of the acquired phase images. However, it also contributes to other image characteristics that affect their ability to be analyzed. Most studies have used a value of 0.10 cycles/mm, however, different values have not been formally investigated. Analyses were performed on 20 volunteers using a range of spiral cine DENSE displacement encoding frequencies. *Successful completion of this aim demonstrated that the displacement encoding frequency could be as low as 0.04 cycles/mm to yield improved image characteristics without compromising the quantification of cardiac mechanics.*

4. **Determine the effect of the number of spiral interleaves and the spiral readout duration on image quality and measured mechanics.** Spiral MRI techniques are prone to blurring when the readout duration is too long, which effectively reduces spatial resolution and may impact measured cardiac mechanics. Increasing the number of spiral interleaves can reduce the readout duration at the expense of increased total scan time. Both simulations and volunteer imaging (five healthy volunteers at both 1.5 T and 3.0 T) were performed with several different readout durations. *Successful completion of this aim demonstrated that spiral cine DENSE image quality and measured cardiac mechanics are dependent on the spiral readout duration due to blurring with longer readout durations.*

5. **Develop and evaluate a single post-processing pipeline to quantify mechanics from both the LV and RV.** Due to the regular shape of the LV, it is common to quantify mechanics in circumferential, longitudinal, and radial directions. An equivalent representation is desirable for the RV despite its complex geometry. A flexible pipeline was made by incorporating a local

coordinate system fit to extracted ventricular surfaces and a regional parameterization that did not require or assume any particular geometric form. Analyses were performed on 50 healthy volunteers. *Successful completion of this aim demonstrated that 3D spiral cine DENSE along with a flexible post-processing pipeline can be used to quantify cardiac mechanics throughout the LV and RV.*

CHAPTER 2

COMPARISON OF LEFT VENTRICULAR STRAINS AND TORSION DERIVED FROM FEATURE TRACKING AND DENSE CARDIAC MRI

2.1 Background

Myocardial mechanics, such as strain and torsion, are important indicators of cardiac function and independent predictors of serious cardiac outcomes, even when accounting for traditional measures such as ejection fraction.[4, 11] Several advanced cardiac magnetic resonance (CMR) sequences have been developed to assess myocardial mechanics including tagging,[2, 12] displacement encoding with stimulated echoes (DENSE),[5, 13, 6] strain encoding (SENC),[14] and tissue velocity phase mapping (TPM).[15] While these techniques can provide gold standard measurements of myocardial motion and deformation, their use has traditionally been clinically impractical. Furthermore, exclusive focus on these new methods does not leverage the availability of historical clinical imaging data that - if tied to patient outcomes - could produce additional novel insights into the prognostic value of these measurements. As such, there has been growing interest in the use of feature tracking software to approximate the mechanics produced by gold standard techniques.[16, 17, 18] While feature tracking is simple to use and requires only standard anatomical cine sequences that are widely available, it is crucial to assess how well measures of cardiac mechanics such as strain and torsion derived from feature tracking agree with those derived from the gold standard techniques.

While results from feature tracking have been compared to those from tissue tagging [16, 19, 20, 21, 22] and TPM,[23] many of these validation studies have been limited in scope. The largest study,[16] with 191 Duchennes Muscular Dystrophy

patients and 42 healthy controls, surveyed only mid-ventricular short-axis images, while studies with a wider focus have had limited sample sizes (n = 18 [22], n = 20 [19]). Additionally, none of the validation studies have been performed with DENSE, which directly encodes displacement into the phase of the MR signal.[5] This allows displacement to be measured at the pixel-level with high spatial resolution. Several advancements in DENSE acquisition since its introduction, such as CSPAMM artifact suppression [13] and efficient spiral readouts [6], make it an ideal technique for gold standard measurements of myocardial motion and deformation.

Additionally, in a review of the literature including 65 feature tracking studies, slice-wise strains (i.e. the average strain over an entire image slice) are the most commonly reported measures derived from feature tracking (Table 2.1). However, slice-wise strains, which are reflective of the change in length of an entire contour, should not require segmental motion tracking.[24] This suggests that the most commonly reported results from feature tracking could be easily assessed without performing tracking by simply using the two end-diastolic and end-systolic endocardial contours which are already generated during the analysis of most clinical CMR scans.

We hypothesized that left ventricular strains and torsion derived from feature tracking would not agree well with those derived from DENSE. We also hypothesized that slice-wise strains from measuring the change in length between the end-diastolic and end-systolic contours (contour-based strains) agree well with strains reported by feature tracking.

2.2 Methods

2.2.1 Study Population

We reviewed our database of CMR datasets that were acquired from 2013 to 2016 at two institutions (University of Kentucky and the Childrens Hospital of

Table 2.1: Reported mechanics from 65 feature tracking studies

	Number of Studies
Mechanics	
Circumferential Strain (slice-wise)	36
Longitudinal Strain (slice-wise)	28
Radial Strain (slice-wise)	21
Circumferential Strain (segmental)	18
Longitudinal Strain (segmental)	12
Radial Strain (segmental)	12
Systolic Strain Rate	5
Diastolic Strain Rate	6
Torsion	8
Torsion Rate	5
Synchrony	6
Atrial Strain	8
Right Ventricular Strain - any	13
Right Ventricular Strain - segmental	7
Other*	3

*Feature Tracking in non-MRI modality

Philadelphia) for all instances where both spiral cine DENSE and steady state free precession (SSFP) were acquired at the same slice location in basal, mid-ventricular, and apical short-axis image planes and in the four-chamber image plane. The studies were approved by the local IRBs and all participants gave informed consent. During the review, no exclusions for diagnosis or the presence of cardiovascular risk factors were applied.

2.2.2 Image Acquisition

All datasets from the University of Kentucky were acquired on a 3.0 T Siemens Trio (Erlangen, Germany) while datasets from the Childrens Hospital of Philadelphia were acquired on a 1.5 T Siemens Avanto. Spiral cine DENSE images with displacements encoded in at least the two in-plane dimensions were acquired with an established spiral sequence [6, 8, 7] using the following parameters: 6 spiral interleaves with 2 spiral interleaves acquired per temporal frame, 250x250 to 360x360 mm^2 field of view, 128x128 image matrix, 1.95x1.95 to 2.81x2.81 mm^2 pixel size, 8 mm slice thickness, 1.08 ms echo time, 15 to 17 ms repetition time. Simple or balanced encoding [25] with an encoding frequency between 0.04 and 0.10 cycles/mm [26] was used to measure in-plane displacements, while through-plane dephasing [27] and CSPAMM [13] were used for echo suppression. Cine SSFP images were acquired at the same locations as the DENSE images using the following parameters: 1.15x1.15 to 1.77x1.77 mm^2 pixel size, 7 to 10 mm slice thickness, 1.15 to 1.51 ms echo time, 2.70 to 3.43 ms repetition time, 8 to 15 segments.

2.2.3 DENSE Strain Analysis

Cardiac strains were derived from the DENSE images as previously described using DENSEanalysis, an open-source application [28] written in MATLAB (The Mathworks Inc, Natick, MA). The post-processing steps for each cine DENSE slice included manual segmentation of the left ventricular myocardium and semi-automated

phase unwrapping to obtain the 2D displacements within each cardiac frame.[29] Following the unwrapping, spatial smoothing and temporal fitting of displacements (10th order polynomial) were performed to obtain smooth trajectories for all tissue points beginning at end-diastole and continuing through systole into mid-diastole.[29] Circumferential and longitudinal strains were calculated from short-axis and four-chamber images, respectively, using the Lagrangian Green finite strain tensor. Both circumferential and longitudinal strain were defined as negative for tissue shortening. For participants that had all three short-axis images (basal, mid-ventricular, and apical), cardiac torsion was calculated as the gradient of twist down the long axis of the left ventricle by finding the slope of the linear regression line between twist and longitudinal position. Twist was defined as positive for counter-clockwise rotation relative to the centroid of the left ventricle when viewing a short-axis image from the apex towards the base. Torsion was positive when the apex was twisting more positively than the base.

2.2.4 Feature Tracking Strain Analysis

Strain and twist were derived from SSFP imaging with Diogenes feature tracking software (TomTec Imaging Systems, Munich, Germany). For short-axis images, both endocardial and epicardial contours were manually drawn at end-diastole and the software automatically propagated the contours through the remaining frames. For the four-chamber image, only an endocardial contour was drawn before propagation. In the case of poor tracking, end-diastolic contours were redrawn and the propagation repeated until the tracking was visually acceptable. Circumferential strain, longitudinal strain, and twist were derived from raw output files generated by the software. In short-axis slices and for appropriate comparisons to DENSE, which measures strain and twist throughout the myocardial wall, the endocardial and epicardial strains and twist from feature tracking were segmentally averaged together to approximate a single transmural value. Torsion was computed from the

twist results using the same calculation as above for DENSE imaging. Studies using feature tracking have stated that strains were derived using the 1D Lagrangian calculation [14, 26, 27],[20, 30, 31] and this was reaffirmed through email correspondence with the vendor.

To assess circumferential and longitudinal strains via the change in length of entire contours, the contour position data reported in the output files from feature tracking were used. By using these contours, rather than having an observer draw them separately, any intra- and inter-observer variability was removed for the comparison between contour-based strains and feature tracking. Contour-based strains were derived from the 1D Lagrangian strain calculation.

2.2.5 Relationship between 1D Lagrangian and 2D Lagrangian Green Strain Calculations

The 1D Lagrangian strain calculation (ϵ_L) has been well-described as the change in the length (ΔL) of a segment of tissue divided by its initial length (L_0):

$$\epsilon_L = \frac{\Delta L}{L_0} \tag{2.1}$$

The differences between this common calculation and another common 1D calculation, natural strain (S_N), have also been well-documented as natural strain is related to Lagrangian strain through the natural logarithm (ln) [32]:

$$\epsilon_N = \ln(\epsilon_L + 1) \tag{2.2}$$

However, in 2 or more dimensions, it is not common or appropriate to use 1D calculations. Indeed, given the large, finite deformations that occur within the heart, it is common to use the Lagrangian Green finite strain tensor. This tensor, which has been used throughout the DENSE literature and in myocardial tagging literature,[6, 33, 9, 29, 7] relies on spatial derivatives of the displacement field. The relationship

between the 1D and 2D calculations has not previously been well-described. In order to compare the 1D and 2D calculations, it is necessary to consider the 1D Lagrangian strain calculation as a spatial derivative of displacement. As a derivative, the 1D Lagrangian strain is given by:

$$\epsilon_L = \frac{dU_x}{dX} \tag{2.3}$$

Where U_x is the displacement in the x-direction. Then, the 2D calculation can be considered in two steps. First, the deformation gradient tensor (F) is formed from four spatial derivatives of the displacement field and the identity matrix (I):

$$F = \begin{bmatrix} \frac{\partial U_x}{\partial X} & \frac{\partial U_x}{\partial Y} \\ \frac{\partial U_y}{\partial X} & \frac{\partial U_y}{\partial Y} \end{bmatrix} + I \tag{2.4}$$

U_y is the displacement in the y-direction. Second, the Lagrangian Green finite strain tensor (E) is calculated by the following matrix equation where superscript T denotes the transpose operation:

$$E = \left(\frac{1}{2}\right)\left(F^T F - I\right) \tag{2.5}$$

For comparison with the 1D calculation, Lagrangian Green strain (ϵ_G) in the x-direction is given by the first component of E:

$$\epsilon_G = \frac{dU_x}{dX} + \left(\frac{1}{2}\right)\left(\frac{dU_x}{dX}\right)^2 + \left(\frac{1}{2}\right)\left(\frac{dU_y}{dX}\right)^2 \tag{2.6}$$

By inspection of the terms in (ϵ_G), the first term is equal to the 1D Lagrangian strain. The second term is half of the square of the 1D Lagrangian strain, which would be a negligible component only if the strain is infinitesimal. The final term is half of the square of a shear component, which is negligible if the amount of shear is infinitesimal. Ignoring the shear component, the relationship between the

2D calculation (ϵ_G) and 1D calculation (ϵ_L)is:

$$\epsilon_G = \epsilon_L + \left(\frac{1}{2}\right)(\epsilon_L)^2 \tag{2.7}$$

For negative strains, such as circumferential and longitudinal strains, the magnitude of the result from the 2D calculation is lower than that from the 1D calculation. However, for positive strains, such as radial strain, the 2D calculation results in a higher magnitude strain.

In order to properly evaluate the agreement between techniques that report 1D Lagrangian strain (such as feature tracking or contour-based strains) and gold standard techniques that use the 2D Lagrangian Green strain tensor (such as DENSE), we propose that a correction can be applied to the 1D strain results based on the above relationship. Specifically, given a 1D Lagrangian strain ϵ_L, we propose to adjust that value by adding $(1/2)(\epsilon_L)^2$ to partially account for the differences between the strain calculations.

2.2.6 Statistics

The agreement of strains and torsion between feature tracking and DENSE was assessed with Bland-Altman analyses and coefficients of variation. Based on similar analyses in previous studies,[34, 35] coefficients of variation less than 20% were considered acceptable. Paired t-tests were utilized to determine statistical significance using $p < 0.05$. Comparisons between feature tracking and DENSE were made both before and after adjusting the feature tracking results to account for the differences in strain calculations. Bland-Altman analyses and coefficients of variation (CoV) were also used to compare adjusted feature tracking strains to adjusted contour-based strains. Continuous data are presented as mean ± standard deviation.

Table 2.2: Volunteer characteristics

	Base (N = 39)	Mid (N = 69)	Apex/Torsion (N = 38)	Four-Chamber (N = 40)
Age	27 ± 12	26 ± 14	27 ± 12	22 ± 9
Male, n (%)	23 (59)	44 (64)	22 (58)	23 (58)
Diagnosis, n (%)				
Healthy	24 (62)	51 (74)	23 (61)	39 (98)
Tetralogy of Fallot	6 (15)	6 (9)	6 (16)	1 (3)
Duchennes	1 (3)	1 (1)	1 (3)	0 (0)
Hypertrophic	2 (5)	2 (3)	2 (5)	0 (0)
Ischemic	1 (3)	2 (3)	1 (3)	0 (0)
Other	5 (13)	7 (10)	5 (13)	0 (0)

2.3 Results

2.3.1 Study Population

From the review of our database, 89 unique participants were identified that had spiral cine DENSE and SSFP imaging at the same image locations. Of those, 1 participant had poor DENSE image quality due to aberrant prospective ECG triggering and was therefore omitted from analyses. From these 88 participants, we obtained 186 independent image pairs, regionally distributed as follows: 39 basal short-axis, 69 mid-ventricular short-axis, 38 apical short-axis, and 40 four-chamber images. For torsion, 38 participants had all 3 of the necessary short-axis images (*i.e.* all participants that had an apical short-axis image also had the other short-axis images). Characteristics of the participants for each image location are recorded in Table 2.2. Compared to other regions, there was a preponderance of healthy individuals in the four-chamber images due to only acquiring short-axis DENSE images in many patient studies.

2.3.2 Comparison between Feature Tracking and DENSE

Mean circumferential strains from the base, mid-ventricle, and apex were all significantly over-estimated by feature tracking compared to DENSE without 2D

Table 2.3: Summary of strains and torsion from feature tracking and DENSE

	Feature Tracking (Unadjusted)	Feature Tracking (Adjusted)	DENSE	P_1	P_2
Circumferential Strain (%)					
Base	-21.7 ± 4.2	-19.3 ± 3.3	-15.2 ± 3.7	<0.001	<0.001
Mid	-19.5 ± 4.3	-17.5 ± 3.5	-17.2 ± 3.4	<0.001	0.36
Apex	-25.4 ± 7.8	-21.9 ± 5.7	-19.4 ± 3.6	<0.001	0.01
Longitudinal Strain (%)					
Four-Chamber	-15.4 ± 5.1	-14.1 ± 4.3	-13.8 ± 2.9	0.08	0.77
Torsion (°/cm)	2.1 ± 1.2	—	3.5 ± 0.9	<0.001	—

P_1, Feature Tracking (Unadjusted) vs. DENSE
P_2, Feature Tracking (Adjusted) vs. DENSE

Lagrangian adjustment (Table 2.3). Mean longitudinal strain (unadjusted) was similarly over-estimated by feature tracking, although the result was not statistically significant. After making the 2D Lagrangian adjustment to account for differences in the strain calculations, mean feature tracking strains all trended closer to corresponding DENSE values such that the mid-ventricular circumferential strains were no longer different. However, basal and apical circumferential strains remained significantly different even after adjustment. A gradient of increasing circumferential strain from base to mid-ventricle to apex was observed in the DENSE results. This gradient was not present in the feature tracking results before or after adjustment. Torsion was substantially underestimated by feature tracking compared to DENSE (2.1 ± 1.2 vs. 3.5 ± 0.9 °/cm, P < 0.001).

For circumferential and longitudinal strains, the biases, 95% limits of agreement, and CoVs were lower after the feature tracking results were adjusted (Table 2.4, Figure 2.1). Circumferential strain at the mid-ventricular level had the best agreement between adjusted feature tracking and DENSE based on all three measures (bias: -0.4%, 95% limits: 6.3%, coefficient of variation: 10.9%). All other

Table 2.4: Summary of Bland-Altman analyses and coefficients of variation

	Feature Tracking (unadjusted) vs. DENSE			Feature Tracking (Adjusted) vs. DENSE		
		95%			95%	
	Bias	Limits	CoV	Bias	Limits	CoV
Circumferential Strain (%)						
Base	-6.5	±7.7	25.1	-4.0	±6.7	17.8
Mid	-2.3	±7.3	13.7	-0.4	±6.3	10.9
Apex	-6.0	±14.3	22.3	-2.4	±10.8	14.8
Longitudinal Strain (%)						
Four-Chamber	-1.5	±10.7	21.3	-0.2	±9.3	19.3
Torsion (°/cm)	-1.4	±2.4	41.1	—	—	—

strains demonstrated CoVs above 20% before applying the adjustment. Those same CoVs dropped below 20% after the adjustment. The negative biases for basal and apical circumferential strain, even after adjustment, indicated that feature tracking overestimated the strain magnitude relative to DENSE in those regions. Torsion had the worst agreement as assessed by CoV (41.1%) and was underestimated by feature tracking with a bias of -1.4 °/cm.

2.3.3 Comparison between Feature Tracking and Contour-based Strain

Excellent agreement was observed between all circumferential and longitudinal strains from feature tracking and contour-based strains (Table 2.5, Figure 2.2) with CoVs between 3.2 and 7.0%. Bland-Altman 95% limits (between ±2.2 and ±3.8%) were substantially lower than those observed during the comparisons between feature tracking and DENSE.

2.4 Discussion

This study evaluated the hypotheses that strains and torsion derived from feature tracking agree well with those derived from DENSE, and that strains from

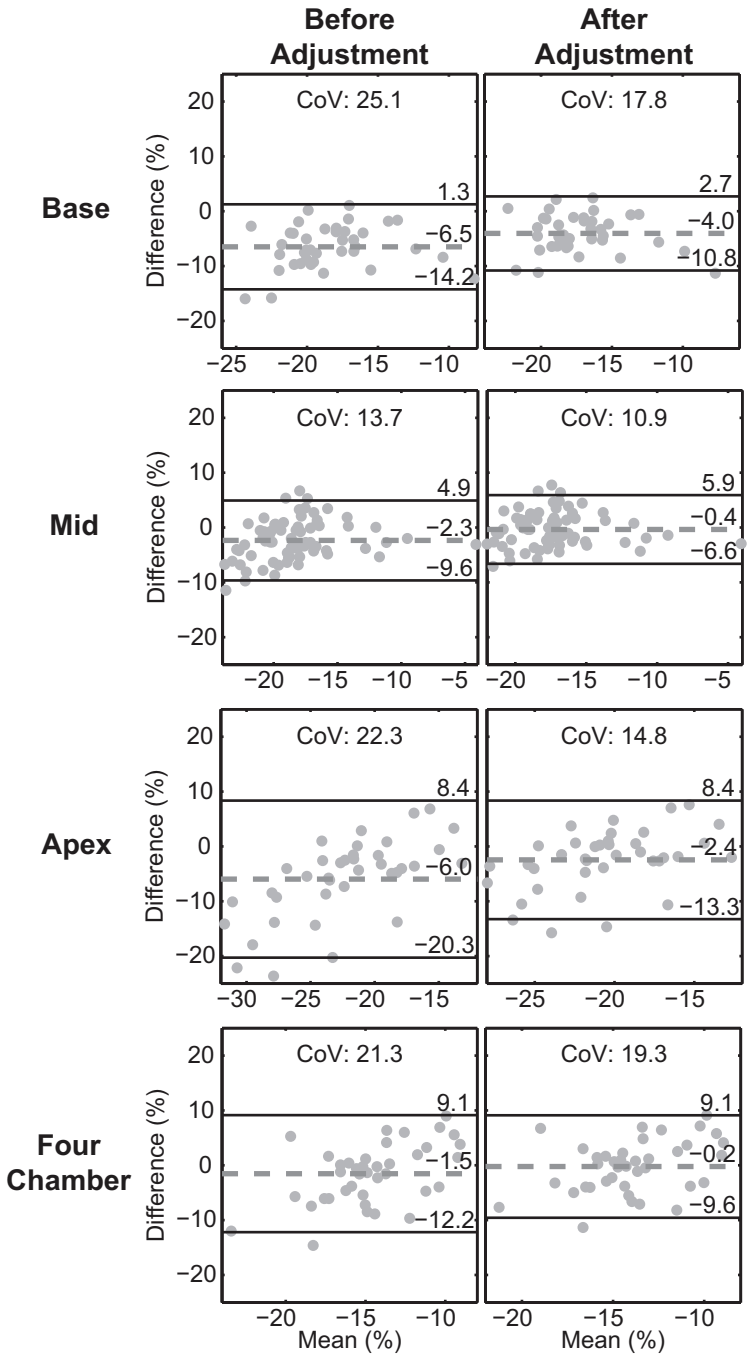

Figure 2.1: Bland-Altman analyses for circumferential and longitudinal strains between feature tracking and DENSE. Analyses were performed both before (left column) and after (right column) adjusting the feature tracking results. All differences were calculated by subtracting the DENSE strain from the feature tracking strain. All biases and 95% limits of agreement improved after adjusting the feature tracking strains. The best agreement was observed in mid-ventricular circumferential strain.

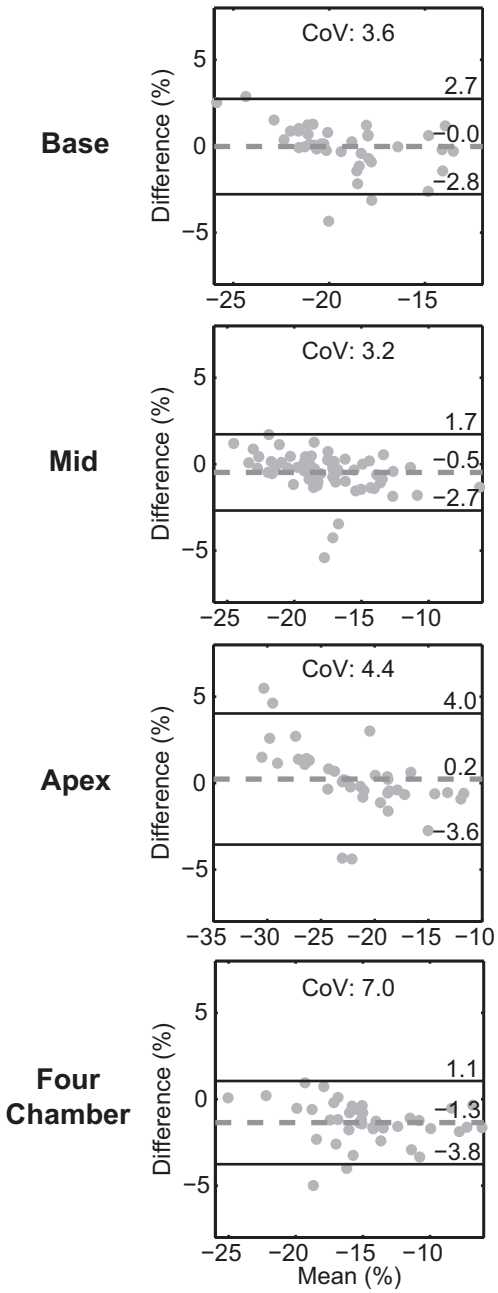

Figure 2.2: Bland-Altman analyses for circumferential and longitudinal strains between feature tracking and contour-based strains. All differences were calculated by subtracting the feature tracking strain from the contour-based strain. Excellent agreement (small biases and tight 95% limits) was observed for all circumferential and longitudinal strains.

Table 2.5: Bland-Altman analyses and coefficients of variation for feature tracking and contour-based strains

	Feature Tracking vs. Contour Strain		
	Bias	95% Limits	CoV
Circumferential Strain (%)			
Base	-0.0	±2.8	3.6
Mid	-0.5	±2.2	3.2
Apex	0.2	±3.8	4.4
Longitudinal Strain (%)			
Four-Chamber	-1.3	±2.4	7.0

feature tracking agree well with strains derived from the change in length of entire contours. Our primary findings included: 1) the best agreement between feature tracking and DENSE was observed in mid-ventricular circumferential strain, 2) even after adjustment, feature tracking significantly overestimated the magnitude of circumferential strain in basal and apical images, 3) longitudinal strain had borderline acceptable agreement between feature tracking and DENSE, 4) feature tracking significantly underestimated torsion with an unacceptable coefficient of variation, and 5) slice-wise strains from the change in length of entire contours had excellent agreement with slice-wise strains reported by feature tracking.

2.4.1 Circumferential Strain from Feature Tracking and DENSE

Mid-ventricular circumferential strain had the best agreement between feature tracking and DENSE with 95% limits of 6.3% and a coefficient of variation of 10.9%. Previous studies that assessed this agreement between feature tracking and myocardial tagging have shown 95% limits between 3.3% [16] and 9.1% [22], with several other studies in between.[19, 20, 31] The level of agreement observed in the current study with DENSE is similar to those levels of agreement observed with myocardial tagging. For circumferential strain in basal and apical images, however,

significant biases and larger coefficients of variation existed, which indicates that feature tracking and DENSE do not agree as well in those regions. In particular, apical circumferential strain had the largest 95% limits (±10.8%), which is consistent with a previous study that also observed that the apical region had the largest 95% limits (±12.8% at 1.5 T and ±9.2% at 3.0 T).[22] The largest bias (-4.0%) was observed in basal circumferential strain. This bias was large enough to disrupt the natural increasing gradient in circumferential strain from base to apex that was observed in the DENSE results and has been documented extensively.[33, 8, 36, 37] These inconsistencies between feature tracking and DENSE at the basal and apical levels are likely due to through-plane motion, which invalidates the fundamental assumption that a segment of tissue can be observed and tracked through the entire cardiac cycle in a single 2D image plane. Inter-test variability in both techniques, while larger in feature tracking,[18, 26] likely also contributes to imperfect agreement between them.

2.4.2 Longitudinal Strain from Feature Tracking and DENSE

Among the strains quantified in this study using feature tracking, longitudinal strain had the highest coefficient of variation (19.3%) along with high 95% limits of agreement compared to DENSE (±9.3%). This is consistent with a previous comparison between feature tracking and myocardial tagging which found 95% limits to be ±9.5%.[19] The coefficient of variation was borderline acceptable based on a previously used cutoff of 20%.[34] Large studies may be able to average over this amount of variability while small studies will be hindered. Additionally, while it is common to assess the agreement between feature tracking and gold standard techniques with only healthy participants,[19] we note that there was a preponderance of healthy participants in the assessment of longitudinal strain compared to other strains in this study. The agreement of longitudinal strain between feature tracking and DENSE may be different in patient populations.

2.4.3 Torsion from Feature Tracking and DENSE

Torsion from feature tracking significantly underestimated the DENSE result by 1.4 °/cm on average. This large bias is consistent with the literature as the torsion found by DENSE (3.5 0.9 °/cm) is similar to previous results from DENSE (3.1 to 3.9 °/cm) [8] and myocardial tagging (3.4 to 3.7 °/cm) [38] while the torsion result from feature tracking (2.1 ± 1.2 °/cm) is similar to previous feature tracking studies (2.3 ± 0.8 °/cm).[35] Furthermore, the CoV and 95% limits for comparing DENSE and feature tracking were high (41.1% and ±2.4 °/cm, respectively), indicating that a simple correction for the mean bias would not be sufficient to ensure agreement across methods. A previous study also found poor agreement and correlation between torsion derived from feature tracking and myocardial tagging as well as poor reproducibility from feature tracking.[21] The poor agreement is likely due to the difficulty in tracking myocardial motion in the circumferential direction. While a strong gradient between the blood pool and the myocardium exists for accurately tracking the location of the endocardial contour, the gradients in the orthogonal direction, which are necessary for tracking twist along that contour, are much weaker. These results suggest that further development of feature tracking is needed in order to replicate the gold standard measures of rotational mechanics including twist and torsion.

2.4.4 Slice-wise Strains from Feature Tracking and Contour-based Strains

We found excellent, but imperfect, agreement between contour-based strains and the strains reported by feature tracking. When deriving strains, the feature tracking software may employ curve-fitting techniques after propagating the contours, which could have led to the small differences between feature tracking strain and contour-based strain. A high level of agreement between feature tracking and contour-based strains has been previously reported along with the suggestion that manual border delineation could be a low-cost alternative to purchasing feature tracking software.[24]

Indeed, our results support that slice-wise strains calculated from the change in length of contours between two time points (end-diastole and end-systole) can be used in place of feature tracking slice-wise strains.

2.4.5 Implications

In light of these findings, and the findings of others, it is useful to consider two groups of measures for assessing the utility of feature tracking. First, there are measures that are not obtainable from manually drawing contours at two time points because they require estimates of motion at the segmental level, estimates of rotational motion, or changes in motion across time (e.g. segmental strains, torsion, strain rates, dyssynchrony). Because gold standard techniques are not widely available and manual contours either cannot measure these quantities or would require manual contouring of several time points, feature tracking could have a substantial impact by accurately and reproducibly assessing these metrics. Unfortunately, for torsion, poor agreement with the gold standard (DENSE) was seen in this study and at least one prior study.[21] Additionally, segmental strains and strain rates have shown poor reproducibility with feature tracking.[18, 22] On the other hand, moderate and borderline-acceptable reproducibility has been seen when measuring dyssynchrony,[39] and, despite poor reproducibility, discriminatory and prognostic power is possible for some of these metrics, such as strain rates, provided the sample size is large.[40, 41] Thus, in its current state, the most appropriate application for using feature tracking to assess these measures is for the evaluation of large, retrospective datasets where gold standard techniques were not acquired and the large sample size can account for the poor reproducibility of feature tracking.

Second, there are measures that are assessable from quick, manual contouring at end-diastole and end-systole (e.g. slice-wise strains). For these measures, particularly for circumferential strain at the mid-ventricle, there is acceptable agreement of feature

tracking with gold standard techniques and acceptable reproducibility.[18] Indeed, these strains are the most commonly reported metrics from feature tracking. However, because of the excellent agreement between feature tracking and contour-based strain, regional tracking capabilities and the cost of the feature tracking software are not required in order to assess these metrics. Many of the insights from previous feature tracking studies could have been produced without the software.

2.4.6 Limitations

While this study evaluated the agreement between mechanics derived from feature tracking and those same measures derived from the gold standard DENSE sequence, we could not evaluate the prognostic utility of the measures. While we observed imperfect agreement between the two techniques, it is still possible that feature tracking (or, equivalently, contour-based strains) produces clinically useful results. However, careful consideration is required before generalizing results from gold standard techniques to feature tracking. There may be cases where only a gold standard technique is sufficient (e.g., identifying a gradient in circumferential strain from base to apex). In addition, the current study did not evaluate all patient populations. Different populations will likely show different levels of agreement. In particular, populations with poor function and reduced through-plane motion would be expected to have better agreement between feature tracking and gold standard techniques. However, since changes in strains may precede changes in other functional measures, quantification of cardiac strains will likely be important in populations with healthy or nearly healthy function.[42] Finally, this study only assessed TomTec feature tracking software. These results may not generalize to other feature tracking implementations, such as Circle (cvi42, Calgary, Canada).[43]

2.5 Conclusion

Good agreement was observed between DENSE and feature tracking in circumferential strain at the mid-ventricular level. Significant biases and worse agreement were seen in circumferential strains at the basal and apical levels, however the coefficients of variation were within acceptable limits. Longitudinal strain from four-chamber images also demonstrated acceptable agreement between DENSE and feature tracking. However, simple contour-based strain demonstrated excellent agreement with feature tracking, suggesting that feature tracking is not required to assess slice-wise strains. Finally, the agreement of torsion between DENSE and feature tracking was poor. In general, estimated mechanics from feature tracking cannot be used in place of mechanics derived from DENSE.

CHAPTER 3

VALIDATION OF *IN VIVO* 2D DISPLACEMENTS FROM SPIRAL CINE DENSE AT 3.0 T

Adapted from: Wehner GJ, Suever JD, Haggerty CM, Jing L, Powell DK, Hamlet SM, Grabau JD, Mojsejenko WD, Zhong X, Epstein FH, Fornwalt BK. Validation of in vivo 2D displacements from spiral cine DENSE at 3T. J Cardiovasc Magn Reson. 2015;17:5

3.1 Background

In Chapter 2, estimates of mechanics from standard clinical MRI were shown to agree poorly with mechanics derived from spiral cine DENSE, a gold standard technique for measuring left ventricular mechanics. This indicated that standard clinical MRI could not be used in place of DENSE in the left ventricle (LV), and, thus, would likely be inappropriate for the right ventricle (RV) as well. The next step is an investigation of whether spiral cine DENSE is valid at a magnetic field strength of 3.0 T. Previously, spiral cine DENSE has only been validated at 1.5 T. While the higher field strength would provide a higher signal to noise ratio (SNR), phenomena such as field inhomogeneities and off-resonance, which can be more pronounced at higher field strengths, may introduce errors into the displacement measurements. This Chapter will investigate the *in vivo* accuracy of spiral cine DENSE at both 1.5 T and 3.0 T.

Displacement Encoding with Stimulated Echoes (DENSE) is a cardiac magnetic resonance (CMR) technique that encodes tissue displacement into the phase of the magnetic resonance signal.[5] This provides pixel-level resolution of Eulerian displacements throughout the imaged slice (Figure 3.1). Due to the stimulated echo acquisition, cine DENSE has inherently low signal that fades through the cardiac

cycle because of T1 relaxation.[5, 44] To counter these limitations, many studies with DENSE at 1.5 T have employed a spiral acquisition, which efficiently acquires k-space and increases SNR compared to typical Cartesian strategies.[7, 45, 6] This acquisition has not been validated at 3.0 T, where the benefits of further increased SNR and longer T1 relaxation times may be offset by field inhomogeneities and off-resonance artifacts that are likely more pronounced at the higher field strength.

Validation of DENSE has been performed at 1.5 T in several ways: by comparing measured displacements to known displacements in a rigid rotating phantom,[44, 29] by comparing measured radial and shear strains to known strains in a non-physiologic deforming phantom,[7] and by comparing left ventricular (LV) strains in participants quantified from DENSE to those quantified from myocardial tagging.[7, 13, 46] These validations and subsequent applications have led to the acceptance of spiral cine DENSE at 1.5 T. This study extends those validations by using myocardial tagging to validate physiologic LV displacements and strains from spiral cine DENSE in human participants at 3.0 T. By using human participants, rather than cylindrical phantoms, the realistic field inhomogeneities and off-resonance effects that are present at 3.0 T were investigated.

In addition to the accuracy of the DENSE displacements and strains, the SNR throughout the cardiac cycle is of interest. Studies with 2D cine DENSE at 1.5 T have used a constant flip angle strategy of 20 [7, 27, 25] or 15.[47] However, 3D volumetric spiral cine DENSE has been performed at 1.5 T with a ramped flip angle strategy,[6] which tends to equalize the SNR across all cardiac phases by using lower flip angles early in the cardiac cycle.[48] A previous study has compared some flip angle strategies at 3.0 T and 1.5 T for cine DENSE with segmented echo planar imaging (EPI),[49] but a similar study has not been done for spiral cine DENSE.

We therefore aimed to test the following hypotheses: (1) DENSE at 3.0 T has sub-pixel displacement accuracy in measuring physiologic motion and is not significantly

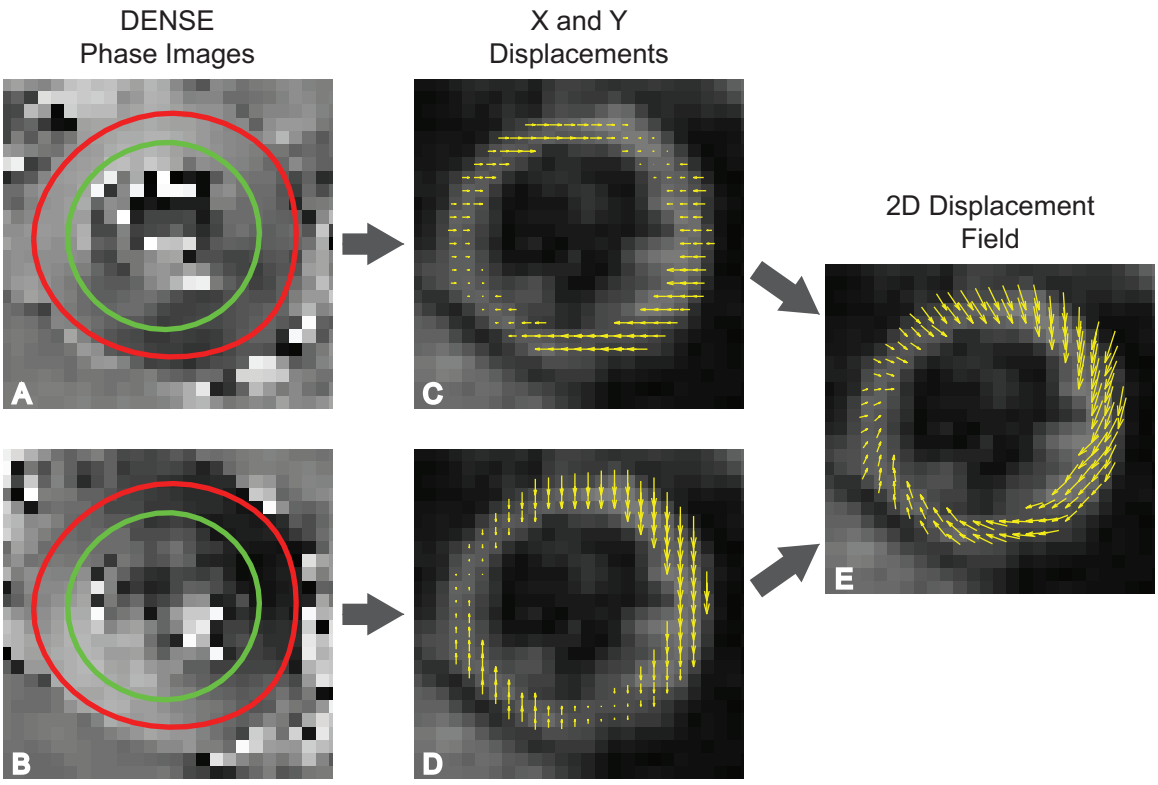

Figure 3.1: Two-dimensional displacements measured by DENSE. The first column (**A, B**) contains X and Y phase images obtained during systole for a healthy participant. The red and green contours define the epicardial and endocardial borders of the left ventricle, respectively. Each pixel within each phase image represents the Eulerian displacement in a single direction (**C, D**). The displacements are overlaid on the magnitude image from DENSE. The third column (**E**) contains the 2D Eulerian displacement field that results from vector addition.

different from the error at 1.5 T, (2) the inter-observer variability of strains derived from DENSE at 3.0 T is similar to that of DENSE at 1.5 T, (3) the cardiac strains and torsion from DENSE at 3.0 T agree with results from analyzing tagged images from the same locations using harmonic phase (HARP), and (4) the SNR of DENSE at 3.0 T is higher than that at 1.5 T and may be best leveraged with different flip angle strategies from those commonly used at 1.5 T.

3.2 Methods

3.2.1 3.0 T Imaging

This protocol was approved by the Institutional Review Board. Ten participants (40% female, age 29 ± 4) without history of cardiovascular disease were consented. Acquisitions at 3.0 T were performed on a Siemens Tim Trio with 6-element chest and 24-element spine coils. After the standard localizers, a cardiac-gated field map was acquired during a breath-hold for second order shimming. Three short-axis (base, mid, apex) and one long-axis (four-chamber) 2D spiral cine DENSE slices were acquired with the following parameters: 6 spiral interleaves (2 interleaves acquired per temporal frame), 360x360 mm^2 field of view, 128x128 image matrix (2.8x2.8 mm^2 pixel size), 8 mm slice thickness, 1.08 ms echo time, 17 ms repetition time (34 ms temporal resolution), 20° constant flip angle, 0.10 cycles/mm encoding frequency, simple encoding,[25] 0.08 cycles/mm through-plane de-phasing frequency,[27] and CSPAMM echo suppression.[13] The spiral acquisition yielded k-space data with a matrix size of 102, which was then zero-padded to 128. The two encoded dimensions were in-plane. The through-plane component was not acquired. Using the R-R interval from the real-time electrocardiogram (ECG), the number of cardiac phases was adjusted to have 100 to 150 ms of dead time, which refers to the period between the last acquired cardiac phase and the next QRS complex on ECG. Reconstruction was performed online with gridding and linear inhomogeneity compensation.[6, 50] No additional off-resonance corrections were performed in the reconstruction. To remove the possible effects of variable breath-hold position, all DENSE scans were performed with a respiratory navigator (acceptance window ± 3 mm). In an effort to improve navigator efficiency, a real-time video of the navigator was projected to the participants, which allowed them to adjust their diaphragm position and to maximize the time spent acquiring data when the diaphragm was

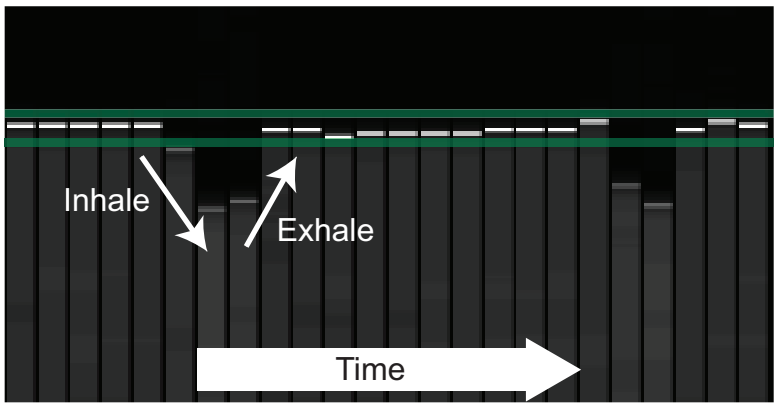

Figure 3.2: Respiratory navigator feedback. The image of the respiratory navigator that was projected to the participants in real-time during the DENSE scans. The horizontal green lines define the ±3 mm acceptance window while the bold white and gray tick marks define the diaphragm location. A breath (inhale and exhale) is labeled.

located within the acceptance window (Figure 3.2).

During the same imaging session, tagged images were acquired at the same slice locations as DENSE with the following parameters: grid tagging 45° to readout direction, 8 mm tag spacing, 340x340 mm^2 field of view, 256x256 acquisition and image matrices (1.3x1.3 mm^2 pixel size), 8 mm slice thickness, 2.72 ms echo time, 5.72 ms repetition time, 15 segments, 10° constant flip angle, and 20 cardiac phases. The tagged images were acquired with pre-navigated breath-holds. The participants used the same navigator as above (Figure 3.2) to place their diaphragm within the acceptance window. The operator watched the diaphragm position in real-time along with the participant and triggered the tagged acquisition once it was inside the acceptance window. The participants then held their breath for the duration of the tagged acquisition.

3.2.2 1.5 T Imaging

Six of the ten participants returned after 185 ± 76 days to perform similar scans at 1.5 T on a Siemens Aera with 18-element chest and 12-element spine coils. The DENSE acquisition parameters were the same as for the 3.0 T case. As before, a

respiratory navigator with a ±3 mm acceptance window was used. However, no visual feedback was available to be projected to the participants. Myocardial tagging acquisition parameters were the same as for the 3.0 T case with the following exceptions: 360x293 mm^2 field of view, 256x141 acquisition matrix interpolated to 256x208 image matrix (1.4x1.4 mm^2 pixel size), 3.89 ms echo time, 4.5 ms repetition time, 9 segments, 14° constant flip angle, and 15-21 cardiac phases (dependent on participant's heart rate).

3.2.3 Overview of Displacement Validation Method

The pixels within the phase images of DENSE represent the Eulerian displacements of the underlying tissue.[5] These displacements can be used to project the instantaneous locations of the tissue back to their original position during the encoding step, which is immediately after detection of the QRS complex on ECG. The encoding step of DENSE and the placement of a perfect grid of taglines in tagged imaging occur at the same point in the cardiac cycle. In myocardial tagging, this grid then deforms with the contracting tissue and the tag intersection points no longer form a perfect grid (Figures 3.3A, 3.3B). If a set of DENSE phase images (with in-plane displacements, denoted as X and Y) were acquired in the same spatial and temporal location as the image of the deformed grid, then the Eulerian displacements represented by the DENSE images could be used to project the tag intersection points back into the original, perfect grid. The deviation of these projections from a perfect grid is a measure of the accuracy in the DENSE displacement data. Figure 3.3 presents an example workflow for both short- and long-axis slices.

3.2.4 Displacement Validation

Displacement analysis was performed offline using *DENSEanalysis*,[28] an open-source software written in Matlab (The Mathworks Inc, Natick, MA) and available at

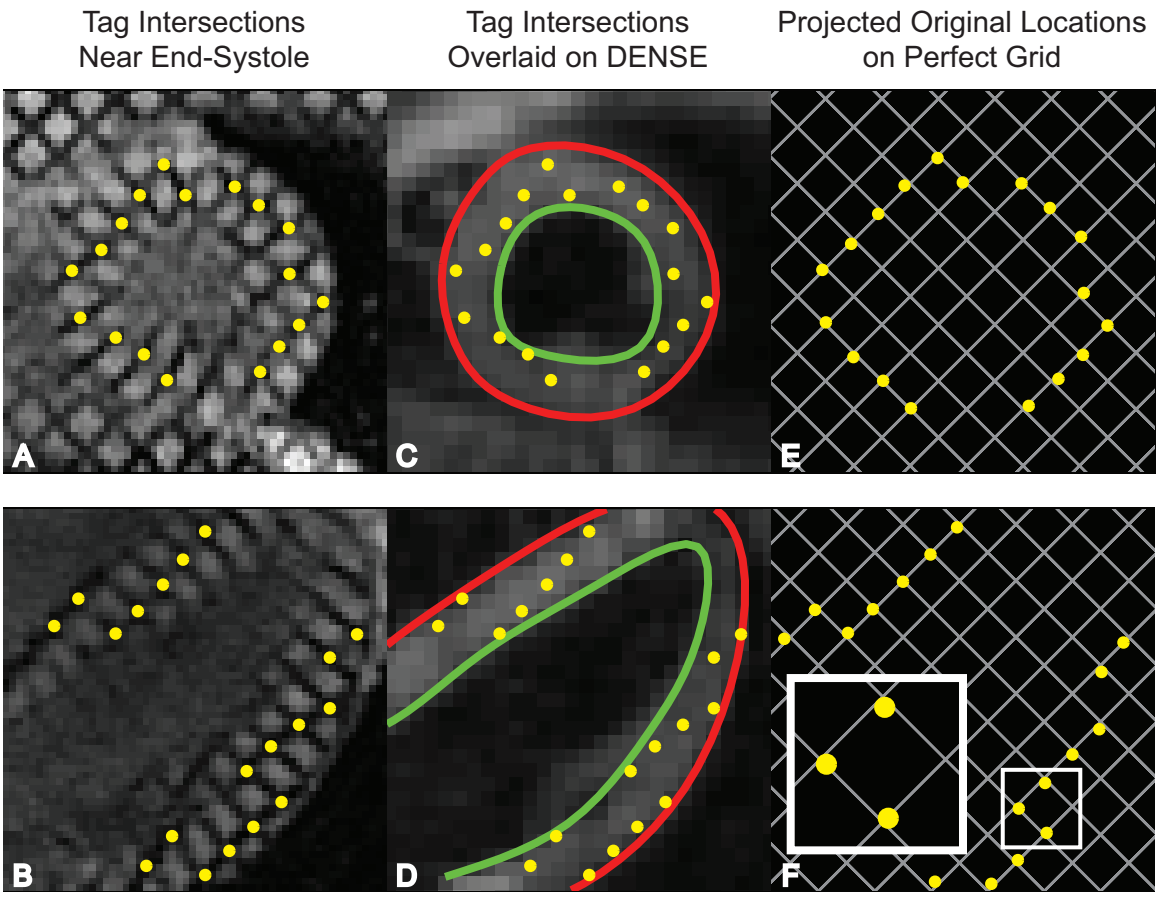

Figure 3.3: DENSE displacements project tag intersection points back into a perfect grid. By end-systole, a perfect grid of tag intersection points has deformed into a warped grid as seen in the first column for both a short-axis and four-chamber slice (**A, B**). The deformed intersection points can be overlaid on DENSE images taken at the same point in the cardiac cycle (**C, D**). The Eulerian displacements from the DENSE images can be used to project the tag intersection points back into a nearly perfect grid (**E, F**). Deviation from a perfect grid of 8x8 mm^2 is a measure of the error in DENSE displacements. The small box in **F** is enlarged to show an example of deviation from the nearest grid intersections.

https://github.com/denseanalysis. Four slices (base, mid, apex, and four-chamber) of myocardial tagging were acquired on each of the ten participants at 3.0 T and each of the six participants at 1.5 T. For each slice, a single observer manually identified the three cardiac phases nearest to end systole and then manually marked tag intersection points in the left ventricle on those cardiac phases. The observer was instructed to only mark definitive intersection points and to ignore intersection points that were unclear. The observer also supplied epicardial contours for each phase to be used for registering the tagged images to the DENSE images to account for any in-plane patient motion. Endocardial contours were not used due to difficulties in discriminating between papillary muscles, trabeculations, and the LV myocardium.

DENSE image processing included manual segmentation of the left ventricular myocardium and semi-automated phase unwrapping.[6, 29, 10] A single observer manually segmented the myocardium by providing endocardial and epicardial contours. Seed points (points that have not experienced phase wrapping) were supplied by the observer at the beginning of the semi-automated phase unwrapping. Using the displacement encoding frequency (0.10 cycles/mm), the unwrapped phase image data were converted to Eulerian displacement maps in millimeters.

Due to the differences in repetition times, DENSE and tagged images were not acquired at the same time points during the cardiac cycle. Therefore, for each slice, the DENSE cardiac phase that was closest in time to one of the marked tagged images was used for further analysis. The tagged image that approximated that DENSE cardiac phase in time was also used for further analysis.

To account for any in-plane patient motion between the tagged and DENSE images, the centroids of the epicardial contours were aligned. The marked tag intersections were then used as points to sample the X and Y Eulerian displacement maps. Linear interpolation was used to determine the X and Y Eulerian displacements for each tag intersection point. Those displacements were then used

to project the intersection points back to their initial, pre-deformed location. Ideally, these projected points would have formed a perfect grid, which is the initial configuration of the tag points when they were applied. Importantly, no other smoothing or processing of the DENSE displacements was performed. Aside from the phase unwrapping and linear interpolation, this method provided a true investigation of the raw displacements from the DENSE imaging.

To measure the deviation from a perfect grid, an 8x8 mm^2 grid at a 45° angle was constructed with reference points located at the grid intersections. These grid parameters are identical to the parameters from the tagged acquisition. An iterative closest point algorithm [51] that did not permit rotation was used to fit this perfect grid to the projected tag intersection points and to calculate the root-mean-squared error (RMSE) between the projected tag intersection points and the nearest perfect grid reference points. The iterative closest point algorithm was used because the exact location of the 45° grid was unknown as no tagged images are acquired at the same instant as the encoding.

For each slice location (four-chamber, base, mid, apex), the distribution of RMSE across the participants at 3.0 T was compared to the distribution at 1.5 T with the Wilcoxon rank sum test.

3.2.5 Strain and Torsion Analyses

Strains from all DENSE slices were calculated by further processing in Matlab of the displacement-encoded phase images. Following automated phase unwrapping, spatial smoothing and temporal fitting of displacements were performed as described previously.[6, 29, 10] This processing provided smooth trajectories for all tissue points beginning at end-diastole (the time of DENSE encoding) and continuing beyond end-systole. The trajectories were not extrapolated into the dead time (the last 100-150 ms of diastole that were not imaged).

Strains were then quantified with the 2D Lagrangian finite strain tensor. For each

short-axis slice, peak radial and circumferential strains were calculated by averaging the strains from all segments within the slice and selecting the peak from the average strain curve. Radial strain was defined as positive for thickening while circumferential strain was negative for shortening. Peak longitudinal strain was calculated in a similar manner from the four-chamber DENSE slice. The most apical segment was excluded from the average before selecting the peak as previously reported.[34] Longitudinal strain was defined as negative for shortening.

In addition to strain, each short-axis DENSE slice also provided a measure of twist. Torsion was then calculated as the gradient of twist down the long axis of the LV by finding the slope of the linear regression line between twist and longitudinal position. The peak torsion was then selected from the torsion curve and reported in units of °/mm. Twist was defined as positive for counterclockwise rotation when viewing a short-axis slice from the apex towards the base. Torsion was positive when the apex was twisting more positively than the base.

Strains and twists from tagged slices were calculated with HARP (Diagnosoft, Durham, NC). For comparison with DENSE, Lagrangian strains were exported from the software for each segment around the myocardium. Twists were exported from HARP for each of the short axis slices and torsion was calculated in the same manner as above. As with DENSE, the most apical segment of the four-chamber slice was excluded from the longitudinal strain average. Other segments were also excluded on a case-by-case basis due to poor tracking. Poor tracking was assessed visually by the observer who was blinded to the results of the DENSE strain analyses.

Two observers independently analyzed each of the DENSE slices in order to compare inter-observer variability in strains and torsions at each field strength with Bland-Altman analysis.[52] A single observer analyzed the tagged slices with HARP for comparison of strains and torsion between DENSE and myocardial tagging at each field strength with Bland-Altman analysis and modified coefficient of variation

(CoV). The equation for CoV for a variable, X, measured on N participants by two observers is below.

$$CoV = \frac{\Sigma_{i=1}^{N}[St.Dev(x_1[i], x_2[i])]/N}{|\Sigma_{i=1}^{N}[(x_1[i] + x_2[i])/2]/N|} \tag{3.1}$$

3.2.6 DENSE Signal to Noise Ratio

To compare the SNR of DENSE between 3.0 T and 1.5 T, the SNR was calculated for each cardiac phase within the mid-ventricular slice of each participant. SNR was calculated from the magnitude images by averaging the signal within the myocardium and finding the standard deviation (noise) of signal within a region outside the body (air) with the care to avoid image artifacts. Corrections were applied for the Rician distribution of the magnetic resonance signal.[53] The true standard deviation of the signal, σ, was calculated from the measured standard deviation, σ_M, by

$$\sigma = \sqrt{\frac{2}{4-\pi}} * \sigma_M \approx 1.526 * \sigma_M \tag{3.2}$$

The true myocardial signal, S, was calculated from the measured myocardial signal, M, by

$$S = \sqrt{M^2 - \sigma^2} \tag{3.3}$$

The DENSE sequences at 3.0 T and 1.5 T varied slightly in the way the magnitude images were reconstructed, likely due to the different versions of DENSE required for the different software installed on the 3.0 T Tim Trio and the 1.5 T Aera (Syngo MR B17 and Syngo MR D13, respectively). At 3.0 T, the magnitude images within a cine series were not normalized independently. Thus, the noise from each cardiac phase was averaged together to get a single noise value for the entire series. The myocardial signal from each cardiac phase was then divided by this noise value to

obtain SNR through the cine series. At 1.5 T, the reconstruction normalized each image independently from others in the cine series, presumably to aid readers in viewing image contrast. Due to this independent scaling, the noise could not be considered constant across all cardiac phases. The SNR of each cardiac phase was calculated from its own noise level without averaging the noise of all phases together. The SNR at each cardiac phase was compared between 3.0 T and 1.5 T with the Wilcoxon rank sum test.

3.2.7 DENSE Flip Angle Analysis

Two of the participants underwent further DENSE imaging at 3.0 T to assess the SNR of different flip angle strategies. Both constant and ramped flip angle strategies of 5, 10, 15, 20, and 25° were investigated (Figure 3.4).[48] The ramped flip angle strategies were designed to maintain equal SNR throughout the cardiac cycle.[48] For a given last flip angle, N, the preceding flip angles can be calculated iteratively as below:

$$\alpha_{n-1} = \arctan\left(\exp\left(\frac{-TR}{T1}\right) * \sin\left(\alpha_n\right)\right) \tag{3.4}$$

TR is the repetition time while T1 is the relaxation constant. A single mid-ventricular short-axis slice was imaged in each case. All other DENSE acquisition parameters remained the same. The SNR of each strategy was calculated in the same manner as above for the 3.0 T case. For each participant, the SNRs were qualitatively compared to investigate whether a strategy other than a constant 20° flip angle would be preferable at 3.0 T.

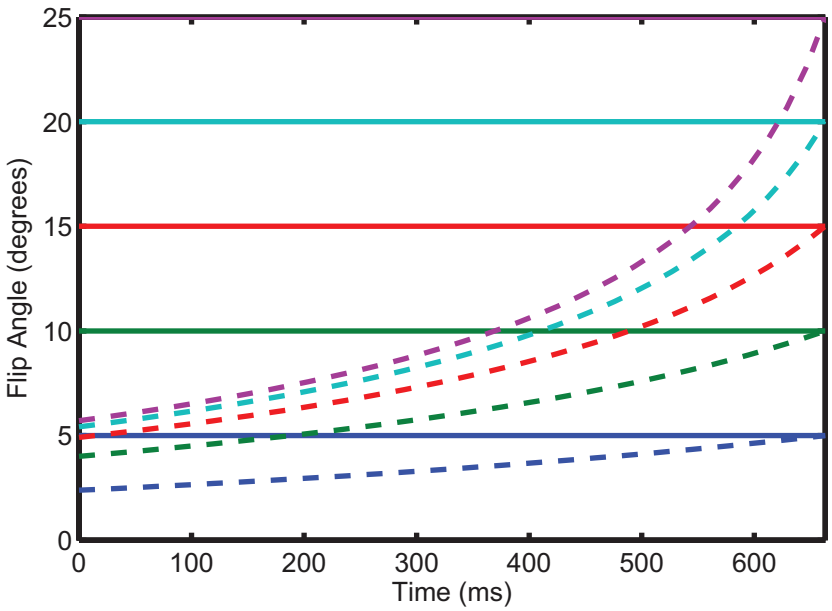

Figure 3.4: Illustration of flip angle strategies throughout the cardiac cycle. The bold, horizontal lines indicate the constant flip angle strategies where the same flip angle is applied throughout the cardiac cycle. The ramped flip angle strategies are indicated by the dashed lines and were calculated as described by Stuber et al.[48] Notice that the ramped flip angle strategies start at low values and increase throughout the cardiac cycle. They are defined by their last flip angle (e.g. the red dashed line is the ramped flip angle strategy that ends at 15°). The ramped flip angle strategies in this illustration were calculated by using 17 ms repetition time, 1000 ms T1 relaxation constant, and 20 cardiac phases (40 repetition times). Typical values of myocardial T1 for healthy participants at 3T and 1.5T have been found.[54]

3.3 Results

3.3.1 Displacement Validation

At 3.0 T, the average temporal difference between the DENSE and tagged images was 3.3 (range: 0.1 - 13.0) ms. At 1.5 T, the average difference was 2.8 (range: 0.8 - 7.7) ms. Both times represent good temporal agreement between the analyzed DENSE and tagged images.

The error in the DENSE displacements, as measured by the RMSE between the projected tag intersection points and a perfect grid, are presented in Figure 3.5. For each slice orientation, no significant differences was seen between the RMSE at 3.0 T and the RMSE at 1.5 T. Considering all slices together, the average RMSEs for 3.0 T and 1.5 T were 1.2 $\pm$ 0.3 mm and 1.2 $\pm$ 0.4 mm, respectively. All RMSEs were below the DENSE pixel spacing (2.8 mm) and below or on the order of the tagged pixel spacing (1.3 and 1.4 mm).

3.3.2 Strain and Torsion Analyses

As a second comparison of spiral cine DENSE between 3.0 T and 1.5 T, the inter-observer variability in the peak strains and torsions produced by analyzing the DENSE slices was assessed with Bland-Altman analyses and CoV. Figure 3.6 contains the Bland-Altman figures for circumferential strain from the three short-axis slices. Both field strengths demonstrated good reproducibility between observers.

Table 3.1 contains inter-observer statistics for the remaining strains and torsion. At both field strengths, longitudinal strain and torsion demonstrated low CoVs. Radial strain, however, had higher biases, 95% limits of agreement, and CoVs compared to the other measures.

Figure 3.7 contains the Bland-Altman analyses for circumferential strain between DENSE and tagged analyses with HARP. The 95% limits and CoVs were higher between DENSE and HARP than the same measurements of DENSE inter-observer

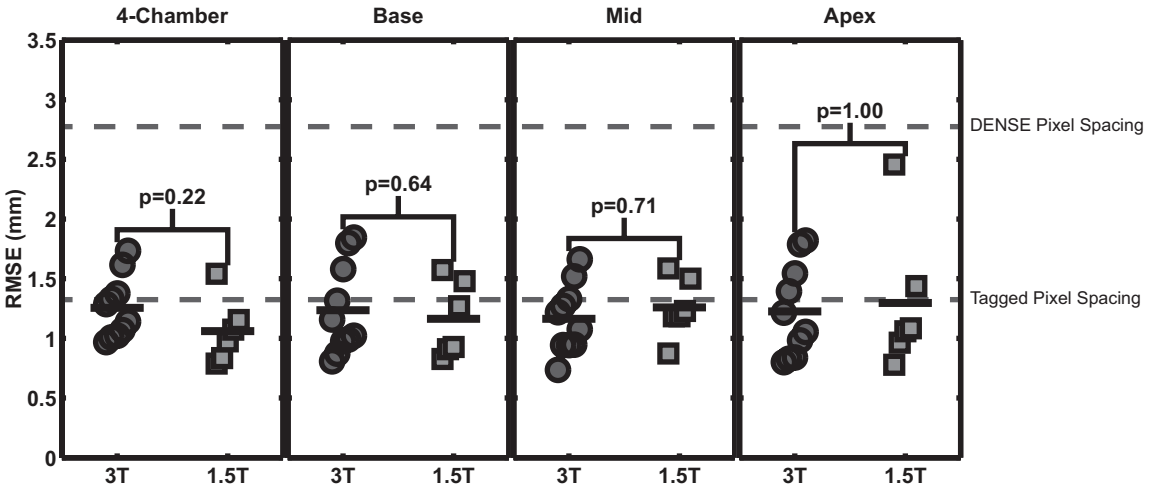

Figure 3.5: RMSE for each slice orientation at 3.0 T and 1.5 T. The error in DENSE displacements as measured by RMSE is shown for each type of slice. The top gray line indicates the DENSE pixel spacing of 2.8 mm. The bottom gray line was placed at 1.35 mm, which is the average of the tag pixel spacing at 3T and 1.5T (1.3 mm and 1.4 mm, respectively). The mean RMSEs were below the DENSE pixel spacing and were below or on the order of the tagged pixel spacing. No significant difference in RMSE were seen between 3T and 1.5T by the Wilcoxon rank sum test for any slice orientation.

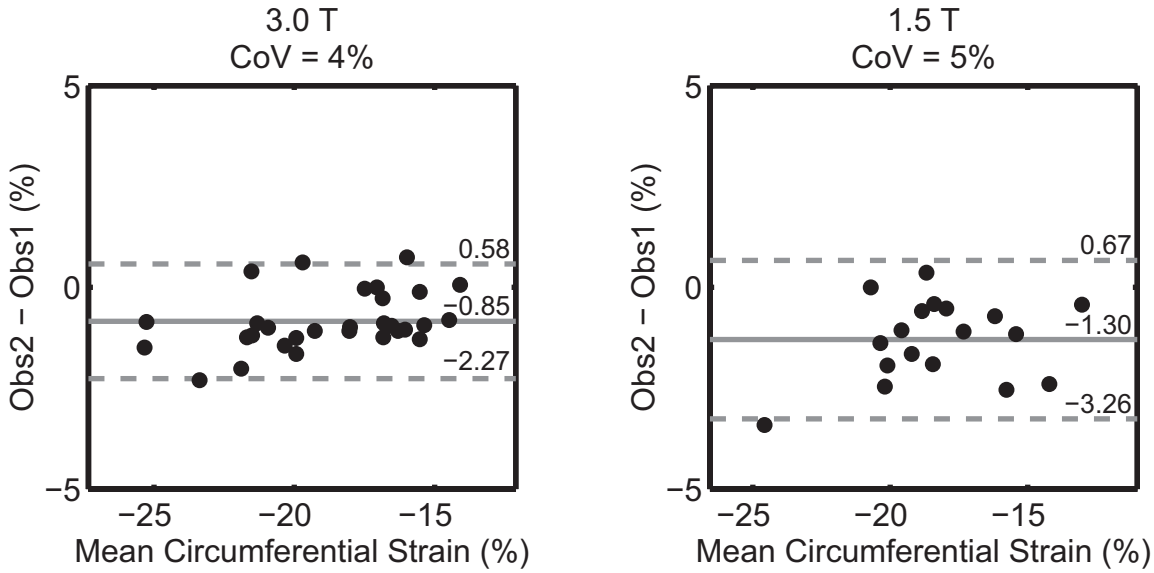

Figure 3.6: Spiral cine DENSE has good inter-observer variability in circumferential strain at both 3.0 T and 1.5 T. The Bland-Altman plots contain the inter-observer peak circumferential strain from the base, mid, and apex slices of DENSE for each field strength. The solid lines indicate the biases while the dashed lines are the 95% limits of agreement.

Table 3.1: Inter-observer variability in strains and torsion quantified with spiral cine DENSE were similar at 3.0 T and 1.5 T.

	3.0 T			1.5 T		
	Bias	95% Limits	CoV (%)	Bias	95% Limits	CoV (%)
Circumferential Strain (%)	-0.8	±1.4	3.6	-1.3	±2.0	5.2
Radial Strain (%)	4.1	±14.7	10.5	-4.5	±13.3	10.4
Longitudinal Strain (%)	0.4	±1.9	3.9	-0.8	±1.5	5.3
Torsion (°/mm)	0.01	±0.02	2.9	0.02	±0.02	3.5

Table 3.2: Variability in strains and torsion between DENSE and HARP at 3T and 1.5T (Bias: DENSE - HARP).

	3.0 T			1.5 T		
	Bias	95% Limits	CoV (%)	Bias	95% Limits	CoV (%)
Circumferential Strain (%)	-0.8	±4.8	7.5	1.2	±4.2	7.6
Radial Strain (%)	-5.3	±40.0	28.5	3.4	±52.2	36.0
Longitudinal Strain (%)	-1.8	±3.2	9.8	2.0	±5.6	13.0
Torsion (°/mm)	0.13	±0.09	30.4	0.11	±0.12	31.6

variability.

Table 3.2 contains the Bland-Altman analyses comparing DENSE to HARP for the remaining strains and torsion. The two field strengths demonstrated comparable agreement between DENSE and HARP. For radial strain and torsion, the 95% limits of agreement and CoVs were high at both field strengths. Circumferential and longitudinal strains showed better agreement.

3.3.3 DENSE Signal to Noise Ratio and Flip Angle Analyses

The SNR at 3.0 T remained higher than the SNR at 1. 5T for 750 ms (Figure 3.8). This difference was significant for periods up to 476 ms by the Wilcoxon rank sum test ($p<0.05$). Using all of the cardiac phases, the SNR at 3.0 T was greater than the SNR at 1.5 T by a factor of 1.4 ± 0.3.

Rather than using a constant 20° flip angle, the SNR gain at 3.0 T may be

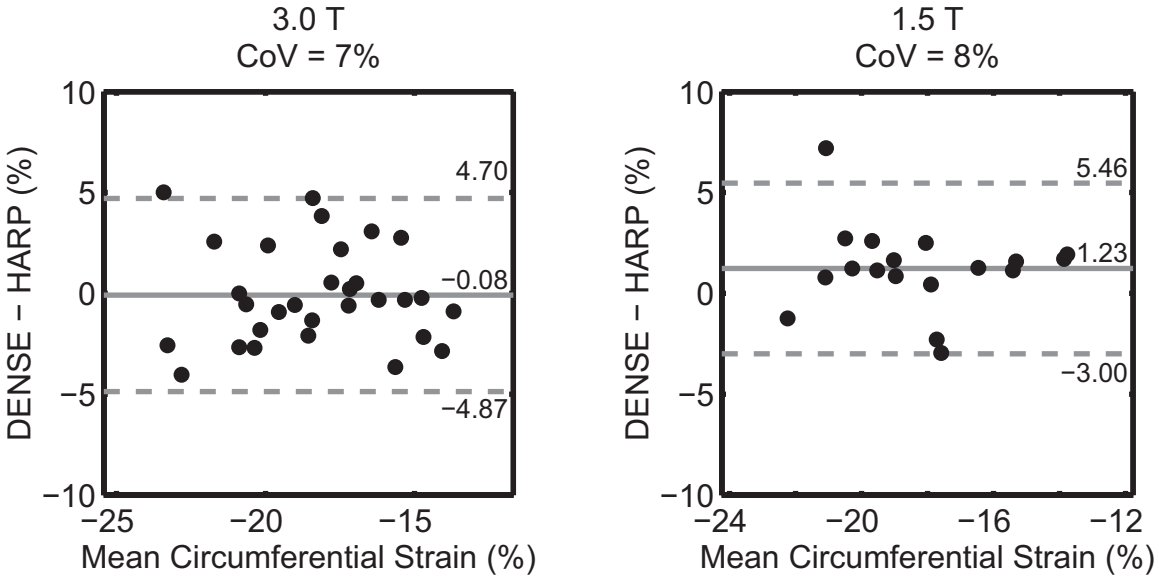

Figure 3.7: Bland-Altman plots for circumferential strain between DENSE and HARP. The solid lines indicate the biases while the dashed lines are the 95% limits of agreement. The 95% limits and CoVs between DENSE and HARP were larger than DENSE inter-observer variability.

better leveraged with a ramped flip angle strategy. To investigate this, SNR was measured in two participants for a range of constant and ramped flip angles at 3.0 T. In Figure 3.9, the solid lines represent the SNR curves of constant flip angle strategies while the dashed lines represent the SNR for the ramped flip angle strategies. In both participants, the constant flip angle strategies provided higher SNR (except for the 5° case) in early systole. However, they had the lowest SNRs in diastole. The ramped flip angle strategies, particularly the 15°, 20°, and 25° cases, provided SNRs above 20 for most cardiac phases in both participants.

3.4 Discussion

Spiral cine DENSE has been validated and utilized at 1.5 T for measuring cardiac displacements and deformation.[7, 45, 6] In the present study, we investigated the hypothesis that the same spiral acquisition could be used at 3.0 T to gain SNR without compromising displacement accuracy due to increased field inhomogeneities or off resonance effects that are likely present at the higher field strength. We developed a

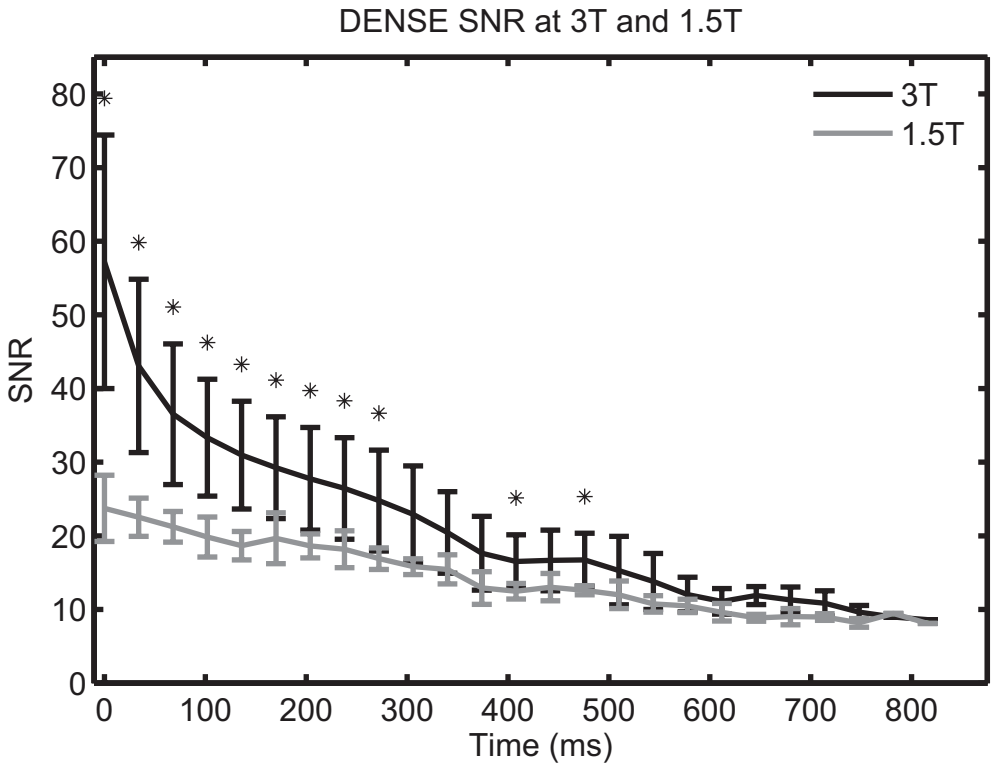

Figure 3.8: Spiral cine DENSE SNR at 3.0 T and 1.5 T. Average SNR curves from all participants were calculated at 3T and 1.5T. Spiral cine DENSE imaging was performed with a constant 20 flip angle. The SNR at 3T was higher than at 1.5T through 750 ms. Statistical significance (p¡0.05) is indicated by asterisks. The last significant difference occurred at 476 ms.

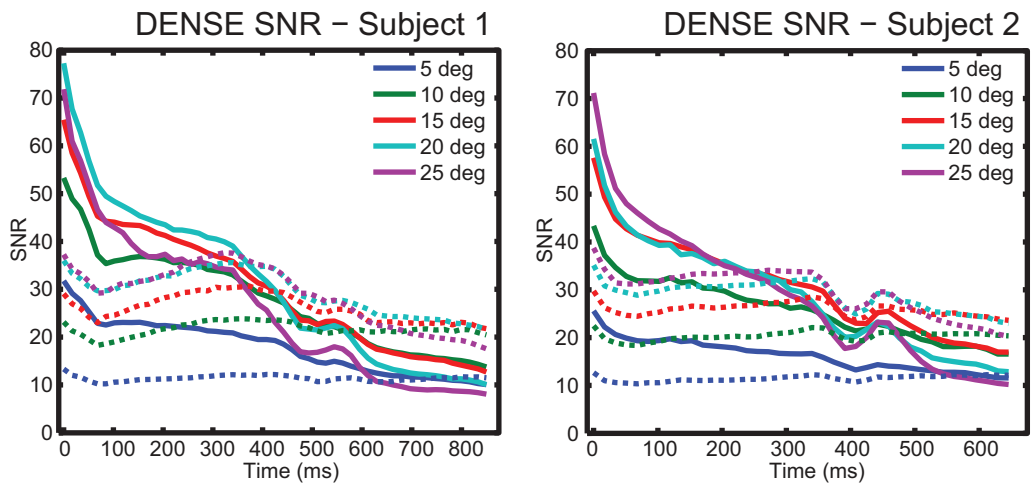

Figure 3.9: DENSE SNR of different flip angle strategies in two participants at 3.0 T. Spiral cine DENSE of a mid-ventricular slice was performed in two participants with different flip angle strategies. The ramped flip angle strategies (dashed lines) ramp up to the indicated degree in the legend. Constant flip angle strategies (solid lines) provided high SNR in early systole at the expense of diastole. Ramped flip angle strategies (particularly 15, 20, and 25) provided SNRs above 20 for most cardiac phases.

displacement validation technique that used DENSE and tagged images to measure the error in physiologic displacements from human participants. Our primary findings included: 1) the displacement error in spiral cine DENSE at 3.0 T was less than the DENSE pixel spacing and not different from the displacement error at 1.5 T; 2) the inter-observer variability of peak strains and torsion from spiral cine DENSE at 3.0 T was acceptable and comparable to the inter-observer variability at 1.5 T; 3) The agreement between spiral cine DENSE at 3.0 T and HARP-based analysis of tagged images was acceptable for circumferential and longitudinal strains and comparable to the agreement at 1.5 T for all strains and torsion; and 4) the SNR of spiral cine DENSE was higher at 3.0 T and may be best leveraged with ramped flip angle strategies that maintain SNR throughout the cardiac cycle.

3.4.1 Displacement Validation

Displacement validation at 3.0 T was performed *in vivo* in order investigate the accuracy of spiral cine DENSE in the setting of physiologic cardiac displacements. Validating the displacements *in vivo* had the added benefit of being affected by the field inhomogeneities caused by the human form, which would not be present when imaging a displacement phantom. Tagged images were acquired to define the ground truth cardiac motion and deformation. Points plotted at the intersection of tag lines near end-systole formed a deformed grid. Eulerian displacements obtained from DENSE phase images ideally contained the exact information needed to project these deformed points back into the initial perfect grid. The deviation from a perfect grid, as measured by RMSE, was a measure of the accuracy in the DENSE displacements. The present method used limited post-processing without smoothing of the displacements. The goal was to investigate the accuracy of raw data from DENSE without introducing confounding post-processing techniques. At 3.0 T, the DENSE errors were less than both the tag spacing of 8 mm and the DENSE pixel spacing of 2.8 mm. Many of the errors were less than the tag pixel spacing of 1.3 mm. In addition, there were no significant differences in displacement error between spiral cine DENSE at 3.0 T and spiral cine DENSE at 1.5 T. Due to the novelty of this validation technique, comparable results for physiologic displacements were not found in the literature. However, the small magnitude of these errors and the similarity between 3.0 T and 1.5 T suggest that any field inhomogeneities or off resonance effects did not substantially affect the measured displacements at the higher field strength.

3.4.2 Strain and Torsion Analyses

The peak strains obtained from spiral cine DENSE at 3.0 T were comparable to the results obtained at 1.5 T and to the results of other studies of cardiac mechanics

in humans.[7, 33] In particular, Young et al. performed spiral cine DENSE at 1.5 T on 19 healthy participants and reported mid-ventricular circumferential strain and radial strain to be -18.3% and 36.6%, respectively.[7] At 3.0 T in the present study, those values were -18.1% and 28.4%.

The inter-observer variability of strains and torsion from spiral cine DENSE at 3.0 T were good for longitudinal strain, circumferential strain, and torsion while acceptable for radial strain. The variability at 3.0 T was comparable to that at 1.5 T and to the variability reported in the literature.[7] Young et al. reported inter-observer 95% limits for circumferential strain and radial strain of 2.3% and 6.9%, respectively.[7] At 3.0 T in the present study, we found those limits to be 1.4% and 14.7%, respectively.

The agreement of strains and torsion between DENSE and HARP was similar between 3.0 T and 1.5 T in the present study. Larger biases and variability were seen for torsion and radial strain compared to longitudinal strain and circumferential strain. Higher variability is expected for radial strain as this parameter is known to be less robust to quantify than the other parameters.[33] The 95% limits of this agreement for all measurements were larger than the inter-observer variability of DENSE but were comparable to previous results.[7] Young et al. compared circumferential and radial strains between DENSE and tags by using a generalized analysis framework rather than HARP. They reported 95% limits for circumferential strain and radial strain of 3.9% and 14%.[7] The present study found similar limits for circumferential strain (4.8%) but higher limits for radial strain (40.0%). The difference in limits between the two studies may be due to differences between HARP and the generalized analysis framework.

The similarities between 3.0 T and 1.5 T in strain values, inter-observer variability, and agreement with HARP suggest that any field inhomogeneities or off resonance effects did not lead to additional errors in quantification of cardiac displacements and

mechanics at 3.0 T.

3.4.3 DENSE Signal to Noise Ratio and Flip Angle Analyses

This study used constant 20° flip angles to compare spiral cine DENSE between 3.0 T and 1.5 T because that flip angle strategy was prevalent in the literature for 1.5 T.[7, 25, 27]] With these constant flip angles, the SNR at 3.0 T was 40% higher than the SNR at 1.5 T. At 3.0 T, the ramped flip angles strategies of 15°, 20°, and 25° provided SNRs above 20 for most cardiac phases. At 1.5 T and with the typical constant 20° flip angle strategy, only the first few cardiac phases had SNRs above 20 while the SNR at end-systole was near 13 and the SNR in diastole was near 9. Future studies with spiral cine DENSE at 3.0 T may use a ramped flip angle strategy to better evaluate cardiac mechanics later in the cardiac cycle with approximately double the diastolic SNR compared to the constant flip angle strategy at 1.5 T.

3.4.4 Limitations

The low number and healthy nature of the participants may limit the applicability of these results to different patient populations. However, the cardiac deformation that is present in healthy participants is likely larger than that found in most patients. The deformations present in this study were therefore a reasonable test of the accuracy of spiral cine DENSE at 3.0 T.

The tagged images were used to define the true motion of the tag intersection points, rather than using a deformable phantom with an externally verified displacement field. There was likely some variability in the manual identification of the tag intersection points. The use of tagged images was necessary because of the difficulty in producing phantoms with known, physiologic deformations. A phantom was also not likely to recreate the field inhomogeneities that are present due to the human form.

A previous study in mice at 7.0 T describes a method for determining the location

of the initial grid of tag intersection points by relying on the tag spacing in stationary tissue.[55] This method was inadequate for our study, particularly at 3.0 T, where much of the stationary tissue was located outside of the adjust volume where proper shimming was not performed and tag lines were significantly warped.

While DENSE has been extended to measure displacements in three dimensions, only 2D (in-plane) displacements were investigated in this study.[6, 9, 10] Many of the applications of DENSE within patient populations have utilized only in-plane displacements.[56, 57] Furthermore, displacement errors due to field inhomogeneities and off resonance effects should be adequately assessed by investigating the in-plane displacements. While cardiac motion does contain a substantial through-plane component, this component was not required for the method of displacement validation. The in-plane displacements were sufficient for projecting deformed tag intersection points into the original 2D grid regardless of the longitudinal motion that occurred.

3.4.5 Future Directions

The primary findings of the present study indicate that the current form of spiral cine DENSE can be implemented at 3.0 T without modifications to compensate for the higher field strength. Future studies can take immediate advantage of the additional SNR at 3.0 T, which may be applied during diastole if a ramped flip angle strategy is used. Alternatively, the additional SNR may be allocated to increased spatial resolution.

3.5 Conclusion

Cine DENSE has inherently low SNR due to the stimulated echo acquisition that has been partially offset with a spiral acquisition. This spiral acquisition has been validated and used extensively at 1.5 T, where field inhomogeneities and off resonance effects are smaller than at 3.0 T. We demonstrated that the same spiral

cine DENSE acquisition can be used at both 1.5 T and 3.0 T with equivalent accuracy. Furthermore, the inter-observer variability and agreement with HARP was comparable at both field strengths. Future studies with spiral cine DENSE may take advantage of the additional SNR at 3.0 T, which will be beneficial for imaging small structures such as the thin right ventricular wall.

CHAPTER 4

SPIRAL CINE DENSE WITH LOW ENCODING FREQUENCIES ACCURATELY QUANTIFIES CARDIAC MECHANICS WITH IMPROVED IMAGE CHARACTERISTICS

Adapted from: Wehner GJ, Grabau JD, Suever JD, Haggerty CM, Jing L, Powell DK, Hamlet SM, Vandsburger MH, Zhong X, Fornwalt BK. 2D cine DENSE with low encoding frequencies accurately quantifies cardiac mechanics with improved image characteristics. J Cardiovasc Magn Reson. 2015;17:93

4.1 Background

In Chapter 3, spiral cine DENSE was found to be similarly accurate at both 3.0 T and 1.5 T. Using spiral cine DENSE at 3.0 T will provide increased SNR, which is valuable for imaging the thin right ventricular wall. The next steps are to optimize the spiral DENSE acquisition for the right ventricle (RV). The RV requires the measurement of 3D displacements due to substantial longitudinal motion and irregular shape. However, measuring 3D displacements requires the use of "balanced" displacement encoding. Such encoding leads to substantial aliasing, or phase wrapping, which can be very difficult for analysis software to handle. This Chapter will investigate the effects of using low displacement encoding frequencies to attenuate the aliasing without compromising resulting measures of cardiac mechanics. Since the RV cannot be analyzed unless the encoding frequency is reduced, this study was performed on the left ventricle (LV) where the typical encoding frequency can be used as a reference.

Displacement Encoding with Stimulated Echoes (DENSE) is a magnetic resonance imaging (MRI) technique that encodes tissue displacement into the phase of the magnetic resonance (MR) signal.[5] The resulting pixel-level resolution of the

displacement field has been used to quantify cardiac mechanics in both healthy and diseased animals and humans.[5, 44, 13, 57, 47, 34] The encoding gradient strength is proportional to the displacement sensitivity of the phase images. It is often referred to as the encoding frequency (k_e) with units of cycles/mm.

In addition to specifying sensitivity, the k_e plays a role in several other processes related to image quality and post-processing. The earliest implementations of DENSE relied on a high k_e to shift the artifact-generating echoes beyond the sampled region of k-space [5] (Figure 4.1, column 1). While this technique removed stripe artifacts, the high encoding gradients caused significant intra-voxel dephasing in deforming tissue, which limited the ability to properly encode displacement during systole.[5] The incorporation of complementary spatial modulation of magnetization (CSPAMM) for echo suppression removed the first artifact-generating echo (the T1 relaxation echo) [13] (Figure 4.1, column 2). This allowed for lower k_e, and thus lower gradients leading to less intra-voxel dephasing, since only the furthest echo (the stimulated anti-echo) had to be shifted out of the k-space field of view. Finally, the addition of a thru-plane dephasing gradient selectively dephased the stimulated anti-echo while preserving the desired stimulated echo [27] (Figure 4.1, column 4). This final addition removed the dependence on high k_e for artifact suppression.

A low k_e is desired to improve the signal to noise ratio (SNR) by reducing the amount of intra-voxel dephasing and to prevent excessive wrapping in the phase images. Recent studies with 2D DENSE have used an in-plane k_e of 0.10 cycles/mm, which creates wrapping in most participants as only 5 mm of displacement is required before wrapping occurs.[47, 7, 45] Unwrapping algorithms have been developed and utilized, but they are not guaranteed to be error-free in all participants or all regions of a given participants heart.[29] Regions with high velocities and noise are the most challenging for automated and semi-automated techniques. Importantly, DENSE

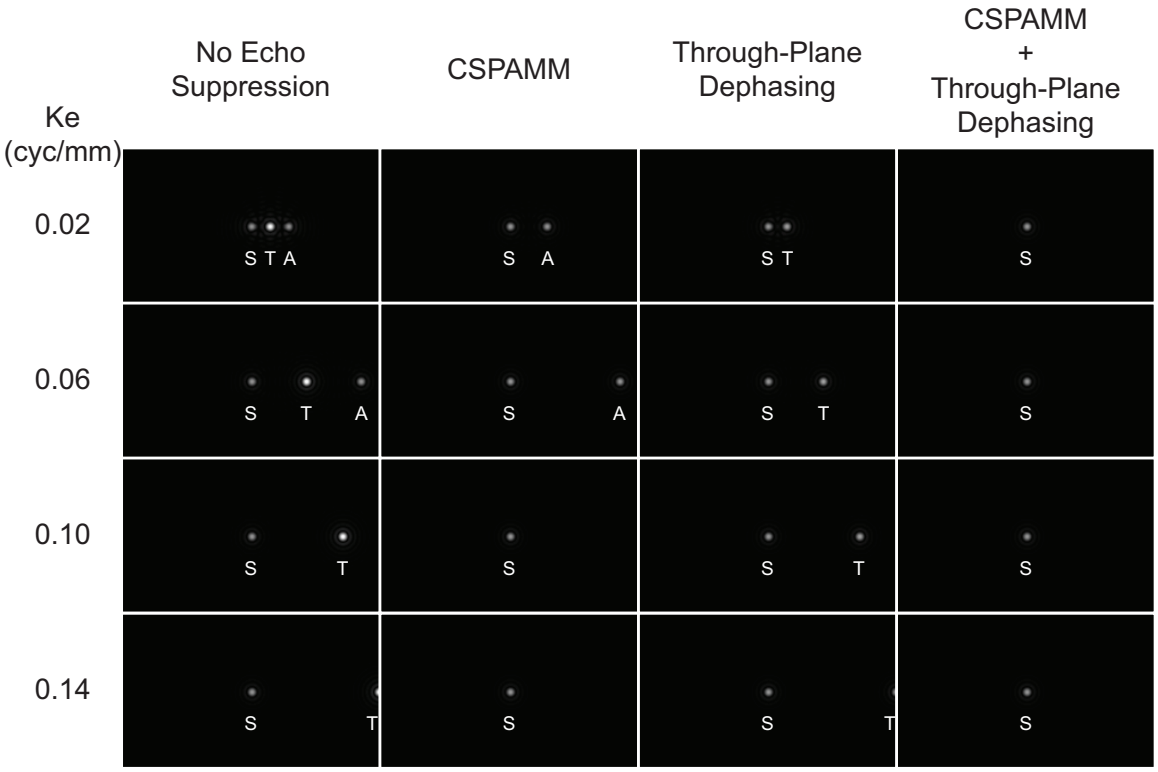

Figure 4.1: The effect of encoding frequency (k_e) and artifact suppression techniques on the DENSE k-space. These simulations of the DENSE k-space illustrate the effect of k_e and artifact suppression techniques. Consider the first k-space in column 1. The echo at the center of k-space is the desired stimulated echo (S). The echo to its right is the T1 relaxation echo (T). The third echo is the stimulated anti-echo (A). Stripe artifacts are generated by the T1 echo and the anti-echo. With no echo suppression technique, a high k_e must be used to shift both artifact-generating echoes beyond the sampled region of k-space (column 1). With CSPAMM echo suppression, the T1 echo is suppressed (column 2). Through-plane dephasing selectively dephases the anti-echo and the T1 echo (column 3). The use of CSPAMM and through-plane dephasing together suppresses both artifact-generating echoes, which removes the dependence on high k_e for artifact suppression (column 4).

studies that use the balanced encoding strategy and online image reconstruction suffer from up to three-fold increased phase wrapping [25] that may not be correctly resolved by the unwrapping algorithm, particularly in the presence of noise. Indeed, lower k_e (0.06 cycles/mm) have been used in these studies to reduce the amount of wrapping and simplify the input to unwrapping algorithms.[25, 6, 9] No direct comparisons with higher k_e have been performed to validate this approach.

Very low k_e may be undesirable due to low sensitivity to displacement.[29, 25] If the sensitivity is too low, there may be errors in the quantifications of cardiac mechanics. While this may be problematic as the k_e approaches zero, a relatively low k_e of 0.04 cycles/mm is still able to resolve displacements of 0.006 mm with typical 12-bit data storage. More importantly, though, the sensitivity of the displacement measurements to phase noise increases with decreasing k_e. No study has investigated a range of k_e to ascertain its effects on quantifications of cardiac mechanics. It has also been suggested that a high k_e is required to dephase the blood pool signal.[29] This may not be the case, however, as long as a through-plane dephasing gradient is in place to accomplish the dephasing.

We hypothesized that 1) quantifications of myocardial circumferential strain, radial strain, and twist will not be different for encoding frequencies between 0.02 and 0.10 cycles/mm, 2) the nulling of the blood signal will be similar for all encoding frequencies, 3) the use of lower encoding frequencies will prevent phase wrapping even in healthy participants with substantial cardiac motion, and 4) lower encoding frequencies will have higher SNR. We tested these hypotheses using a spiral cine DENSE protocol implemented on a 3.0 T Siemens Tim Trio MRI.

4.2 Methods

4.2.1 Image Acquisition

This protocol was approved by the local Institutional Review Board. Ten healthy participants (50% female, age 27 ± 9) without history of cardiovascular disease and ten participants with a history of myocardial infarction or congestive heart failure (40% female, age 57 ± 6) consented for the study. A 3.0 T Siemens (Erlangen, Germany) Tim Trio with a 6-element chest and 24-element spine coil was used to acquire mid-ventricular short-axis 2D cine DENSE images with the following parameters: 6 spiral interleaves, 1 average, 360x360 mm^2 field of view, 128x128 reconstruction matrix, 2.8x2.8 mm^2 pixel size, 8 mm slice thickness, 1.08 ms/17 ms TE/TR, constant 20° flip angle. Two spirals were acquired per heartbeat which yielded a temporal resolution of 34 ms. View sharing was used to achieve 17 ms between reconstructed cardiac frames. Simple encoding was used to measure in-plane displacements while through-plane dephasing of 0.08 cycles/mm and CSPAMM were used for echo suppression.[13, 27, 25] To remove effects due to variable breath-hold position, the acquisitions were performed with respiratory navigator gating and an acceptance window of ±3 mm.

In each participant, the same mid-ventricular short-axis slice was acquired five times with different values of in-plane k_e: 0.02, 0.04, 0.06, 0.08, and 0.10 cycles/mm. The 0.10 cycles/mm acquisition was repeated during the same imaging session to assess inter-test reproducibility.

4.2.2 DENSE Strain and Twist Analyses

Myocardial strain and twist were derived from the DENSE images using *DENSEanalysis*,[28] an open-source application written in MATLAB (The Mathworks Inc, Natick, MA). The post-processing steps for each cine DENSE slice included manual segmentation of the left ventricular myocardium and

semi-automated phase unwrapping to obtain the 2D Eulerian displacements within each cardiac frame.[29] Following the unwrapping, spatial smoothing and temporal fitting of displacements (10th order polynomial) were performed to obtain smooth trajectories for all tissue points beginning at end-diastole and continuing through systole into much of diastole.[29] Radial strain, circumferential strain, and twist were calculated from the resulting displacement fields for each cardiac frame.[10]

Radial and circumferential strains were quantified with the 2D Lagrangian finite strain tensor in six circumferential segments throughout the cardiac cycle. Strain was defined as positive for thickening and negative for shortening. To report peak global strains, the curves from the six segments were averaged into a single global curve from which the peak was selected. Twist was quantified in the same segments and was defined as the angle of rotation about the centroid of the endocardial contour at end-diastole. Twist was positive for counterclockwise rotation when viewing the short-axis slice from the apex towards the base. Peak global twist was quantified in the same manner as the peak global strains.

As many recent studies have used a k_e of 0.10 cycles/mm, the peak strains and twists quantified with the other k_e were compared to the same measures quantified with a k_e of 0.10 cycles/mm. Paired t-tests (with significance defined as $p<0.05$), Bland-Altman analyses,[52] and modified coefficients of variation (CoV) were used for statistical comparison. The equation for CoV is below for a given measurement, X, quantified in N participants with two encoding frequencies (k_{e1} and k_{e2}).[34, 8]

$$CoV = \frac{\Sigma_{i=1}^{N}[St.Dev(x_{ke1}[i], x_{ke2}[i])]/N}{|\Sigma_{i=1}^{N}[(x_{ke1}[i] + x_{ke2}[i])/2]/N|} \tag{4.1}$$

4.2.3 Phase Wrapping

The amount of phase wrapping that occurred for a given participant and k_e was measured by first considering the phase images for the X and Y directions

separately. For each of the two directions, the cardiac frame with the largest percentage of wrapped pixels within the cardiac segmentation was found. The cardiac frame with this largest percentage may have been at slightly different time points for the two directions, though always near end-systole because that is when the most displacement and wrapping occurred. The average of those two percentages was taken as the amount of phase wrapping for that participant and k_e.

4.2.4 Blood Pool Dephasing

Dephasing of the blood signal through the cardiac cycle for each k_e was quantified by calculating the average pixel intensity of the DENSE magnitude images within a set of manually defined contours that denoted the blood pool. Care was taken to ensure that the papillary muscles and trabeculations were not included within the blood pool for this analysis. The magnitude of the blood pool signal was quantified and expressed through the cardiac cycle as a percentage of its signal in the first cardiac phase. To demonstrate the amount of dephasing that occurred by early systole, the blood pool signal remaining at the fifth cardiac frame (85 ms into the cardiac cycle) was compared between the acquisitions with different k_e.

4.2.5 Signal to Noise Ratio

To compare the effects of intra-voxel dephasing between the different k_e, the signal to noise ratio (SNR) was calculated for each cardiac phase. The end-systolic SNR for each lower k_e was compared to the SNR for k_e of 0.10 cycles/mm with a paired t-test. SNR was calculated from the magnitude images by finding the average signal within the myocardium and the standard deviation (noise) of signal within a region of zero signal outside of the body. Care was taken to avoid image artifacts in the region of zero signal. Corrections were applied for the Rician distribution of the MR signal based on Equations 3.2 and 3.3.[53]

4.2.6 Relationship between Phase Noise and SNR

To assess the relationship between phase noise and SNR, the same DENSE acquisitions above were performed on a stationary water phantom. SNR was quantified in the same manner as for the human studies. For each k_e, the phase noise in the X and Y phase images was quantified via the root mean squared error (RMSE) in radians. To compute the RMSE of the 2D displacements, the previous RMSEs were converted from radians to millimeters via the k_e. The X and Y RMSEs in millimeters were then added together via vector addition to yield the 2D RMSE. The phase noise in radians is theoretically inversely proportional to the SNR.[53]

4.3 Results

As quantified by the DENSE acquisition with a k_e of 0.10 cycles/mm, the patients had a mean ($\pm$ standard deviation) global circumferential strain of -12 $\pm$ 6% (range: -3 to -20%). The same measure in the healthy participants was -20 $\pm$ 2% (range: -17 to -23%).

End-systolic images from a representative participant are shown in Figure 4.2 and demonstrate a reduction in phase wrapping at lower k_e. No phase wrapping was present within the segmentation of the myocardium for k_e of 0.04 and 0.02 cycles/mm.

4.3.1 DENSE Strain and Twist Analyses

Negligible differences were seen in strains and twist for all k_e between 0.04 and 0.10 cycles/mm (Figure 4.3, Table 4.1). These differences were of the same magnitude as inter-test differences. The comparison between k_e of 0.02 and 0.10 cycles/mm, however, demonstrated larger biases, larger 95% limits of agreement (LoA), and larger CoVs for both strains and twist. The differences in circumferential strain and twist between k_e of 0.02 and 0.10 cycles/mm were significant ($p < 0.01$ and $p = 0.04$, respectively).

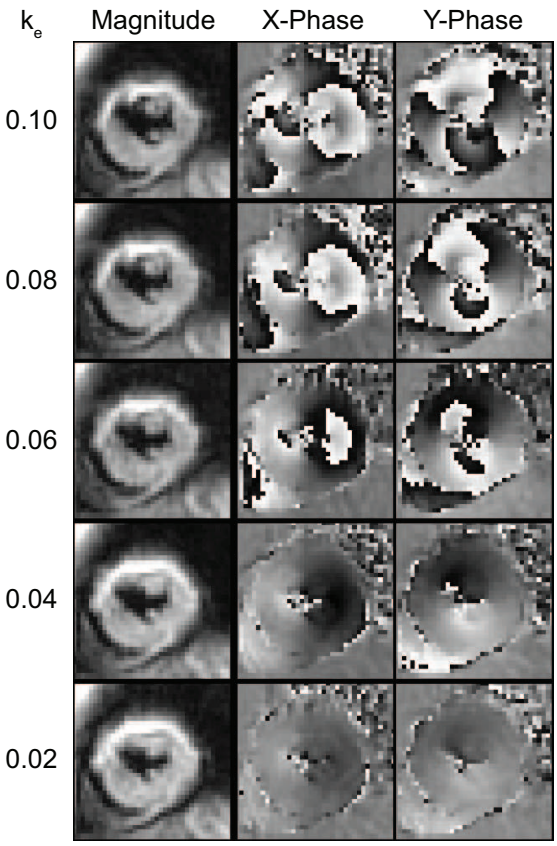

Figure 4.2: End-systolic magnitude and phase images from a participant with previous myocardial infarction. Substantial wrapping was present in the phase images for the higher k_e. As the k_e was decreased, the amount of wrapping in the X and Y phase images decreased. No wrapping was present in the myocardium for 0.02 and 0.04 cycles/mm. Also note that the blood pool dephased similarly for all k_e.

Table 4.1: Summary statistics showed good agreement for all k_e between 0.04 and 0.10 cycles/mm.

	Circumferential Strain (%)				Radial Strain (%)				Twist (°)			
	Bias	95% Limits	CoV	*p*	Bias	95% Limits	CoV	*p*	Bias	95% Limits	CoV	*p*
$E_{0.10}$-$E_{0.02}$	-1.9	±5.0	11%	<0.01	3.9	±20.4	23%	0.11	-0.48	±1.92	14%	0.04
$E_{0.10}$-$E_{0.04}$	-0.6	±3.6	6%	0.15	-0.0	±15.9	14%	1.00	-0.14	±1.22	8%	0.32
$E_{0.10}$-$E_{0.06}$	0.0	±3.2	6%	0.91	0.8	±12.8	13%	0.59	-0.22	±0.93	6%	0.05
$E_{0.10}$-$E_{0.08}$	0.1	±2.6	4%	0.67	-0.5	±10.9	11%	0.67	-0.13	±0.77	5%	0.16
Inter-test	0.1	±2.0	4%	0.53	0.9	±13.0	12%	0.54	-0.05	±0.87	5%	0.59

E_{k_e} represents peak strain or twist using a particular k_e. CoV, *coefficient of variation*

4.3.2 Phase Wrapping

For k_e of 0.02, 0.04, 0.06, 0.08, and 0.10 cycles/mm, the largest percentage of wrapped pixels in the phase images was 0 ± 0, 0 ± 0, 5 ± 6, 17 ± 10, and 32 ± 9%, respectively. Thus, phase images acquired with a k_e of 0.04 cycles/mm had zero wrapped pixels. In contrast, the same phase images acquired with a k_e of 0.10 cycles/mm had about 32% of the pixels wrapped in the cardiac frame with the most displacement.

4.3.3 Blood Pool Dephasing

As k_e increased, the rate of blood pool dephasing increased, however, the standard deviations demonstrated considerable overlap among the different k_e (Figure 4.4). Across the 20 participants and using the fifth cardiac phase as an example, the amount of blood pool signal remaining as a percentage of its initial value was 28 ± 11, 26 ± 10, 24 ± 9, 23 ± 8, and 21 ± 7% for k_e of 0.02, 0.04, 0.06, 0.08, and 0.10 cycles/mm, respectively. Frame 20 was the average end-systolic frame and there was no effective difference in blood pool dephasing by that time.

4.3.4 Signal to Noise Ratio

SNR throughout the cardiac cycle was similar for the different k_e (Figure 4.5), with a trend towards higher SNR at lower k_e. Across the 20 participants, the mean SNR at end-systole, which occurred at different cardiac frames for the different participants, was 23 ± 9, 24 ± 9, 23 ± 9, 23 ± 10, and 22 ± 9 for k_e of 0.02, 0.04, 0.06, 0.08, and 0.10 cycles/mm, respectively. The end-systolic SNR for k_e = 0.02, 0.04, 0.06, and 0.08 were each significantly different than the end-systolic SNR for k_e = 0.10 cycles/mm (p = 0.010, 0.003, 0.005, 0.03, respectively). This represents a 9% increase in SNR for k_e of 0.04 cycles/mm compared to a k_e of 0.10 cycles/mm.

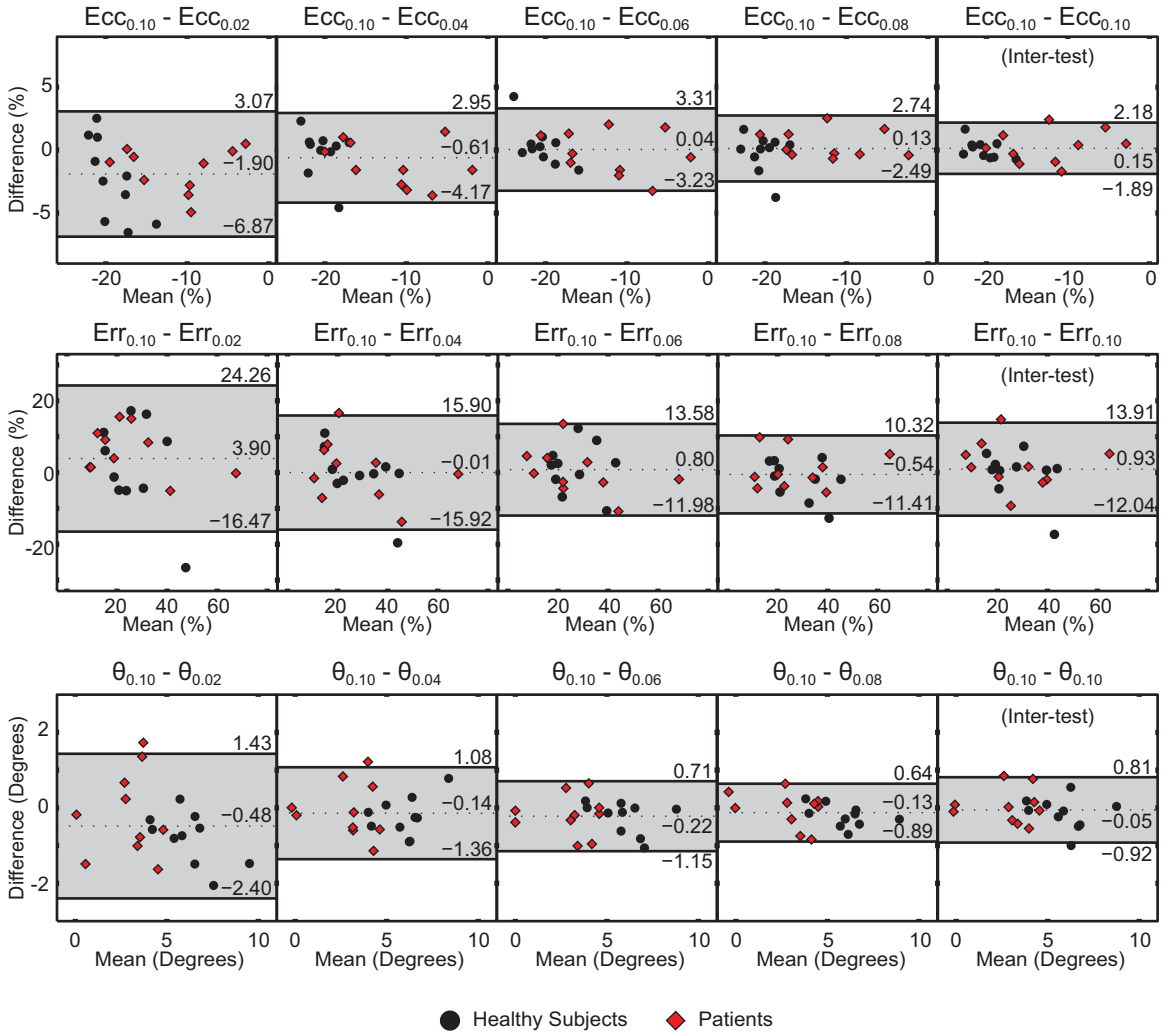

Figure 4.3: Bland-Altman plots demonstrate agreement among k_e of at least 0.04 cycles/mm. The first, second, and third rows contain Bland-Altman plots for circumferential strain (Ecc), radial strain (Err), and twist (), respectively. The subscript values denote the comparisons between acquisitions with the stated k_e. The inter-test comparison was between two acquisitions with k_e of 0.10 cycles/mm. The shaded areas denote the region within the 95% limits of agreement. The worst agreement was seen between 0.02 and 0.10 cycles/mm.

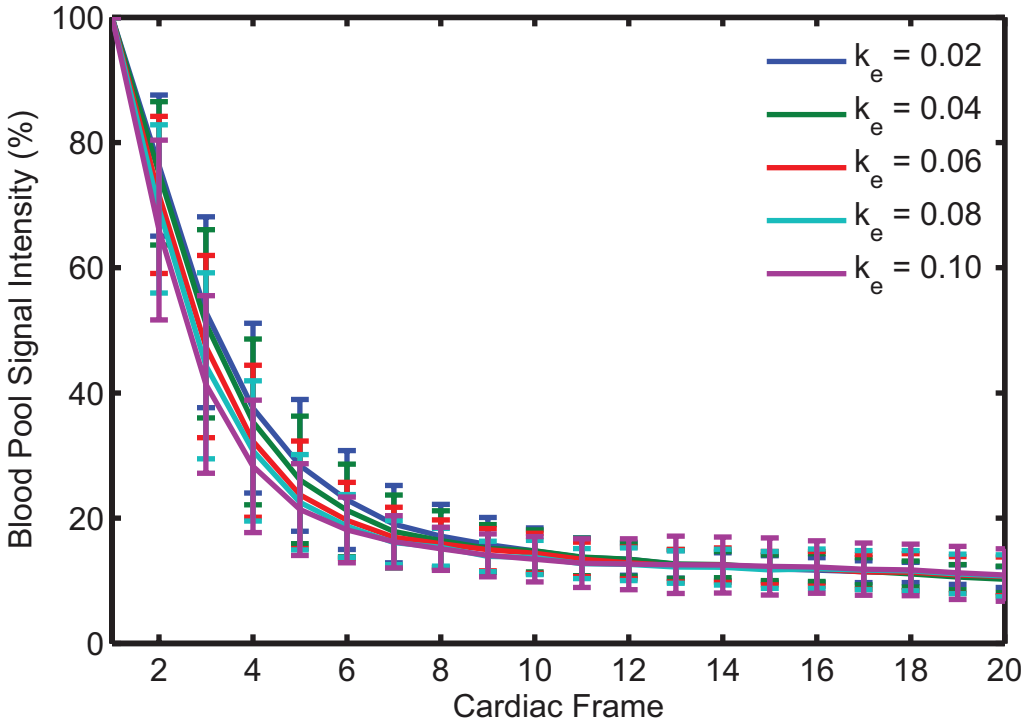

Figure 4.4: Similar rates of blood pool dephasing were observed for the different k_e. Blood pool signal intensity was expressed as a percentage of its value at the first cardiac phase. The first 20 cardiac frames are shown. Each curve represents the average of the 20 participants with standard deviation error bars. As the ke increased, the rate of blood pool dephasing increased, but with considerable overlap between the different ke as seen by the wide standard deviation bars.

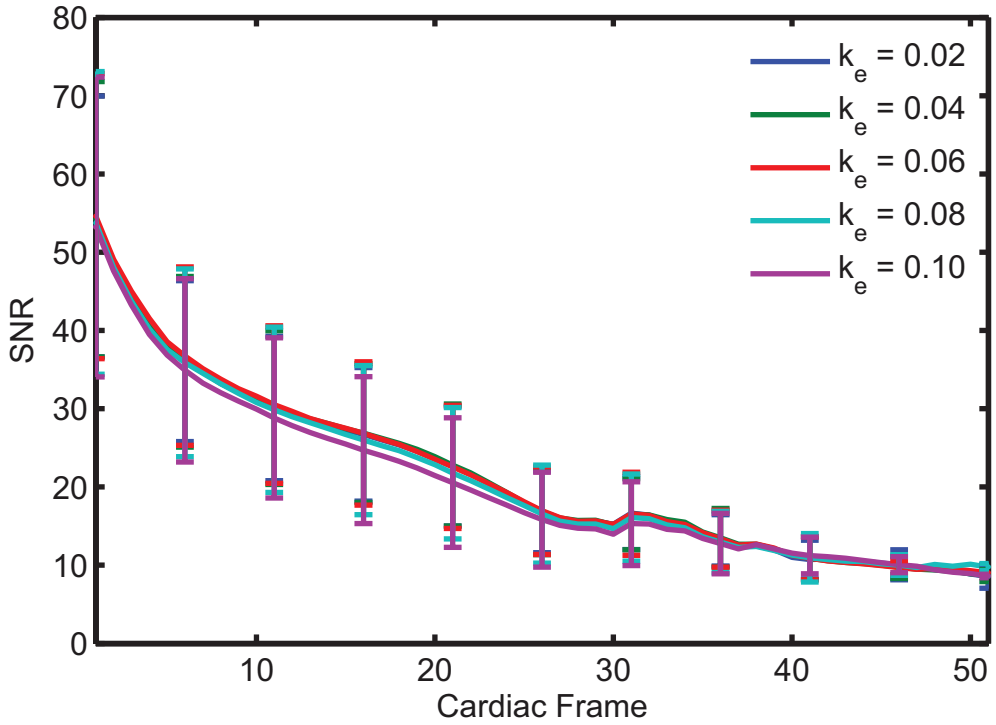

Figure 4.5: The SNR throughout the cardiac cycle was similar for the different k_e. Each curve represents the average of the 20 participants with standard deviation error bars. Starting with the first frame, the standard deviation is shown at every fifth cardiac frame for clarity. There is a trend towards higher SNR at lower k_e, particularly between the 15th and 20th cardiac frames.

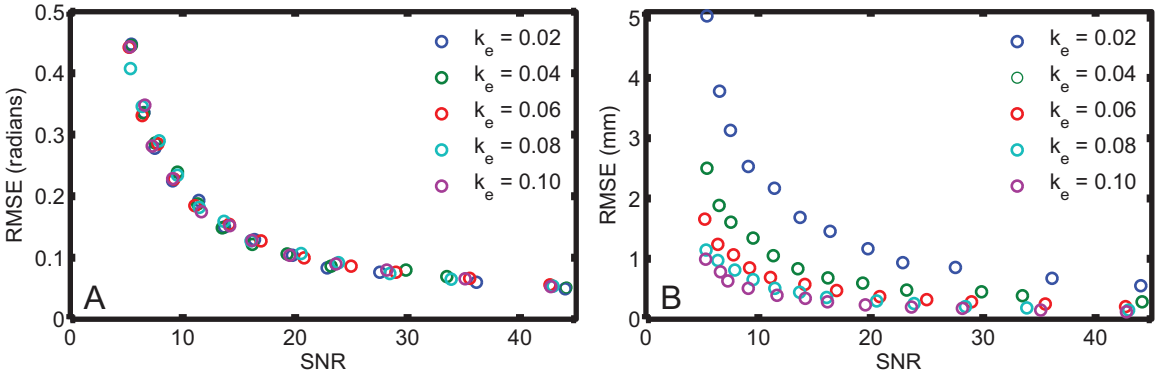

Figure 4.6: Phase noise had a larger effect on displacement errors with lower k_e. (**A**) In a stationary water phantom, phase noise, as quantified by RMSE in radians, was inversely related to SNR. No differences in RMSE were seen between the different k_e. (**B**) When RMSE in radians was converted to millimeters by dividing by k_e, there were substantial differences between the different k_e. Lower k_e had increased displacement errors.

4.3.5 Relationship Between Phase Noise and SNR

In the stationary water phantom, the inverse relationship between the phase noise (as measured by RMSE in radians) and the SNR was similar for all k_e (Figure 4.6a). However, the RMSE in millimeters, which required division by the appropriate k_e, was substantially higher for lower k_e (Figure 4.6b). For example, for SNR near 20, the RMSEs in millimeters were 1.17, 0.60, 0.38, 0.30, and 0.23 mm, for k_e = 0.02, 0.04, 0.06, 0.08, and 0.10 cycles/mm, respectively.

4.4 Discussion

Spiral 2D cine DENSE has typically been acquired with a k_e of 0.10 cycles/mm.[47, 7, 45] This value is high enough to cause phase wrapping after only 5 mm of tissue displacement. In the present study, we investigated the hypothesis that lower k_e could be used to reduce the amount of phase wrapping without compromising the quantification of strain and twist from mid-ventricular short-axis images. Our primary findings included: 1) the k_e can be reduced to 0.04 cycles/mm without causing differences in the quantifications of circumferential

strain, radial strain, or twist; 2) phase wrapping can be eliminated from the phase images with the use of k_e less than or equal to 0.04 cycles/mm; 3) the rate of blood pool dephasing, which is a source of contrast between blood and myocardium in the magnitude images, is similar for k_e between 0.02 and 0.10 cycles/mm; and 4) the SNR at end-systole is 9% higher when using a k_e of 0.04 cycles/mm compared to using a k_e of 0.10 cycles/mm.

4.4.1 DENSE Strain and Twist Analyses

Spiral cine DENSE is primarily used to measure cardiac displacements and deformation in the forms of twist and strain.[13, 29, 6] The k_e is the proportionality constant between the tissue displacement in millimeters and the measured signal phase. It also determines the strength of the encoding gradient that is applied. A high k_e provides high sensitivity to small displacements, but at the cost of intra-voxel dephasing and increased phase wrapping. The results from this study suggest that the k_e can be lowered to 0.04 cycles/mm, which significantly reduces the presence of phase wrapping, without compromising measures of circumferential strain, radial strain, or twist. In addition, studies that use different k_e between 0.04 and 0.10 cycles/mm can be directly compared as no systematic differences in strain or twist due to differences in k_e were found. This is valuable as not all DENSE studies have used the typical value of 0.10 cycles/mm. In particular, some previous studies have used 0.06 cycles/mm,[6, 9] which is within the range of the k_e found to be comparable to 0.10 cycles/mm in the current study.

The measures of strain and twist were compromised as the k_e was lowered to 0.02 cycles/mm. This was likely caused by the increased effect of phase errors at low k_e. For a given phase error in radians, the corresponding error in displacement (mm) was larger for lower k_e. This same phenomenon is present in phase contrast velocity imaging as the velocity encoding (VENC) is increased.[58]

4.4.2 Phase Wrapping

The amount of phase wrapping decreased as the k_e was decreased. Lowering the k_e to the point that there is no wrapping puts DENSE on a similar level as phase contrast velocity imaging, where the VENC is commonly adjusted to prevent wrapping in the blood velocities.[59] The use of this low value was possible due to the artifact suppression techniques of CSPAMM [13] and through-plane dephasing.[27] As seen in the representative participant (Figure 4.2, no stripe artifacts were present in the images for the low k_e.

4.4.3 Blood Pool Dephasing

The rate of blood pool dephasing decreased as the k_e was decreased. However, the difference between the acquisitions with 0.10 and 0.02 cycles/mm was not large. By the fifth cardiac frame, the acquisition with 0.02 cycles/mm had approximately 7% more of its blood pool signal remaining. This difference was not practically significant as the delineation between the myocardium and the blood pool was still possible at the lowest k_e. The drop in blood pool signal through the cardiac cycle is due to dephasing.[29] This dephasing can be due to both in-plane and through-plane gradients. While the in-plane gradients necessarily changed with the k_e, the through-plane gradient remained constant for all acquisitions and likely contributed to the blood pool dephasing at similar rates for all k_e. Thus, the advent of through-plane dephasing removed dependence on high k_e to accomplish blood pool dephasing.

4.4.4 Signal to Noise Ratio

The SNR was 9% higher for k_e of 0.04 cycles/mm compared to 0.10 cycles/mm. This reflects the decreased intra-voxel dephasing that occurs due to the decreased gradient strengths that accompany lower k_e. This modest increase in SNR is generally beneficial and reduces phase noise.[53]

It is important to note that both the in-plane encoding gradient and the through-plane dephasing gradient are can produce intra-voxel dephasing of the stimulated echo in deforming tissue.[27] The voxel size in the through-plane direction was larger than the in-plane direction (8 mm vs. 2.8 mm). Thus, the amount of intra-voxel dephasing may have been largely controlled by the through-plane dephasing gradient, which was constant (0.08 cycles/mm) for all acquisitions in this study. Further increases in SNR could be possible by reducing the through-plane dephasing gradient, however, this value was chosen to cause more than one half cycle of dephasing across the 8 mm slice.[27] Reducing the amount of through-plane dephasing could lead to the presence of stripe artifacts in the images.

4.4.5 Limitations

This study assessed a single mid-ventricular short-axis slice without consideration of long-axis images. The longitudinal motion of the left ventricle (particularly near the base) is often larger than the circumferential and radial components.[33] Long-axis images would likely have demonstrated phase wrapping with a k_e of 0.04 cycles/mm. While this implies that unwrapping algorithms cannot be removed from the post-processing, the amount of wrapping can be substantially reduced with a lower value. As the circumferential and radial strains were not compromised in the short-axis images with this low value, the longitudinal strains from the long-axis images should also not be compromised.

The acquisitions in this study were performed at 3.0 T, which yields higher SNR compared to 1.5 T.[49] Acquisitions at 1.5 T may have larger phase errors (due to decreased SNR) than those present in this study. However, those errors could be offset by better field homogeneity at the lower field strength. It has recently been reported that the displacement errors from spiral cine DENSE are the same at 3.0 T and 1.5 T.[8] Thus, the results from this study are likely applicable to 1.5 T.

We performed the acquisitions in this study with the simple encoding strategy

because of the reported ability to handle phase wrapping due to k_e as high as 0.10 cycles/mm.[29] A motivation for this study, however, was to investigate the ability to lower the k_e during acquisitions that use the balanced encoding strategy. This strategy has been used for DENSE acquisitions that encode displacements in all three directions.[25, 6, 9] However, in those studies, the k_e was reduced to 0.06 cycles/mm due to the increased wrapping that is present in the online reconstructed images.[25] We could not guarantee successful unwrapping from images acquired with the balanced strategy and a k_e of 0.10 cycles/mm, so the simple strategy was used to be able to accurately test up to 0.10 cycles/mm. The results from this study suggest that the k_e could likely be lowered to 0.04 cycles/mm with the balanced strategy, which has better noise performance than the simple encoding strategy.[25] This lower value would reduce the load on the unwrapping algorithm for 3D DENSE studies and any DENSE studies that use the balanced encoding strategy. The strain and twist results from this study suggest that these measures of cardiac mechanics would not be compromised with the lower value.

4.5 Conclusion

Cine DENSE is typically acquired with an encoding frequency of 0.10 cycles/mm.[47, 7, 45] This value allows for high sensitivity to tissue displacements, but at the cost of substantial phase wrapping. We demonstrated that the encoding frequency can be lowered to 0.04 cycles/mm to nearly eliminate phase wrapping without compromising the quantification of cardiac strains or twist. Future studies may take advantage of this lower value to reduce the amount of wrapping and simplify the input to unwrapping algorithms. In addition, studies performed with different encoding frequencies between 0.04 and 0.10 cycles/mm can be directly compared as there is no systematic bias.

CHAPTER 5

TYPICAL READOUT DURATIONS IN SPIRAL CINE DENSE YIELD BLURRED IMAGES AND UNDERESTIMATE CARDIAC STRAINS AT BOTH 3.0 T AND 1.5 T

5.1 Background

Chapter 4 presented the first step towards optimizing the spiral cine DENSE acquisition for measuring 3D displacements in the right ventricle (RV). Because measuring 3D displacements requires balanced displacement encoding, a low encoding frequency is desirable to prevent excessive phase wrapping. An encoding frequency as low as 0.04 cycles/mm was shown to substantially reduce phase wrapping without compromising the measurement of cardiac mechanics. A second optimization step was centered on ensuring a sufficient spatial resolution for imaging the thin RV wall. In general, this means that pixel size needs to be smaller than the thickness of the wall. However, spiral acquisitions, such as spiral cine DENSE, can be prone to blurring which effectively reduces the image resolution and may alter measured mechanics. This Chapter investigated the degree to which the typical spiral cine DENSE acquisition is impacted by blurring and how to mitigate it.

Phase contrast (PC) techniques encode motion into the phase of the magnetic resonance (MR) signal. Two examples include velocity-encoded PCMR [60] and Displacement Encoding with Stimulated Echoes (DENSE).[5, 13] Because DENSE encodes tissue displacement into the phase of the MR signal, spatial derivatives of the phase images yield measures of cardiac strains, which are valuable indicators of cardiac function.[4, 11] For improved signal to noise ratio (SNR) and better temporal and spatial resolution, cine DENSE is often acquired with a spiral readout.[47, 8, 6] Despite those benefits, spiral readouts are prone to blurring and

distortions from sources such as off-resonance and T2* decay.[61, 62] Measured cardiac strains could be particularly affected as blurring would be expected to dampen gradients in the phase images.

The spiral readout duration affects the amount of blurring that is present in spiral imaging. Longer readout durations allow more time for off-resonant spins to accumulate phase and for more T2* decay to occur. Both phenomena result in blurring in spiral imaging.[62] Spiral PCMR techniques have used readout durations between 11.75 and 14 milliseconds.[15, 60, 63] Similarly, two dimensional (2D) spiral cine DENSE is typically acquired with 6 spiral interleaves [47, 8, 6, 7, 45, 9, 26, 64] and a readout duration of 11.1 milliseconds. Field strengths of 3.0 T and 1.5 T are both common.[8, 6] We hypothesized that shorter readout durations would yield differences in image quality and measured cardiac strains at both 3.0 T and 1.5 T. Differences at 3.0 T would have high relevance for RV imaging while differences at 1.5 T would be relevant due to the common use of 1.5 T overall.

5.2 Theory

This section describes the major components of strain calculations and how blurring in DENSE images would be expected to alter the resulting quantifications of strain. To align with the approximately cylindrical geometry of the left ventricle, cardiac strains from short-axis views are commonly quantified in radial (E_{rr}) and circumferential (E_{cc}) directions. Specifically, cardiac strains from DENSE are quantified with the finite Lagrangian (Green) strain tensor E according to Equation 2.5 (13,18). In that equation, F is the deformation gradient tensor, which can be described by:

$$F = \frac{\partial \mathbf{x}}{\partial \mathbf{X}} \tag{5.1}$$

$\mathbf{X}$ is the initial location of a material point in the un-deformed state while $\mathbf{x}$ is

the location of that material point after deformation. If a tissue point is located at radius R and angle θ from the centroid of the LV in the un-deformed state, and if that tissue point experiences a radial displacement of u_r and an angular displacement of ω during deformation, then the 2D Cartesian locations can be written in terms of those variables:

$$X = \langle R\cos(\theta), R\sin(\theta)\rangle \tag{5.2}$$

$$X = \langle (R+u_r)\cos(\theta+\omega), (R+u_r)\sin(\theta+\omega)\rangle \tag{5.3}$$

After performing the spatial derivatives and matrix operations (Equations 5.1 and 2.5, respectively), the initial result is a Cartesian strain tensor in terms of R, θ, u_r, and ω. Following rotational transformation, the resulting polar strain tensor yields the following equations for E_{rr} and E_{cc}:

$$E_{rr} = \frac{\partial u_r}{\partial R} + \frac{1}{2}\left(\frac{\partial u_r}{\partial R}\right)^2 + \frac{1}{2}\left((R+u_r)\frac{\partial \omega}{\partial R}\right)^2 \tag{5.4}$$

$$E_{cc} = \left(\frac{u_r}{R} + \left(1+\frac{u_r}{R}\right)\frac{\partial \omega}{\partial \theta}\right) + \frac{1}{2}\left(\frac{u_r}{R} + \left(1+\frac{u_r}{R}\right)\frac{\partial \omega}{\partial \theta}\right)^2 + \frac{1}{2}\left(\frac{1}{R}\frac{\partial u_r}{\partial \theta}\right)^2 \tag{5.5}$$

Both E_{rr} and E_{cc} are sums of three terms. In each case, the first term is equivalent to fractional thickening or shortening and is the greatest contributor to the sum for physiologic deformations (see Young et al. [7] for an example of non-physiologic deformation where the third term is the sole contributor). For E_{rr}, the first term, $\frac{\partial u_r}{\partial R}$, is the gradient of radial displacement along the radial direction (i.e. across the LV wall). For E_{cc}, the first term is composed of both the ratio of radial displacement to initial radius as well as the gradient in twist along the circumference of the LV

wall, $\frac{\partial \omega}{\partial R}$. Due to the inward motion during cardiac contraction, a large component of circumferential strain is determined by the ratio. Furthermore, considering the entire ring of tissue, the net gradient in twist over the whole circumference is zero. The second terms are one half of the square of the first terms, which can be significant when the first term is large (*e.g.* for a fractional thickening of 0.50 (50%), the second term would contribute an additional 0.125 to the sum). The third terms are based on shears, which represent either the gradient in twist across the LV wall or the gradient in radial displacement along the LV circumference.

Due to the dependence on radial displacement for both E_{rr} and E_{cc}, the effect of blurring the DENSE phase images can be illustrated by simulating a ring of tissue experiencing wall thickening and inward contraction characterized by a linear gradient in radial displacement across the wall (Figure 5.1). When subjected to blurring, the measured displacement gradient is reduced compared to the prescribed gradient, such that the measured radial displacement at the inner circumference (endocardium) is erroneously low and the measured radial displacement at the outer circumference (epicardium) is erroneously high. Per Equation 5.4 for E_{rr}, this reduced gradient is equivalent to a reduction in measured radial strain. The effect of blurring on E_{cc} depends on where E_{cc} is measured. Because the measured radial displacement is erroneously low at the endocardium, the ratio of radial displacement to initial radius, and thus the magnitude of E_{cc}, is reduced. The opposite holds at the epicardium.

By considering typical values for LV radii, the relative magnitude of the effect of blurring on each strain can be estimated. Typical un-deformed dimensions of the LV are an inner radius of 24 mm and an outer radius of 33 mm, which yield a wall thickness of 9 mm.[65] If, for example, blurring caused radial displacement to be underestimated by 0.45 mm at the endocardium and overestimated by 0.45 mm at the epicardium, then the radial displacement gradient would be dampened by 0.9 mm per 9 mm of wall thickness. This represents a 10% (absolute) decrease in this

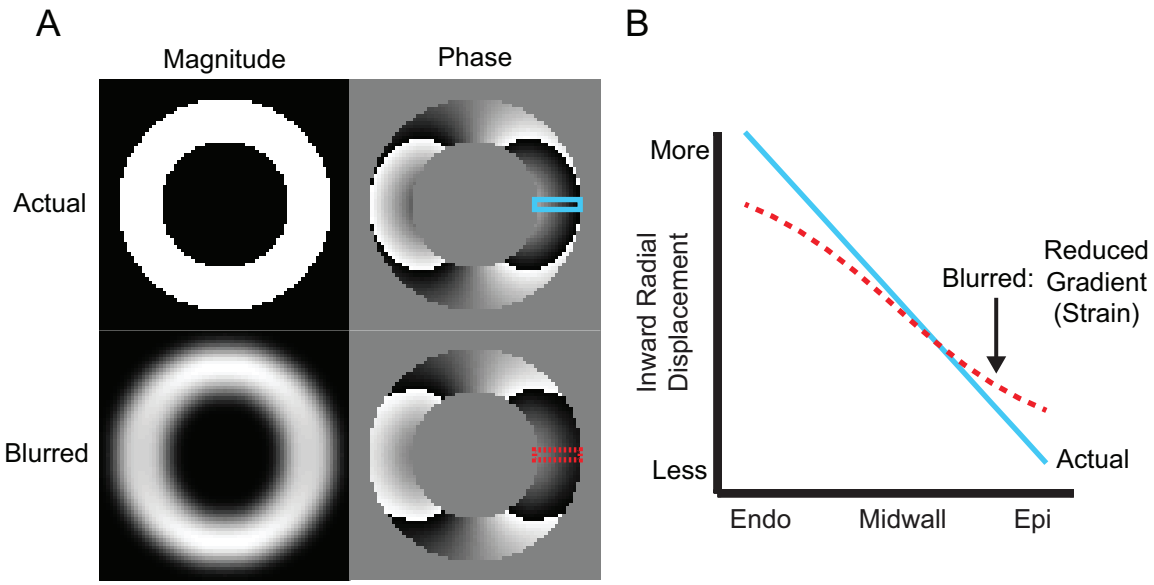

Figure 5.1: Illustration of blurring that causes a reduction in the observed radial displacement gradient. (**A**)In the short-axis view, the left ventricle can be approximated as a ring of tissue. The top row contains the magnitude and phase components from a simulated, complex DENSE image. Displacement in the x-direction has been encoded into the phase. The bottom row contains the results of blurring the complex image with a Gaussian filter. The magnitude image is clearly blurred while the differences in the phase image are visually subtle. (**B**) The prescribed gradient in displacement across the left ventricular wall is shown as the blue line and was taken from the top phase image. The dashed red line is the displacement gradient across the wall in the blurred phase image. There is a clear reduction in the measured displacement gradient (strain) across the wall in the presence of blurring. Endo: endocardial boundary; Epi: epicardial boundary.

gradient, which yields a similar reduction in measured E_{rr}. Alternatively, for E_{cc} at the endocardium, the ratio of radial displacement to initial radius would decrease by 0.45 mm / 25 mm (or 1.8% absolute). For E_{cc} at the epicardium, that ratio would increase by 0.45 mm / 33 mm (or 1.4% absolute). Thus, the effect of blurring on E_{rr} is expected to be several times larger than the effect on E_{cc}.

5.3 Methods

5.3.1 Computational Simulations

To expand on the illustrated theoretical blurring above, computational simulations of blurring due to off-resonance and T2* decay were performed for

different spiral readout durations using MATLAB (The Mathworks Inc, Natick, MA). Specifically, a ring of tissue with un-deformed endocardial and epicardial radii of 24 and 33 mm, respectively, was deformed based on a linear radial displacement gradient such that the endocardial and epicardial borders underwent 7.5 and 3.0 mm of inward radial displacement, respectively. Initial 2D DENSE images were simulated with the prescribed displacement encoded perfectly into the phase images using an encoding frequency of 0.10 cycles/mm. The DENSE images had a 2.8 x 2.8 mm pixel spacing, which is typical for human DENSE imaging. Pixels within the ring of tissue were given a uniform magnitude of unity, while pixels outside the ring had a magnitude of zero.

The k-space of the simulated images was then sampled along uniform density spiral trajectories. To assess different readout durations, the number of spiral interleaves was varied between 6 and 36, which corresponded to readout durations between 11.1 and 1.9 ms (Table 5.1). For all simulations, the time between readout samples along the spiral interleaves was 4 μs, and the number of samples was adjusted to maintain the same spatial resolution for all acquisitions. The 6-interleaves acquisition required 2784 samples along each interleaf and had the longest readout duration (11.1 ms). The 36-interleaves acquisition required 480 samples per interleaf and had the shortest readout duration (1.9 ms). Congruent with human spiral DENSE implementations,[8] the spiral interleaves sampled a circular region of k-space within a matrix of 102x102, which was then zero-padded to 128x128 before reconstruction. During the simulations, global off-resonance frequencies of 0, 30, and 60 Hz as well as global T2* constants of infinity, 25, and 5 ms were applied. These values span the range of off-resonance and T2* found in healthy participants at 1.5 T.[66] Image reconstruction was performed using gridding with a Kaiser-Bessel kernel and without corrections for the applied off-resonance or T2* decay.

Table 5.1: Spiral DENSE readout parameters

Number of Interleaves	Readout Samples	Readout Duration (ms)	Number of Heart Beats
6	2784	11.1	20
8	2112	8.4	26
10	1696	6.8	32
12	1408	5.6	38
14	1216	4.9	44
16	1056	4.2	50
18	928	3.7	56
20	864	3.5	62
22	768	3.1	68
24	704	2.8	74
30	576	2.3	92
36	480	1.9	110

Due to both the inability of spiral interleaves to sample the corners of k-space and the reduced resolution of the spiral sampling (102 vs 128), even perfect sampling along the interleaves followed by perfect gridding would be unable to exactly reconstruct the initial simulated DENSE images. To obtain an appropriate reference, the Cartesian k-space of the initial simulated images was replaced with zeros for all frequency points that were beyond the circular region sampled by the spiral interleaves. Reference images were then reconstructed via inverse Fourier transform to obtain the best possible images that could result from spiral k-space sampling.

5.3.2 Participant DENSE Imaging

This protocol was approved by the local Institutional Review Board and five healthy male participants (age 26 $\pm$ 2 years) without history of cardiovascular disease gave informed consent. For each participant, acquisitions took place at both 1.5 T and 3.0 T on an Aera and Trio, respectively (Siemens, Erlangen, Germany). The time between acquisitions on the respective Aera versus Trio was 2 days or less for all

participants. A 6 element chest and 24 element spine coil were used at 3.0 T, while 18-element chest and 12-element spine coils were used at 1.5 T. At 3.0 T and before DENSE acquisitions, a cardiac-gated field map was acquired during a breath-hold and used for 2^{nd} order shimming.

Standard localizers were used to plan a four-chamber balanced steady state free precession cine image. A single mid-ventricular short-axis slice was then planned perpendicular to the four chamber image at end-systole. The short-axis slice was planned parallel to the mitral valve plane and located 50% of the distance between the endocardial LV apex and the mitral valve plane. With an established spiral sequence,[8, 6, 25] short-axis 2D cine DENSE images were acquired with the following parameters: 2 spiral interleaves acquired per temporal frame, 360x360 mm^2 field of view, 128x128 image matrix, 8 mm slice thickness, 1.08 ms echo time, 17 ms repetition time, 20° constant flip angle. Simple encoding [25] with an encoding frequency of 0.10 cycles/mm [26] was used to measure in-plane displacements while through-plane dephasing of 0.08 cycles/mm [27] and CSPAMM [13] were used for echo suppression.

To assess different readout durations in the same manner as the simulations, the short-axis slice was acquired multiple times with readout durations between 1.9 and 11.1 ms. The properties of the spiral interleaves were the same between the human acquisitions and the simulations (Table 5.1). The order of the DENSE acquisitions was randomized for each participant. During each repetition time, a DENSE encoding gradient, a spiral readout, and spoiling gradients were played out. While acquisitions with shorter spiral readout durations could allow for shorter repetition times and, thus, either better temporal resolution or the acquisition of more than 2 interleaves per heartbeat, there are significant SNR penalties associated with sampling the longitudinal magnetization more frequently. In order to control the temporal resolution and SNR, the repetition time was the same for all acquisitions.

All DENSE acquisitions were performed with a respiratory navigator

(acceptance window = ±3 mm) prescribed at the dome of the liver. Image reconstruction was performed online with gridding via a Kaiser-Bessel kernel and typical linear corrections for partial compensation of off-resonance.[6, 67] The field maps for the linear corrections were acquired during 2 heartbeats within each DENSE acquisition. The linear corrections for off-resonance were based on a plane fit to the field map data. Fat suppression was applied with each acquisition. Images with different numbers of interleaves were compared visually to assess the presence of blurring artifacts.

5.3.3 DENSE Strain Analysis

Cardiac strains were derived from both the simulated and participant DENSE images as previously described using DENSEanalysis, a custom software written in MATLAB that is available at https://github.com/denseanalysis.[29, 28] The post-processing steps for each cine DENSE slice included manual segmentation of the left ventricular myocardium and semi-automated phase unwrapping to obtain the 2D displacements within each cardiac frame.[29] Following the unwrapping, typical spatial smoothing and temporal fitting of displacements (10^{th} order polynomial) were performed as previously described to obtain smooth trajectories for all tissue points beginning at end-diastole and continuing beyond end-systole.[29] Radial strain and circumferential strain were quantified from the resulting displacement fields for each cardiac frame with the 2D Lagrangian Green finite strain tensor in six circumferential segments throughout the cardiac cycle. Radial strain was defined as positive for thickening while circumferential strain was negative for shortening. To report peak global strains, the curves from the six segments were averaged into a single global curve from which the peak was selected. For circumferential strain both globally and segmentally, the strains were reported at different transmural regions (subendocardial, midwall, and subepicardial).

5.3.4 Statistics

For each peak strain, a Pearson correlation was performed with the mean of the five participants against the readout duration to determine if the measured strain was significantly dependent on the readout duration. An ordinary linear regression between the mean strain and the readout duration was performed to assess the change in measured strain per millisecond of readout duration.

5.4 Results

5.4.1 Computational Simulations

Simulations with longer readout durations were more susceptible to blurring from off-resonance and T2* decay. With an 11.1 ms readout, both off-resonance and T2* decay resulted in blurred magnitude images as well as altered phase images (Figure 5.2A). In contrast, the images from a 1.9 ms readout were largely unaffected even in the worst simulated case (60 Hz of off-resonance and a T2* of 5 ms).

Consistent with theory, the measured radial strain in the presence of off-resonance and T2* decay was dependent on the readout duration such that longer readouts underestimated radial strain (Figure 5.2B). In the worst simulated case, the measured radial strain was underestimated by 21% (absolute) compared to the reference. Measured circumferential strain in the presence of off-resonance and T2* decay was dependent on both the readout duration and the location of the measurement (Figure 5.2C). Longer readouts underestimated the magnitude of circumferential strain at the subendocardium while overestimating at the subepicardium. The amount of error was lower than that for radial strain. The largest error was 1.8% (absolute) in subendocardial circumferential strain during the worst simulated case. Both the direction of the errors in circumferential strain and their relative magnitude compared to errors in radial strain were consistent with theory.

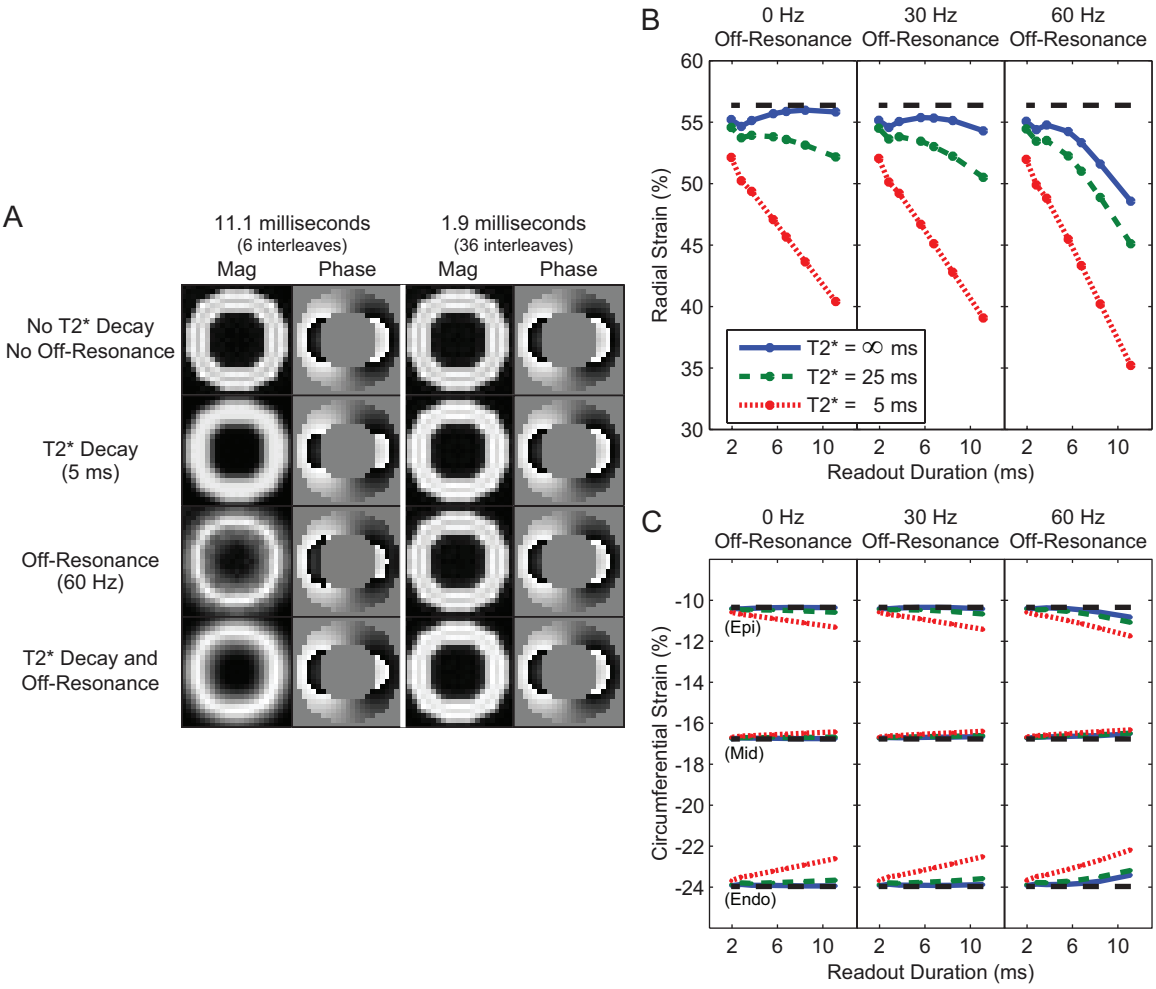

Figure 5.2: Simulations of longer readout durations in the presence of off-resonance and T2* decay yield blurred images and erroneous strain measurements. (**A**)Simulations with longer readout durations were more susceptible to blurring from off-resonance and T2* decay. (**B**) Radial strain was underestimated as the readout duration increased in the presence of off-resonance and T2* decay. The dashed line represents the measured strain from the reference simulation. (**C**) Measured circumferential strain was also altered with longer readout durations in the presence of off-resonance and T2* decay, however the magnitude was less than that of radial strain and the direction was dependent on the location of the measurement (Epi: epicardium; Mid: midwall; Endo: endocardium).

5.4.2 Participant DENSE Imaging

Compared to 1.9 ms readouts, magnitude images from 11.1 ms readouts showed blurring and distortions in the anterior and lateral segments of the left ventricle at both 3.0 T and 1.5 T (Figure 5.3). In phase images, however, artifacts were not visually obvious (Figure 5.4). The phase images were only subtly different between acquisitions with 11.1 and 1.9 ms readouts. The degree of blurring and distortions in the magnitude images was diminished as the readout duration decreased (Figure 5.5). For readouts $\leq$ 3.7 ms, the blurring and distortions were not visually apparent.

5.4.3 Participant Radial Strain

At 3.0 T, global radial strain and several segmental radial strains were significantly correlated with the readout duration (Figure 5.6A). Among the anterior and lateral segments of the left ventricle, measured radial strain decreased between 0.90 and 2.12% for every millisecond of readout duration. With a difference of 9.2 ms between the 11.1 and 1.9 ms readouts, those rates correspond to differences in measured radial strain of 8.3 and 19.5% (absolute). There was no correlation in the inferior and inferoseptal segments. Summary strain results from the 1.9 and 11.1 ms readouts are reported in Table 5.2.

Similar results for radial strain were present at 1.5 T (Figure 5.6B). The measured radial strains in the anterior segments were significantly and negatively correlated with the readout duration while the inferior and inferoseptal segments were not correlated. However, there was no significant correlation in the inferolateral segment or globally. Among the anterior segments, measured radial strain decreased between 1.03 and 2.13% per ms, which corresponds to differences of 9.5 and 19.6% (absolute) between the 11.1 and 1.9 ms readouts.

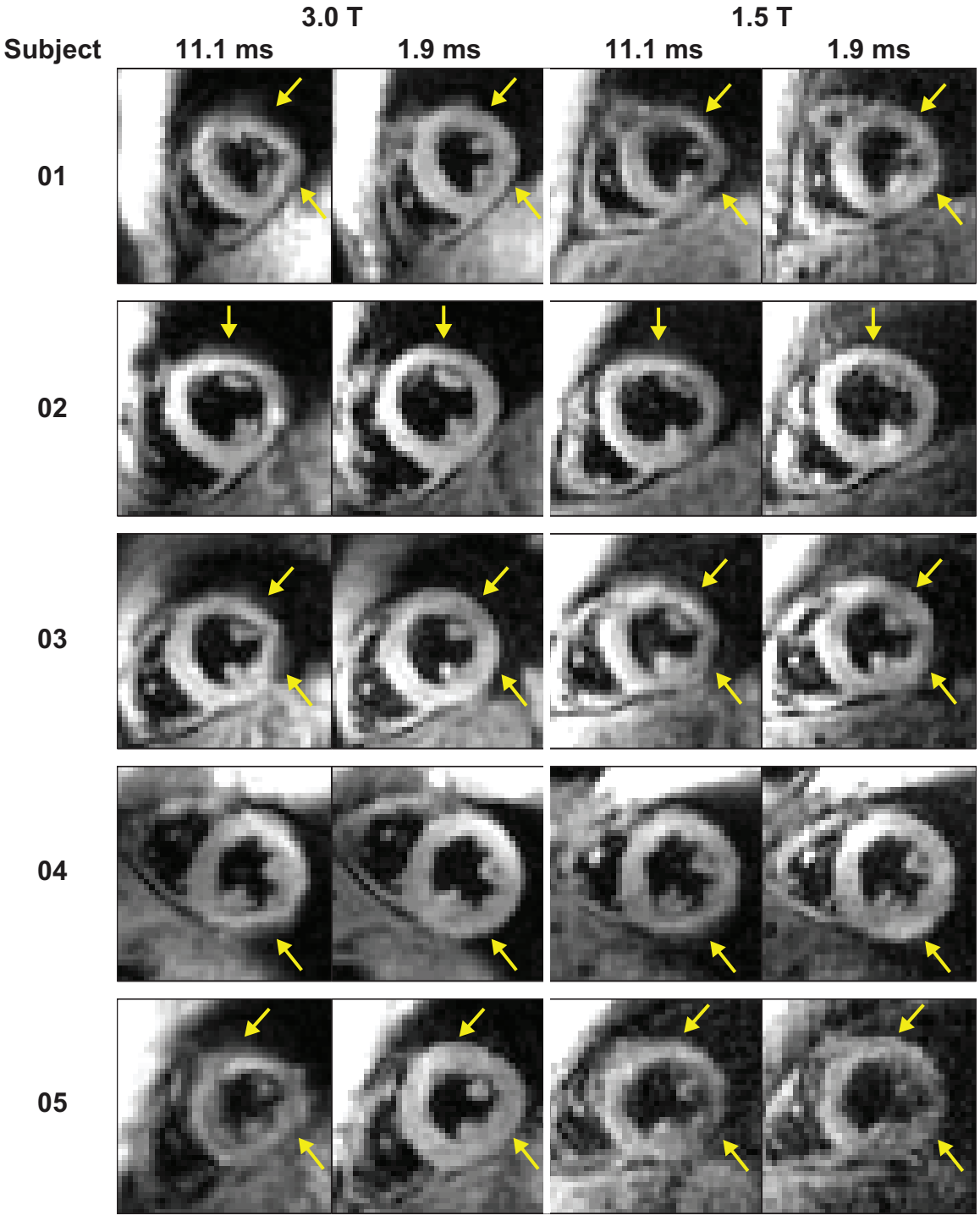

Figure 5.3: Acquisitions with 11.1 ms readouts demonstrated blurring and distortions in all participants compared to 1.9 ms readouts. The artifacts in the anterior and lateral walls of the left ventricle were variable between the participants. However, within each participant, the artifacts were similar in location and appearance at 3.0 T and 1.5 T.

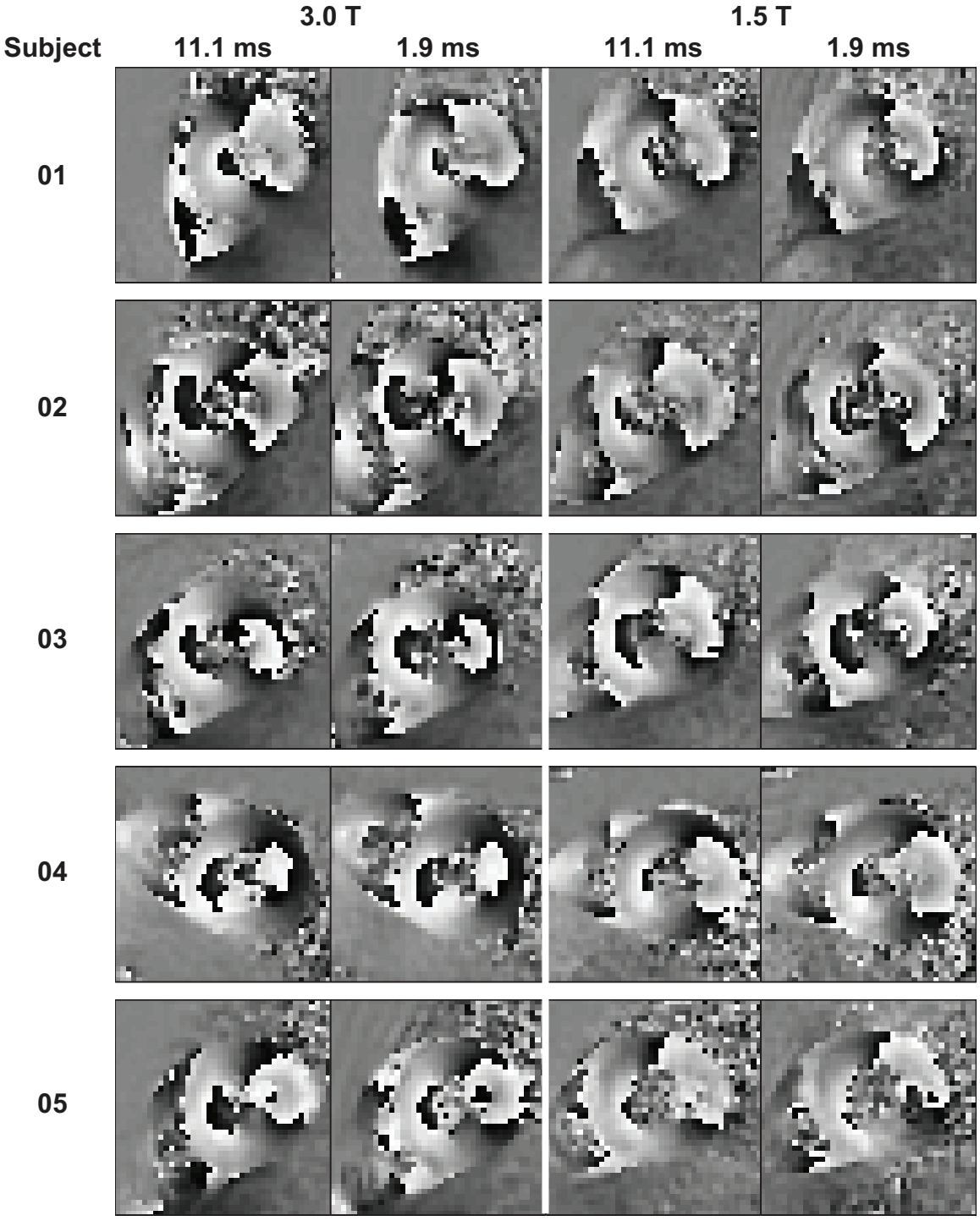

Figure 5.4: Phase images with displacement encoded in the x-direction were visually similar between acquisitions with 11.1 and 1.9 ms readouts. Blurring and distortion artifacts were not visually obvious in the phase images from 11.1 ms readouts.

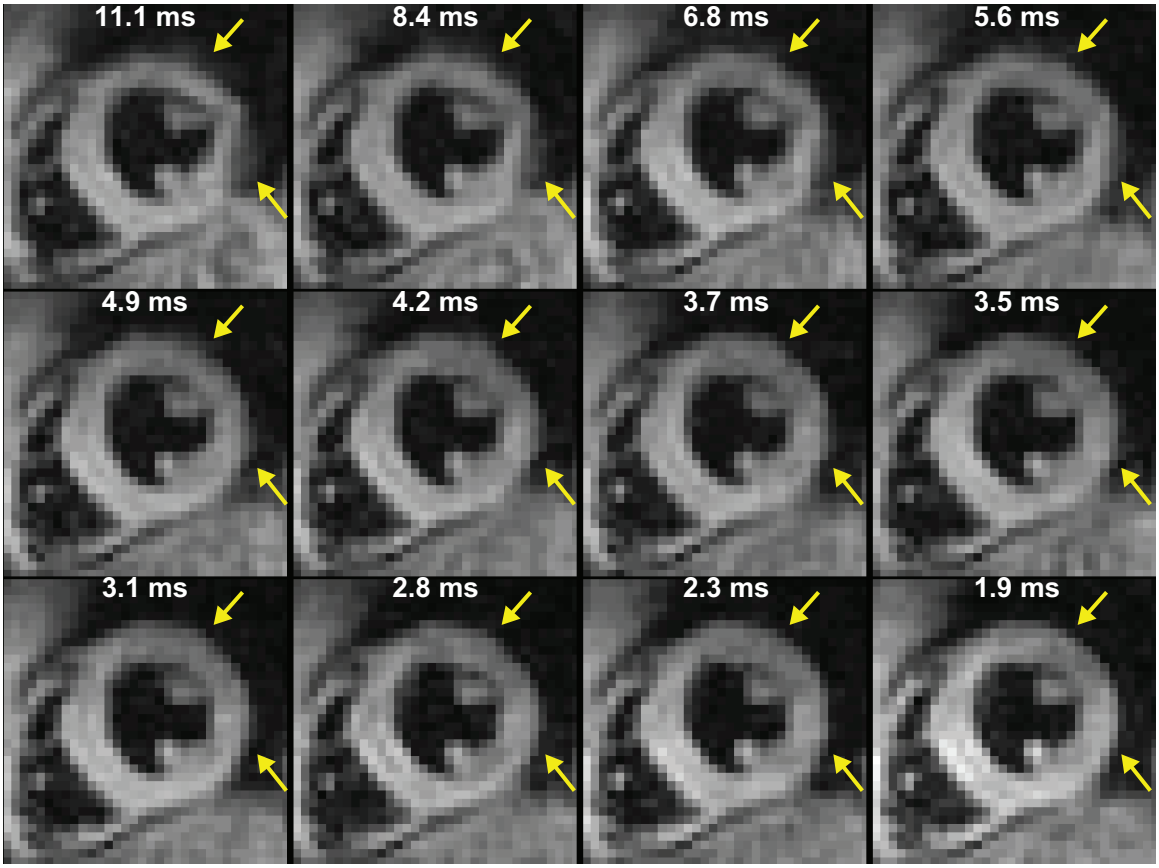

Figure 5.5: Blurring and distortions were diminished with decreasing readout duration. The white text indicates the readout duration. In this representative participant at 3.0 T, blurring and distortions were present in the anterior and lateral walls of the left ventricle with 11.1 ms readouts. These artifacts were not visually apparent with 3.7 ms or shorter readouts.

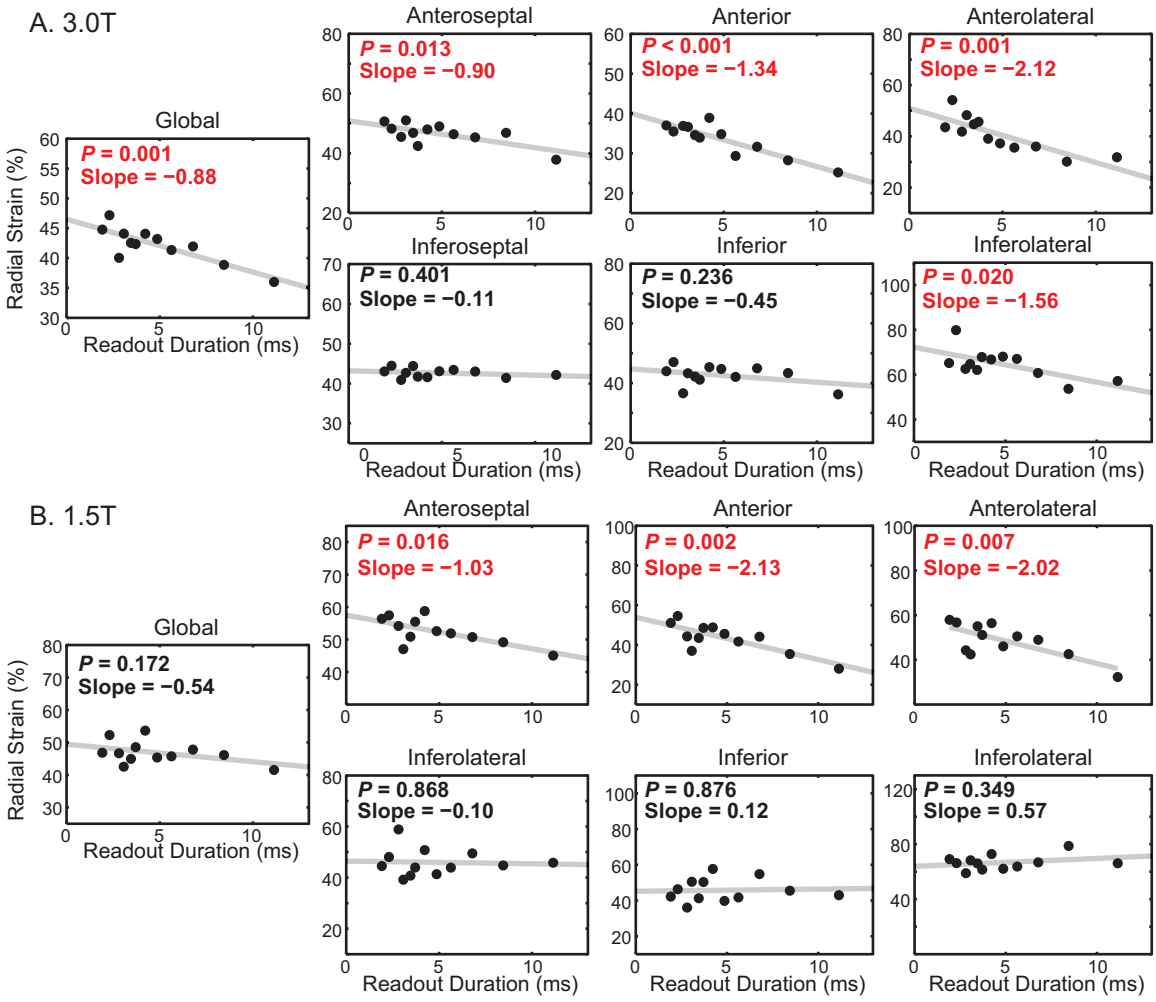

Figure 5.6: Radial strain was significantly correlated with the readout duration at both 3.0 and 1.5 T. In each plot, the mean of the participants is represented by the points. The gray line is the linear fit to the mean of the participants. Red text denotes statistical significance. Slope is reported in units of %/ms. A) At 3.0 T, anterior and lateral radial strains, as well as global radial strain, were significantly correlated with the number of interleaves. B) At 1.5 T, anterior radial strains were significantly correlated with the readout duration. However, unlike the results at 3.0 T, inferolateral and global radial strains were not significantly correlated.

Table 5.2: Mean (± standard deviation) strains from the 11.1 and 1.9 ms readout durations

	Radial Strain (%)		Circumferential Strain (%)					
Readout Duration			Sub-Endocardial		Midwall		Sub-Epicardial	
(ms)	*11.1*	*1.9*	*11.1*	*1.9*	*11.1*	*1.9*	*11.1*	*1.9*
3.0 T								
Global	36 ± 3	45 ± 5	-19 ± 1	-20 ± 1	-16 ± 2	-17 ± 2	-13 ± 2	-13 ± 2
Anterior	25 ± 9	37 ± 6	-19 ± 1	-21 ± 1	-15 ± 1	-17 ± 2	-12 ± 1	-13 ± 2
Anteroseptal	38 ± 13	51 ± 9	-18 ± 4	-19 ± 3	-15 ± 4	-15 ± 2	-12 ± 2	-11 ± 3
Inferoseptal	42 ± 10	43 ± 9	-18 ± 4	-19 ± 4	-14 ± 4	-15 ± 3	-12 ± 4	-12 ± 4
Inferior	36 ± 7	44 ± 16	-21 ± 3	-21 ± 3	-18 ± 4	-18 ± 2	-15 ± 4	-15 ± 3
Inferolateral	57 ± 26	65 ± 12	-23 ± 4	-22 ± 1	-21 ± 3	-20 ± 2	-18 ± 3	-18 ± 1
Anterolateral	32 ± 7	44 ± 10	-22 ± 3	-23 ± 2	-18 ± 3	-18 ± 3	-16 ± 3	-15 ± 3
1.5 T								
Global	42 ± 9	47 ± 12	-19 ± 2	-20 ± 3	-16 ± 1	-16 ± 2	-13 ± 2	-13 ± 2
Anterior	28 ± 7	51 ± 12	-20 ± 2	-21 ± 1	-17 ± 2	-17 ± 2	-14 ± 3	-13 ± 2
Anteroseptal	45 ± 3	56 ± 7	-18 ± 2	-19 ± 4	-14 ± 1	-16 ± 3	-12 ± 1	-13 ± 2
Inferoseptal	46 ± 10	45 ± 9	-17 ± 2	-18 ± 4	-13 ± 1	-14 ± 3	-11 ± 2	-11 ± 2
Inferior	43 ± 23	42 ± 17	-19 ± 2	-21 ± 4	-17 ± 2	-18 ± 4	-15 ± 2	-15 ± 4
Inferolateral	66 ± 27	69 ± 31	-23 ± 2	-24 ± 2	-20 ± 2	-21 ± 1	-18 ± 1	-17 ± 1
Anterolateral	32 ± 10	58 ± 22	-22 ± 2	-21 ± 4	-19 ± 3	-18 ± 4	-16 ± 3	-16 ± 3

5.4.4 Participant Circumferential Strain

At 3.0 T, significant correlations between the readout duration and circumferential strain were found globally and in the anterior segments (Figure 5.7A). For the subendocardial layer of affected segments, the magnitude of the circumferential strain decreased by between 0.147 and 0.159% per ms, which correspond to differences of 1.4 and 1.5% (absolute) between the 11.1 and 1.9 ms readouts. In the inferior segments, there were no significant correlations between circumferential strain and readout duration. At 1.5 T, there were few significant correlations between circumferential strain and the readout duration (Figure 5.7B). The sole significance was observed in the anterolateral segment. As with all reported strains in this study, no significant correlations were seen in the inferior or inferoseptal segments.

5.5 Discussion

Spiral cine DENSE is typically acquired with 6 interleaves and an 11.1 ms readout duration.[47, 8, 6, 7, 45, 9, 26, 64] The current study investigated whether shorter readout durations yield differences in image quality and measured cardiac strains at both 3.0 T and 1.5 T. Our primary findings included: 1) Computational simulations demonstrated that longer spiral readout durations in the presence of off-resonance and T2* decay yield blurred images, substantial reductions in measured radial strain, and mild errors in measured circumferential strain; 2) In participants, substantial blurring and distortions were present with 11.1 ms readouts compared to 1.9 ms readouts at both 3.0 T and 1.5 T; 3) the blurring and distortions were predominantly in the anterior and lateral segments of the left ventricle; 4) radial strain was substantially underestimated by the 11.1 ms readouts at both field strengths in the same segments where artifacts were present; and 5) circumferential strain was less dependent on the readout duration, but was mildly underestimated by the 11.1 ms readout in the

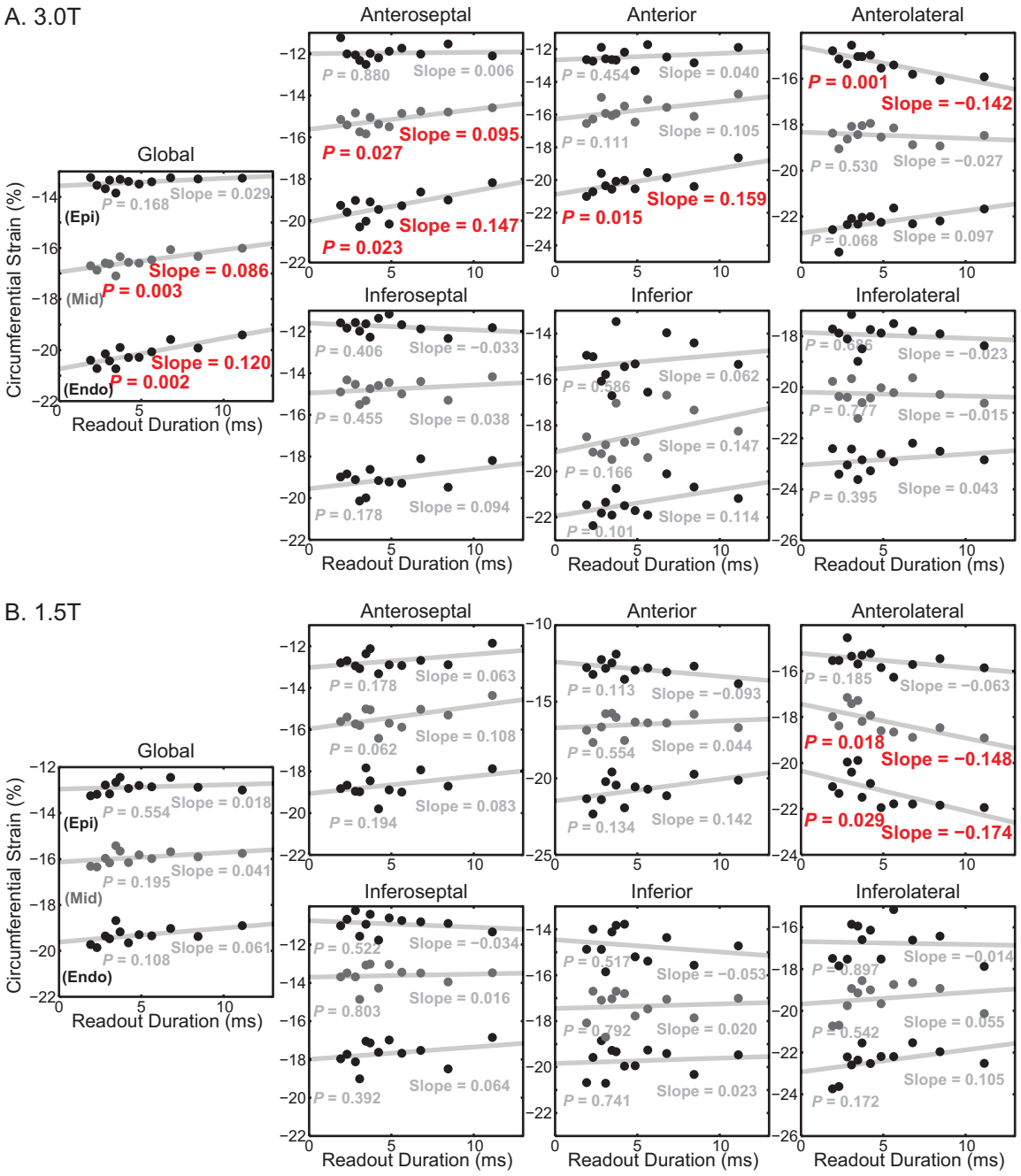

Figure 5.7: Circumferential strains were significantly correlated with the readout duration at 3.0 T. In each plot, the mean of the participants is represented by the points. The gray line is the linear fit to the mean of the participants. Red text denotes statistical significance. Circumferential strain was reported for the subepicardium (Epi), midwall (Mid), and subendocardium (Endo). Slope is reported in units of %/ms. A) At 3.0 T, global and anterior circumferential strains were significantly correlated with readout duration B) At 1.5 T, only the circumferential strains in the anterolateral segment correlated with the readout duration.

subendocardial layer at 3.0 T.

5.5.1 Computational Simulations

Spiral acquisitions are prone to blurring with longer readout durations due to phenomena such as off resonance and T2* decay. Because blurring affects the entire complex signal, and not just the magnitude, measurements from quantitative phase contrast techniques like DENSE may be dependent on the amount of blurring. The equations for radial and circumferential strain suggest that, for physiologic cardiac deformation, measured radial strain will be substantially reduced in the presence of blurring while the effect on circumferential strain will be milder. Computational simulations of off-resonance and T2* decay resulted in blurred images and alterations in the measured strains that were consistent with this theory.

5.5.2 Participant Imaging and Strains

In participants, blurring and distortions were present with longer readout durations and had similar appearance between 3.0 T and 1.5 T. The anterior and lateral segments of the left ventricle were predominantly affected. This is consistent with the presence of the lung-heart interface as well as the existence of epicardial veins carrying deoxygenated blood.[66] Tissue-air interfaces and tissues with susceptibility differences are prone to generating off-resonance and T2* decay artifacts.[66]

Radial strain was substantially underestimated by up to 19.6% (absolute) with 11.1 ms readouts in the anterior and lateral segments at 3.0 T and in the anterior segments at 1.5 T compared to the 1.9 ms readouts. Notably, artifacts were typically observed in these segments within the magnitude images. Subendocardial circumferential strain was also generally underestimated by the 11.1 ms readout, but to a lesser extent, consistent with theory. Small differences were seen globally and in some anterior segments at 3.0 T. No differences in either radial or

circumferential strain were seen in the inferior and inferoseptal segments, which was consistent with the lack of visual blurring artifacts in those regions.

To put the strain differences in context of the reproducibility of spiral cine DENSE, a previous study reported inter-test Bland-Altman limits of 13% and 2% for global radial and global circumferential strains, respectively.[26] The differences in strain between the different numbers of interleaves in the current study were on the order of the reported Bland-Altman limits. While the observed differences were about the same magnitude as known inter-test variability, inter-test variability would not explain the consistent directionality of the differences (e.g. radial strain was consistently underestimated when using longer readout durations). Our results also suggest that phenomena such as off-resonance and T2* may contribute to inter-test variability due to their effects on measured strains and their possible variability between imaging sessions.

The strain values reported in this study are similar to those from previous studies. One study with 6 interleaves (11.1 ms readout) conducted at both 3.0 T and 1.5 T reported global strain results that are within the above limits of agreement compared to the current study.[8] At 3.0 T, they reported 28.4 ± 7.1% and -18.1 ± 2.1% for radial and circumferential strain, respectively; at 1.5 T, they reported 41.6 ± 10.1% and -18.2 ± 0.8% for radial and circumferential strain, respectively.[8] The strains from 11.1 ms readouts in the current study also compare well with results from another study with 6 interleaves at 1.5 T.[7] No previous studies of readout durations down to 1.9 ms exist for comparison.

5.5.3 Previous Validations of Spiral Cine DENSE

Validation of the spiral cine DENSE sequence with 6 interleaves and 11.1 ms readout duration has previously been performed in several ways: radial and shear strain comparisons in a non physiologic deforming phantom at 1.5 T,[7] radial and circumferential strain comparisons to measurements from tagged MRI at 1.5 T,[7]

and a comparison of displacement error relative to tagged MRI at 3.0 T versus 1.5 T.[8] While these techniques were appropriate, they did have limitations that restricted their abilities to detect the effects that were evaluated in the current study. The phantom study likely did not reproduce field inhomogeneities that are present due to human anatomy and it assessed non-physiologic motion.[7] The comparisons with strain results from tagged MRI were subject to any errors or variability associated with tagged images and their image processing.[7] The comparison of DENSE displacement error between 3.0 T and 1.5 T (Chapter 2) utilized the acquisitions at 1.5 T as a reference and found no differences between displacement errors at 3.0 T compared to 1.5 T.[8] This suggested that spiral cine DENSE at 3.0 T was not demonstrably worse than spiral cine DENSE at 1.5 T, but it could not detect any errors associated with DENSE at 1.5 T. Hence, the present findings do not invalidate these previous comparisons, but do identify important sensitivities in the spiral DENSE acquisition that were not previously appreciated.

5.5.4 Implications

The typical 6-interleaves, 11.1 ms acquisition is likely sufficient for attempting to identify disease based on circumferential strain since the dependence of circumferential strain on readout duration was small. This is largely due to the relative insensitivity of circumferential strain to small differences in measured tissue displacement.

For radial strain, the dependence was much stronger, particularly in the anterior and lateral segments. For studies with a specific interest in segmental radial strains, 11.1 ms readouts are limited and likely inappropriate. Similarly, for studies on the detailed structure, deformation, and tissue properties of the left ventricle, 11.1 ms readouts are not recommended. The blurring and distortions in the magnitude images compromise the extracted geometry of the ventricle while the phase images yield dampened strains. The blurring was not visually apparent in acquisitions with ≤ 3.7 ms readouts.

Future technical developments of spiral cine DENSE may allow for the realization of the quality of the 1.9 ms readout without requiring many heartbeats of acquisition time. It may be possible to replace the linear corrections for field inhomogeneities with more advanced algorithms.[68, 69, 70, 71] Recent advancements have also included zonal excitation around the heart,[72] which allows for a reduced field of view, and both parallel imaging and compressed sensing,[73] which allow for undersampling of k space data. The combination of these advancements is a promising future direction for accelerating the spiral cine DENSE acquisition while maintaining a short readout duration.[74]

While the present study utilized spiral cine DENSE, other spiral phase contrast techniques exist to measure blood and tissue velocities.[60, 15, 63] Readout durations between 11.75 and 14 ms have been reported.[60, 15, 63] Based on the results of this study, those readout durations may yield velocity encoded phase images that are compromised by their readout duration. In particular, identical problems would arise if spatial derivatives of the velocity-encoded images were used to calculate shear or strain rates. For other applications, including first pass perfusion and balanced steady state free precession imaging of the heart, much shorter spiral readout durations of between 1.5 and 7.1 ms have been used.[75, 76, 77]

5.5.5 Limitations

While no additional imaging technique was acquired as an objective reference (such as myocardial tagging), none was required to fulfill the purpose of the current study, which was to evaluate the dependence of both artifacts and measured strains on the spiral cine DENSE readout duration. In addition, the computational simulations served as reference that corresponded well with the participant results.

Acquisitions with more interleaves were necessarily longer (i.e. required more heart beats), which allowed more time for physiologic changes that could have their own effect on image quality and measured strains. However, the blurring and

distortion artifacts found in this study were present in acquisitions with fewer heart beats. It would have been possible to assess a limited number of different readout durations without large changes in acquisition time, however differences in spatial resolution, temporal resolution, and SNR would have been required, which likely have their own effects on measured peak strains. The chosen study design allowed for the same spatial and temporal resolutions, as well as the same SNR, between the different acquisitions.

With the small sample size used in this study, subtle differences in cardiac strains may have been missed in the cardiac segments that were least affected by the readout duration. However, the current sample size was sufficient for demonstrating the dependence of image quality and several measurements of cardiac strains on the spiral readout duration.

5.6 Conclusion

Blurring and distortions due to a long readout duration are present in spiral cine DENSE images acquired at both 3.0 T and 1.5 T using the typical 6-interleaves acquisition with 11.1 millisecond readout duration. These artifacts yield substantially reduced radial strains and mildly reduced circumferential strains in short-axis views of the left ventricle. Reducing the readout duration diminishes the presence of these artifacts. Clinical studies using spiral cine DENSE should acknowledge these limitations, while future technical advances should aim to accelerate the DENSE acquisition while replicating the quality of acquisitions which utilize shorter readout durations.

CHAPTER 6

RIGHT VENTRICULAR STRAIN, TORSION, AND DYSSYNCHRONY IN HEALTHY SUBJECTS USING 3D SPIRAL CINE DENSE MAGNETIC RESONANCE IMAGING

Adapted from: Suever JD, Wehner GJ, Jing L, Powell DK, Hamlet SM, Grabau JD, Mojsejenko D, Andres KN, Haggerty CM, Fornwalt BK. Right Ventricular Strain, Torsion, and Dyssynchrony in Healthy Subjects using 3D Spiral Cine DENSE Magnetic Resonance Imaging. IEEE Trans Med Imaging. 2017;36(5):1076-1085

6.1 Background

The results from the previous Chapters validated and optimized the spiral cine DENSE image acquisition in preparation for the accurate measurement of cardiac mechanics throughout the left and right ventricles. In Chapter 4, we found an acceptable value for the displacement encoding frequency (0.04 cycles/mm) that allowed for accurate quantification of cardiac mechanics without excessive phase wrapping. In Chapter 5, we found that using more spiral interleaves to reduce the readout duration yielded less blurring and more accurate measures of mechanics. This Chapter describes the final step, which is to acquire DENSE of the right ventricle (RV) and to then create an image processing pipeline that can handle the irregular shape of the RV to enable the calculation of cardiac mechanics in a manner that is equivalent to the typical scheme used in the left ventricle (LV). Several processing components were developed to realize this goal, and the final pipeline was used to analyze spiral cine DENSE images from 50 healthy participants to characterize normal RV mechanics.

Measures of LV cardiac mechanics are predictive of adverse cardiac events and poor clinical outcomes.[4] A multitude of studies have characterized LV function in

both healthy individuals and patients with impaired cardiac function using various imaging techniques and modalities. The role of the RV, however, remains less clear. While more traditional measures of RV function, such as mass and volumes, are known to play an important role in a number of pathologies including arrhythmogenic right ventricular cardiomyopathy (ARVC), RV hypertrophy, pulmonary hypertension, and congenital heart disease,[78, 79] very few studies have looked at advanced measures of function in the RV such as strain, torsion, and synchrony. These advanced measures of RV function may provide better insight into the progression and pathophysiology of these diseases and allow for earlier subclinical diagnosis.

The lack of studies on RV function is due in part to the technical difficulties of measuring cardiac mechanics in the RV. Its myocardium is much thinner (3–5 mm) than the LV myocardium and can only be imaged with a high resolution technique.[80] Furthermore, while the geometry of the LV is readily modeled as a prolate spheroid, the shape of the RV does not adhere to any standard coordinate system. The contraction is also complex with mechanical activation beginning at the apex and propagating longitudinally towards the outflow tract.[81] This complex shape and contraction make it difficult to measure RV function using a standard two-dimensional imaging plane. Taken together, these factors make imaging, processing, and quantifying RV function difficult.

Despite these difficulties, several modalities have been used to measure advanced cardiac mechanics in the RV. While echocardiography is the most widely used modality for assessing LV function, the acoustic windows into the RV are narrow or even non–existent in many individuals. Magnetic Resonance Imaging (MRI) can overcome this limitation thanks to excellent tissue contrast as well as its ability to assess complex structures using multi–slice imaging. Traditional cine Steady State Free Precession (SSFP) MRI has been combined with feature tracking techniques to assess RV mechanics;[82, 39, 83] however, feature tracking techniques traditionally

suffer from poor reproducibility, particularly when used to quantify regional strain, twist, and torsion. More advanced techniques such as 3D myocardial tagging have been used to measure bi–ventricular mechanics,[84] but the thin wall of the RV makes tracking tag intersection points (on the order of 8 mm) difficult, ultimately leading to a poor estimate of transmural cardiac function.

Three-dimensional cine Displacement-encoded (DENSE) MRI, however, is a technique in which the displacement of tissue is encoded directly into the phase of the MRI signal.[13, 6] By applying this technique in both the LV and RV, it is possible to map the three–dimensional displacement of any pixel within the myocardium over the cardiac cycle with high temporal and spatial resolution. Using this displacement information, cardiac strains and torsion can be computed for any region of the RV and LV.

While DENSE has been used widely to measure and characterize LV function in both mice and humans,[34, 7] very few studies have investigated its ability to assess RV function. In 2012, Auger *et al.* used three–dimensional cine DENSE to measure principal strains within the RV. Due to the limited spatial resolution of the technique at the time (2.8 mm in-plane resolution), the authors were only able to determine strain at the midwall of the myocardium. While this study represented a critical first step to understanding right ventricular function, transmural differences in strain have been shown to be important in the LV [85] and it would be beneficial to make such measurements in the RV as well. Moreover, this study was completed in a limited set of 5 volunteers and their post-processing framework did not include a local coordinate system adapted to the complex geometry of the RV. In this study, we sought to combine the advanced capabilities of 3D DENSE imaging with a robust post–processing framework to perform bi–ventricular assessment of cardiac mechanics including strain, torsion, and dyssynchrony. Our goal was to use this framework to characterize normal RV function in a cohort of healthy individuals and to compare

measures of RV mechanics with their LV counterparts.

6.2 Methods

6.2.1 Image Acquisition

All scanning for this study was performed on a 3.0 T Siemens (Erlangen, Germany) Tim Trio with a 6–element chest and 24–element spine coil. After acquiring the necessary localizing images, a single four-chamber image and a stack of 9–11 contiguous short–axis images were acquired spanning from the apex to the mitral valve plane at end–diastole. Spiral cine DENSE was acquired at each of the image locations with balanced 3D displacement encoding (Figure 6.1).[25] DENSE parameters included: 12 spiral interleaves, 1 average, 360x360 mm^2 FOV, 180x180 image matrix, 2.0x2.0 mm^2, 8 mm slice thickness, ramped 20° flip angle, 17 ms repetition time, 1.8 ms echo time, 0.04 cyc/mm encoding frequency,[26] two spirals per heartbeat (34 ms temporal resolution), and 3–point phase cycling for artifact suppression.[6, 10] Based on typical values of off-resonance and T2* decay, the estimated net spatial resolution from full width at half maximum analysis of the point spread function was 3.7 mm.[66] All acquisitions were performed using a respiratory navigator to eliminate respiratory artifacts and to ensure a consistent diaphragm position (acceptance window: ±3 mm / range: 7 mm).

6.2.2 DENSE Post–Processing

Briefly, after manual segmentation of the myocardium, the displacement–encoded phase images were unwrapped. A 3D radial basis function interpolant was fit to these displacements and the spatial derivatives were computed analytically to construct the deformation gradient tensor and subsequently the Cartesian Lagrangian strain tensor. Using a local coordinate system based upon the endocardial surface mesh, the Cartesian strains were transformed into radial, circumferential, and longitudinal strains. Regional analysis was performed using standard segmentations of the LV and

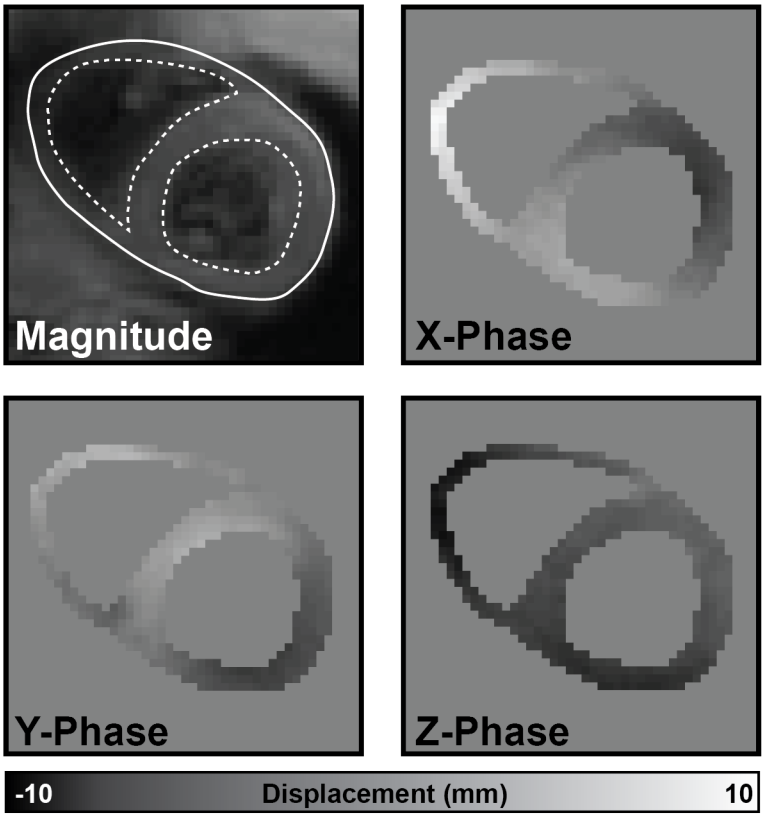

Figure 6.1: 3D spiral cine DENSE magnitude and phase images. RV and LV endocardial boundaries (dotted lines) and a combined epicardial boundary (solid line) were delineated on the magnitude image for all slices and cardiac phases. These boundaries were used to create a mask of the myocardium and unwrap the X, Y, and Z displacement–encoded phase images. Using these images, a 3D displacement field could be constructed.

a comparable segmentation of the RV. All analysis was performed for both the RV and LV simultaneously.

Myocardial Segmentation

For each short–axis slice and cardiac phase, RV and LV endocardial boundaries (dotted lines in Figure 6.1) and a combined epicardial boundary (solid line in Figure 6.1) were manually delineated on the combined black–blood magnitude images. All trabeculations and papillary muscles were excluded from the segmentation to isolate mechanics calculations to the true myocardium. The open–source *DENSEanalysis* software [28] with a custom plugin for bi–ventricular segmentation was used to perform all segmentation and phase unwrapping. From these boundaries, a mask was created for each short–axis slice. The X, Y, and Z displacement–encoded phase images were unwrapped using manual seed points and a quality–guided path following phase unwrapping algorithm.[29] All cardiac phases were visually inspected to ensure no phase unwrapping errors were present (Figure 6.1).

Cartesian Strain Tensor Calculation

The coordinates of all pixels within the myocardium were converted to 3D coordinates using the position information stored within the image headers. By combining the 3D coordinates of each pixel with the unwrapped X, Y, and Z Eulerian displacement vectors, a 3D displacement field was generated for each cardiac frame.

Previous work has often utilized a finite-element based analysis where a mesh is fit to the geometry of the myocardium and then deformed using the measured displacements in order to derive cardiac strains.[6, 84] This methodology requires algorithms to construct the volumetric meshes and care must be taken to control the arrangement and size of the elements. Furthermore, the computation of strains and

torsion from a displacement field are only dependent on the spatial gradients of the displacement field. We chose to compute the strains *analytically* from a continuous and differentiable interpolant of the displacement field.

Linear radial basis functions (RBFs, ϕ) were fit to the 3D Lagrangian displacement field.[86] The weights $\boldsymbol{\omega_i}$ in Equation 6.1 were determined using the 3D coordinates and measured 3D displacements. Using the position $\boldsymbol{x}$ of a query point, it was possible to determine the 3D displacement $\boldsymbol{D}$ of this point using the calculated weights $\boldsymbol{\omega_i}$ and the location of each of the M original data points, $\boldsymbol{x}_i$.

$$\boldsymbol{D}(\boldsymbol{x}) = \sum_{i=1}^{M} \boldsymbol{\omega_i} \phi(\|\boldsymbol{x} - \boldsymbol{x}_i\|) \tag{6.1}$$

To compute strains at any point, the deformation gradient tensor (F) was computed from gradients in the displacement interpolants at that point. D_x, D_y and D_z are the interpolants for the X, Y, and Z displacements, respectively. I is the identity matrix.

$$F = \begin{bmatrix} \frac{\partial D_x}{\partial x} & \frac{\partial D_x}{\partial y} & \frac{\partial D_x}{\partial z} \\ \frac{\partial D_y}{\partial x} & \frac{\partial D_y}{\partial y} & \frac{\partial D_y}{\partial z} \\ \frac{\partial D_z}{\partial x} & \frac{\partial D_z}{\partial y} & \frac{\partial D_z}{\partial z} \end{bmatrix} + I \tag{6.2}$$

All of the derivatives in Equation 6.2 were computed analytically using the coefficients from the RBFs fit to the displacement field. The Green Cartesian strain tensor E_c was then computed using Equation 2.5, ultimately yielding the tensor shown in Equation 6.3.

$$E_c = \begin{bmatrix} E_{xx} & E_{xy} & E_{xz} \\ E_{yx} & E_{yy} & E_{yz} \\ E_{zx} & E_{zy} & E_{zz} \end{bmatrix} \tag{6.3}$$

Local Coordinate System

The Cartesian strain tensor is not useful on its own for quantifying cardiac mechanics because the different components are dependent upon patient position and measurement position within the heart. To account for this dependency, Cartesian strains are typically transformed into a cylindrical coordinate system with radial, circumferential, and longitudinal components. In 2D LV analysis of a short–axis image, the radial direction is typically defined as pointing towards the centroid of the LV and the circumferential direction is defined as normal to this vector (within the same short–axis imaging plane). This works well for the mid-ventricular region of the LV but breaks down near the apex, where the true radial direction is angled out of the image plane and points towards the base, and in the RV where the geometry is non–cylindrical. To transform the Cartesian strain tensor to a polar strain tensor, we defined an adaptive local coordinate system based upon a surface mesh fit to the endocardial boundaries of the myocardial segmentation. The endocardial mesh generation methodology introduced by Haggerty et al. was used in this study.[87]

Radial $\boldsymbol{r}$, longitudinal $\boldsymbol{l}$, and circumferential $\boldsymbol{c}$ directions were defined for each vertex on the endocardial surface meshes of both the right and left ventricles. The radial direction was defined as the inward normal to the surface. The longitudinal direction was constrained to be tangent to the surface but pointing in the direction of the apex of the ventricle.

The apices of each ventricle were defined automatically from the point of maximum curvature of the LV and RV endocardial contours delineated on the four-chamber image. The four-chamber image was chosen for apex selection since it was planned such that it passed through the apices of the ventricles. These apical points on the 2D encodardial contours were then projected to the endocardial mesh of their respective ventricle to obtain the apical reference point for that ventricle.

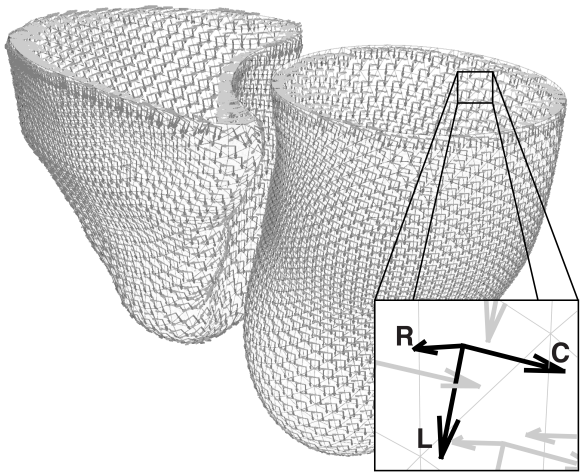

Figure 6.2: 3D Local coordinate system. For any point in either the left or right ventricle, a local coordinate system was defined with the radial direction (**R**) being the inward normal of the surface, the longitudinal direction (**L**) pointing towards the apex, and the circumferential direction (**C**) as the cross–product of the radial and longitudinal components.

The circumferential direction was then the cross product of the longitudinal and radial direction vectors (Figure 6.2).

The local coordinate system was used to construct a rotation matrix, R (Equation 6.4), that was then used to transform the Cartesian strain tensor, E_c, into the polar strain tensor E_p (Equation 6.5).

$$R = \begin{bmatrix} r_x & c_x & l_x \\ r_y & c_y & l_y \\ r_z & c_z & l_z \end{bmatrix} \tag{6.4}$$

$$E_p = R^T E_c R \tag{6.5}$$

Using this polar strain tensor E_p, it is possible to derive the radial (E_{rr}),

circumferential (E_{cc}) and longitudinal (E_{ll}) strains (Equation 6.6).

$$E_p = \begin{bmatrix} E_{rr} & E_{rc} & E_{rl} \\ E_{cr} & E_{cc} & E_{cl} \\ E_{lr} & E_{lc} & E_{ll} \end{bmatrix} \tag{6.6}$$

Torsion was quantified using the circumferential–longitudinal shear angle α_{cl} (in degrees) computed from the polar strain tensor using Equation 6.7.[88]

$$\alpha_{cl} = \arcsin \frac{2E_{cl}}{\sqrt{(1+2E_{cc})(1+2E_{ll})}} \tag{6.7}$$

In addition to the polar strains, principal strains were derived from the eigenvalues and vectors of the polar strain tensor, E_p. Because principal strains are invariant to rotations of the coordinate system, either E_c or E_p could be used to derive them.

6.2.3 Regional Analysis

The American Heart Association (AHA) 17–segment model is widely used for characterizing regional function within the LV.[89] This representation of the ventricle requires parameterization in both the longitudinal and circumferential directions. In order to perform similar regional analysis in the RV, it is necessary to develop a method that is flexible enough to handle the variable and irregular geometry of the RV.

For longitudinal parameterization, we used the normalized geodesic distance between the base and the apex for each ventricle independently. For every point in the endocardial surface mesh of each ventricle, we computed the geodesic distance of that point from both the apex of that ventricle as well as the base. We then used the ratio of these two distances to determine the normalized longitudinal distance. The heat method was used to compute geodesic distances across the surfaces meshes [90] using the freely available Geometry Processing Toolbox [91] (Figure 6.3).

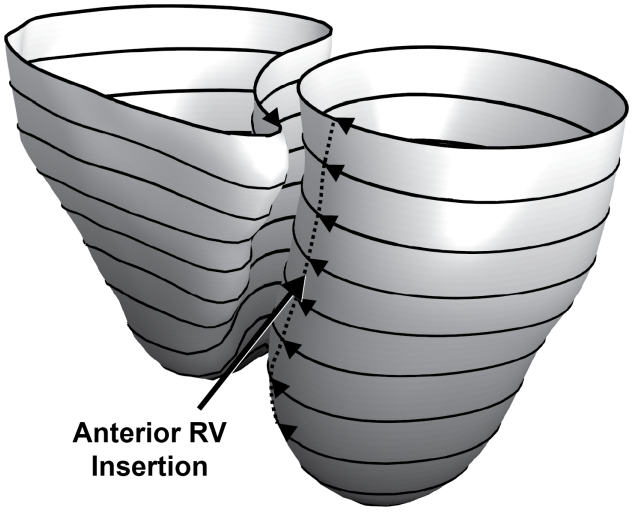

Figure 6.3: Longitudinal and circumferential parameterization. The normalized geodesic distance from the apex (0, black) to the base (1, white) was computed for each point on the encodardial surface for both the left and right ventricles to determine the longitudinal parameterization. Using the iso–value lines of the longitudinal parameterization (black rings), the circumferential position was parameterized using the normalized arc length of each iso–value line starting at the anterior insertion line of the right ventricle (dotted line) and continuing around the ventricles.

To perform circumferential parameterization, we determined the iso-value lines of the longitudinal parameterization (black lines in Fig. 6.3).[91] This provided us with paths that traversed the ventricle circumferentially. We normalized the arc length of each of these paths with zero being defined as the anterior insertion of the RV (dotted line in Figure 6.3). The anterior and inferior insertion points were defined automatically for each short–axis image by finding the points on the LV endocardial contour that had the lowest sum of distances to the other two contours (the RV endocardial contour and the epicardial contour).

Radial parameterization is important if transmural differences in strain are to be studied. It has been shown that different disease states affect the different layers of the myocardium preferentially.[85] Here we present a method to perform this transmural parameterization.

Radial parameterization was performed using a 3D version of a PDE–based

thickness measurement.[92] Using the endocardial and epicardial surface meshes, the region within the RV endocardium was defined to have a potential of 0 and the epicardium and LV endocardium were defined to have a potential of 1. The PDE–based approach solved the heat equation for any point within the myocardium. Then, this procedure was repeated except that the LV endocardium was set to 0 and the epicardium and RV endocardium were set to 1. For any point in the myocardium, its transmural position (normalized between 0 and 1) was defined as the minimum of the two results.

Using the circumferential and longitudinal parameterization of the endocardial surfaces, any point within the myocardium could be mapped to the nearest point on the endocardial surface mesh to determine its circumferential and longitudinal position. Using this information, the LV and RV were divided into segments (17 and 13 segments, respectively) and all mechanics derived from DENSE were averaged within each of these segments. The LV segmentation used the standard AHA 17–segment model while the RV segmentation used four equal segments longitudinally and four equal segments circumferentially between the anterior and inferior insertion points for all but the apex where a single circumferential segment was used.

Peak strain and torsion values were determined by averaging the time series of all sampled points within a segment. The peak value of this average curve was then used as the representative peak value from that segment.

Dyssynchrony Analysis

To assess regional timing, the second principal strain curve was computed for each segment. Contraction timing was measured throughout the LV and RV by computing the mechanical activation delay of each segment relative to a patient–specific reference curve using cross–correlation analysis.[93] Using the R-R interval, the delay times were converted from milliseconds to percent of the cardiac cycle. After obtaining a delay

time for each region, the dyssynchrony index (the standard deviation of segmental delay times) was computed for both the LV and RV. The septum was included with the LV, which is standard for the 17-segment LV model. The inter–ventricular delay time was computed as the difference between the median delay time of each ventricle with a positive value indicating that the LV contracts before the RV.[39]

6.2.4 Reproducibility Analysis

To determine the inter–observer reproducibility of the 3D post–processing pipeline, 10 datasets were selected at random and analyzed by a second observer. No restrictions were placed on the independent observers regarding which slices to use for the analysis (i.e., selecting the most apical and basal slices to segment). All metrics including global and regional torsion, strain and dyssynchrony were compared between the two observers using Bland-Altman analysis. Additionally, a modified coefficient of variation (CoV) was computed using Equation 3.1.

To assess inter–test reproducibility, we acquired two 3D DENSE datasets in 6 healthy individuals. Each of the two acquisitions was performed by a different technician and the participant was completely removed from the scanner between acquisitions. Reproducibility of strain, torsion, and dyssynchrony was again assessed via Bland–Altman analysis and the modified CoV.

6.3 Results

To characterize healthy RV function, we scanned 50 healthy participants (Age: 26 $\pm$ 8 years, 46% male) without history of cardiovascular disease. Volumes and ejection fractions as calculated from the endocardial surface meshes derived from the DENSE imaging are reported (Table 6.1). RVEDV may be underestimated due to exclusion of portions of the most basal region of the RV. All participants provided written and informed consent and the protocol used in this study was approved by the Institutional Review Board.

Table 6.1: Subject Characteristics

	Mean ± Std.	Range
Age (years)	26 ± 8	18 – 50
Height (cm)	173 ± 8	156 – 191
Weight (kg)	72 ± 13	43 – 106
Heart Rate (bpm)	67 ± 12	41 – 100
LVEF (%)	58 ± 4	47 – 69
RVEF (%)	53 ± 4	44 – 61
LVEDV (ml)	107 ± 28	49 – 175
RVEDV (ml)	91 ± 27	28 – 149
LVESV (ml)	45 ± 14	20 – 76
RVESV (ml)	43 ± 14	14 – 73

Bi–ventricular 3D imaging and post–processing were performed successfully on all 50 participants. Average scan time for the 3D data was 28 ± 6 minutes with an average respiratory navigator efficiency of 63 ± 10% (nominal scan time of 18 ± 5 minutes). Average time for manual segmentation of the myocardium of the left and right ventricles was 15 minutes per slice. The computational processing time on a 3.40 GHz CPU with 16.0 GB of RAM was 28 ± 18 minutes.

6.3.1 Cardiac Strains

Peak global circumferential strain for the RV had a similar magnitude to the values observed in the LV (−18.0 vs. −18.0%); however, global RV longitudinal strain had a higher magnitude than in the LV (−18.1 vs. −15.7%) (Table 6.2). Circumferential strain varied regionally within the RV with the lowest values (−16%) in the outflow region (Figure 6.4a). Longitudinal strain varied considerably throughout the RV free wall (11 – 24%) (Figure 6.4b).

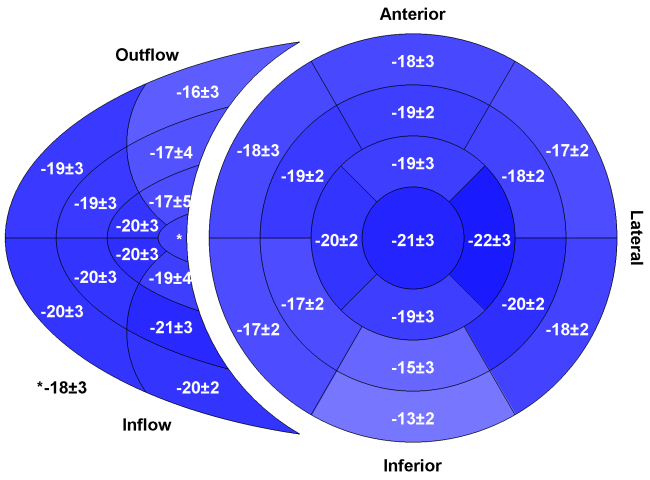

(a) Circumferential Strain

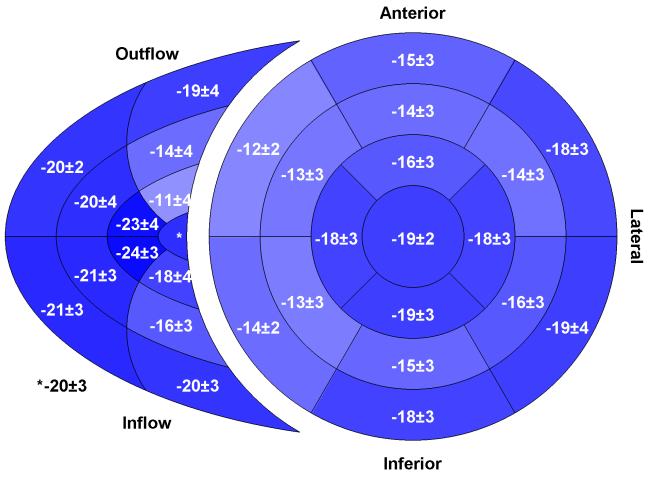

(b) Longitudinal Strain

Figure 6.4: Regional circumferential and longitudinal strains. Bi–ventricular segment model showing regional peak circumferential (a) and longitudinal (b) strain in both the left and right ventricles. All values are expressed as a percent. Segments with greater strain magnitude are shown with a darker shade of blue. The inner–most region of the right ventricular segment model is the apical portion while the outer-most is the basal portion. (n = 50)

6.3.2 Mechanical Activation Times

Mechanical activation times were computed for each segment relative to a patient-specific reference strain curve and were reported as percent of cardiac cycle. On average, the septum contracted first followed by the apex, the lateral wall of the RV, and finally the basal lateral regions of the LV (Figure 6.5). Globally, the RV contracted later than the LV (0.6 vs. 0.0%); however, once RV contraction began, it contracted more synchronously than the LV (dyssynchrony index: 3.1 vs. 3.3%) (Table 6.2).

6.3.3 Cardiac Torsion

Significant torsion was observed in the RV with comparable global magnitude to that observed in the LV (Table 6.2). The highest torsion values were seen in the lateral segments of the RV free wall and the basal lateral segments of the LV (Figure 6.6).

Table 6.2: Global Cardiac Mechanics

	Left Ventricle	Right Ventricle
Circumferential Strain (%)	-18.0 ± 1.8	-18.0 ± 2.0
Longitudinal Strain (%)	-15.7 ± 1.3	-18.1 ± 1.6
Radial Strain (%)	31.5 ± 8.9	–
Torsion (°)	7.1 ± 1.1	6.2 ± 2.0
[1,2]Delay Time (%)	0.0 ± 1.0	0.6 ± 1.0
[2]Dyssynchrony (%)	3.4 ± 1.0	3.1 ± 1.1
Dyssynchrony (ms)	25.0 ± 6.9	23.3 ± 8.3
[2]Inter–ventricular Dyssynchrony (%)	-0.0 ± 1.5	
Inter–ventricular Dyssynchrony (ms)	-0.7 ± 10.6	

[1]Negative is early contraction; Positive is late contraction

[2]Expressed as a percent of the cardiac cycle

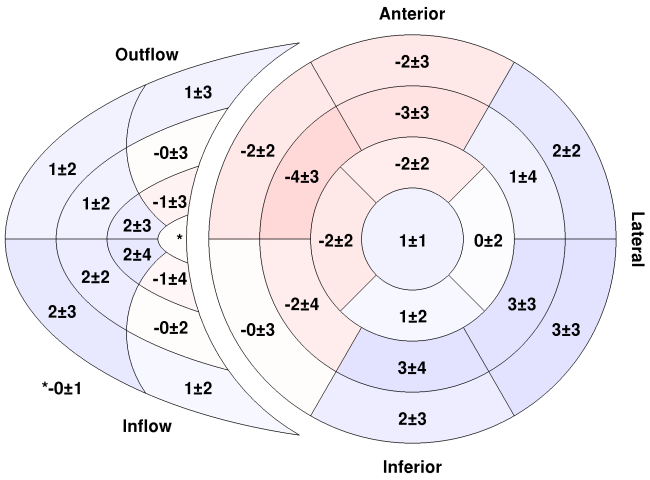

Figure 6.5: Regional delay times throughout both the right and left ventricles. A negative number (red) indicates an early–contracting segment while a positive number (blue) indicates a region with delayed mechanical contraction. All values are expressed as a percentage of the cardiac cycle. The inner–most region of the right ventricular segment model is the apical portion while the outer-most is the basal portion. (n = 50)

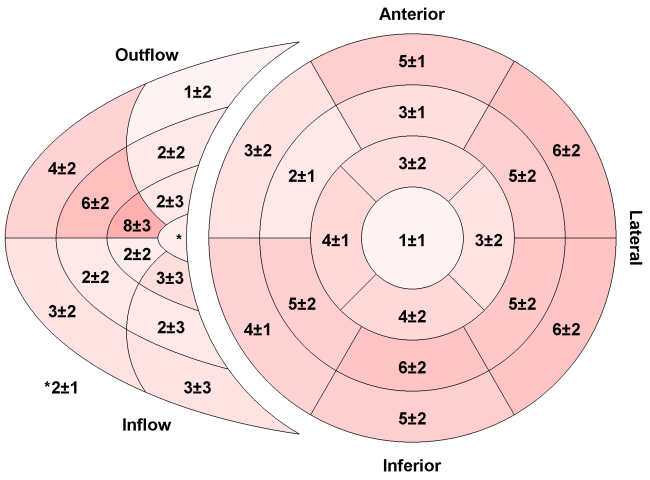

Figure 6.6: Regional torsion for the right and left ventricles. Torsion was computed from the circumferential–longitudinal shear angle and is expressed in degrees. Segments with greater torsion are shown with a darker shade of red. The inner–most region of the right ventricular segment model is the apical portion while the outer-most is the basal portion. (n = 50)

6.3.4 Reproducibility

Inter–observer reproducibility assessed by two observers for 10 randomly–selected datasets including Bland–Altman biases and 95% limits of agreement and the modified coefficient of variation (CoV) is shown in Table 6.3. Global circumferential and longitudinal strains demonstrated excellent reproducibility in both the right and left ventricles (CoV: 3–5%) (Figure 6.7). All global measures of LV and RV strain, torsion, and synchrony demonstrated excellent reproducibility with CoVs less than 15%. While slightly less reproducible, segmental strain, torsion, and dyssynchrony also demonstrated good inter–observer reproducibility with the exception of regional RV torsion (CoV = 44.4%). Inter–test reproducibility measured in 6 healthy individuals is shown in Table 6.4. Global measures of LV and RV strain, torsion, and dyssynchrony all demonstrated good inter–test reproducibility (all less than 20%) except for regional RV torsion (CoV = 28.0%).

6.4 Discussion

This study introduced a robust pipeline for processing 3D displacement–encoded images of both the left and right ventricles to yield measures of biventricular cardiac mechanics including global and regional strains, torsion, and dyssynchrony. By acquiring data in 50 healthy individuals, we were able to test the pipeline and characterize normal right ventricular function to serve as a baseline for future studies looking at impaired RV function. Our major findings included: 1) regional variations in circumferential and longitudinal strain were present within the RV, 2) global circumferential strain was comparable between the LV and RV while global longitudinal strain was larger in the RV, 3) the magnitude of RV torsion was similar to that observed in the LV, and 4) the RV contracts later but more synchronously than the LV.

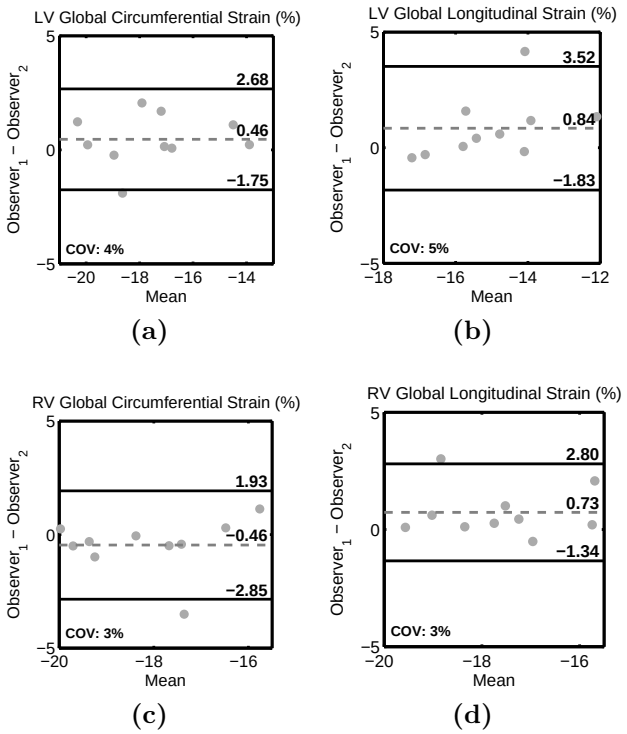

Figure 6.7: Bland-Altman analyisis of inter-observer reproducibility. Bland–Altman plots demonstrating inter–observer reproducibility for global circumferential (left) and longitudinal (right) strain in both the left (top) and right (bottom) ventricles.

Table 6.3: Inter–observer reproducibility

	Left Ventricle		Right Ventricle	
Global	Bland–Altman Bias ± Limits	CoV	Bland–Altman Bias ± Limits	CoV
Circum. Strain (%)	0.5 ± 2.2	3.6	-0.5 ± 2.4	3.1
Long. Strain (%)	0.8 ± 2.7	4.8	0.7 ± 2.1	3.3
Radial Strain (%)	1.3 ± 8.4	7.1	–	–
Torsion (°)	0.1 ± 0.8	2.5	-0.4 ± 3.0	14.8
[1]Dyssynchrony (%)	0.3 ± 1.6	5.6	-0.1 ± 2.2	9.8
Segmental				
Circum . Strain (%)	0.3 ± 3.6	5.7	-1.1 ± 6.2	9.8
Long. Strain (%)	0.6 ± 4.6	7.7	0.3 ± 6.9	10.3
Radial Strain (%)	-1.0 ± 17.6	12.0	–	–
Torsion (°)	0.1 ± 4.4	16.8	-0.5 ± 8.9	44.4
[1,2]Delay Times (%)	0.2 ± 4.0	–	0.2 ± 4.0	–

[1]Expressed as a percent of the cardiac cycle

[2]Negative is early contraction; Positive is late contraction

6.4.1 DENSE Post-Processing

Several components of the post-processing pipeline were developed to adapt the typical processing of the LV to the more complex geometry of the RV. While the LV is often modeled as a cylinder or prolate spheroid, neither is well-suited for the RV. The local coordinate system introduced in this study is a generalization of the cylindrical model that defined radial, circumferential, and longitudinal directions for any point on the LV and RV endocardial surfaces. This model definition allowed for the evaluation of RV mechanics analogous to LV mechanics, overcoming a limitation that was noted in the first study to compute RV mechanics from 3D DENSE imaging.[9] This generalization, while developed for the RV, also improves the post-processing of the LV, as the true LV geometry will never be a perfect cylinder or prolate spheroid.

Another benefit of the local coordinate system is its independence to the

Table 6.4: Inter–test reproducibility

	Left Ventricle		Right Ventricle	
Global	Bland–Altman Bias ± Limits	CoV	Bland–Altman Bias ± Limits	CoV
Circum. Strain (%)	0.7 ± 1.8	3.8	0.4 ± 1.5	2.8
Long. Strain (%)	0.0 ± l.3	2.4	-0.4 ± 3.1	4.8
Radial Strain (%)	0.6 ± 11.5	11.6	–	–
Torsion (°)	0.2 ± 1.2	5.6	0.6 ± 2.0	8.4
[1]Dyssynchrony (%)	0.4 ± 3.6	11.8	0.3 ± 2.2	10.8
Segmental				
Circum . Strain (%)	0.5 ± 4.0	6.6	0.8 ± 4.6	7.1
Long. Strain (%)	-0.1 ± 4.2	7.6	-0.3 ± 6.3	9.2
Radial Strain (%)	1.1 ± 21.3	18.0	–	–
Torsion (°)	0.2 ± 4.7	19.6	0.6 ± 8.2	28.0
[1,2]Delay Times (%)	-0.8 ± 5.9	–	0.4 ± 5.6	–

[1]Expressed as a percent of the cardiac cycle

[2]Negative is early contraction; Positive is late contraction

orientation of the images. When considering a short-axis image, it is common to define the radial and circumferential directions to be in the plane of the image while the longitudinal direction is perpendicular to the image.[29, 94] While this is possibly true for a cylindrical geometry and perfectly-oriented short-axis image planes, it is unlikely to be the case for the actual geometry of the RV and LV. By extracting the local coordinate system from endocardial surfaces that were fit to the boundaries of the myocardial segmentation, the resulting radial, circumferential, and longitudinal directions were not restricted based on the prescribed image planes. Indeed, any combination of image planes could be inputted to the pipeline as long as they span the extent of the ventricular anatomy including four-, three-, and two-chamber long-axis views.

Another important component of the pipeline is the circumferential and longitudinal parameterization of the RV, which enabled regional analyses. The AHA

17-segment model is widely used for the LV (including the septum) and is based on a cylindrical model with equiangular sampling around the LV central axis.[89] This model is not well suited for the irregular shape of the RV (i.e. the RV is not cylindrical and has no obvious central axis). By using normalized arc lengths and geodesic distances around the surface of the RV endocardial mesh, every point on the mesh was represented by a circumferential and longitudinal parameterization. A 13-segment RV model was chosen to represent regional strains in this study. There is no standard model for RV segmentation, and several different models have been proposed in previous studies.[78, 9, 95] Importantly, the parameterization employed in our post-processing pipeline is generalizable and can be made compatible with any such RV segmentation scheme.

6.4.2 Strain Analyses and Timing of Contraction

Globally, peak circumferential strains were similar between the RV and the LV. In the RV, peak circumferential strain was lowest in the basal outflow region (-16%). The remainder of the ventricle demonstrated higher circumferential strain values. This trend is consistent with previous imaging studies using myocardial tagging [96] and strain imaging (SENC).[97] Those two studies found the lowest principal strains and lowest circumferential strains in the basal region of the RV. An additional myocardial tagging study also found circumferential strain to be lowest in the outflow region (-16%).[98] A previous 3D DENSE study found that the inflow region demonstrated the lowest circumferential strain (-10%), however the outflow region was the next lowest segment (-15%).[9]

Peak global longitudinal strain was larger in the RV compared to that in the LV and displayed more regional heterogeneity than circumferential strain. Longitudinal strain was highest in the lateral regions, particularly in the apical segments, which also demonstrated the highest longitudinal strain across both ventricles. The lowest longitudinal strains were seen in the apical and mid-ventricular segments of the

outflow and inflow regions, however, the basal segments of those regions demonstrated higher strains. Both Hamdan *et al.* and Fayad *et al.* found the highest longitudinal strains in the apical (-19 and -29%, respectively) and basal (-19 and -25%, respectively) segments,[97, 98] which is consistent with our findings of the highest strains in the apical-lateral segments (-24%) and relatively high strains in the basal segments in the outflow and inflow regions (-19 and -20%, respectively). Auger *et al.* found the highest longitudinal strain in the basal outflow region (-22%), consistent with our findings; however, their lowest reported strain was in the basal inflow region (-16%) where we observed higher strains (-19%).[9] This discrepancy is likely due to differences in the strain computation and our use of a local coordinate system. Because Auger *et al.* did not define a local coordinate system for the RV, they resorted to separate 1-dimensional calculations in the direction that was perpendicular to the image planes.

Regarding both ventricles, the earliest contracting segments were in the septal and anterior regions of the LV while the latest segments were in the basal-lateral regions of the LV. Within the RV, the apical segments contracted earliest while the lateral wall contracted latest. We did not observe a gradient in contraction time from apex-to-base within the lateral regions. However, the basal segments of the outflow and inflow regions contracted later than their apical counterparts (difference in cross-correlation delay: 2% of cardiac cycle). Hamdan *et al.* found similar results to ours, with the apex contracting earliest and the base contracting latest (difference in time-to-peak: 55 ms),[97] which is consistent with the course of the right bundle branch that delivers electrical conduction down the septum to the apex and then out to the remainder of the ventricle.[99] In contrast, Auger *et al.* found the inflow region to contract earliest with the apex contracting latest (difference in time-to-peak: 96 ms). We also found the RV to contract more synchronously than the LV, which is likely due to the RV having a thinner wall and less myocardium, which takes less time to

depolarize and contract.

6.4.3 Right Ventricular Torsion

To our knowledge, this is the first study to quantify RV torsion, likely because it has been suspected that torsion does not play a large role in the RV compared to the LV .[100] A previous study has qualitatively observed reduced RV torsion in patients with RV hypertrophy, however, there were no attempts to quantify it.[101] While previous studies in the LV have used basal and apical twist relative to a central axis to quantify torsion, this procedure is not appropriate for the RV where there is no well-defined central axis.[102] The incorporation of a local coordinate system to define local circumferential and longitudinal directions allowed for the calculation of the local circumferential-longitudinal shear angle, which has been widely used as a measure of torsion in the LV.[102] We found the magnitude of RV torsion to be comparable between the RV and LV, largely due to segments in the lateral wall of the RV that had the largest shear angles across both ventricles. Regional RV torsion may be an important, and now quantifiable, indicator of RV function.

6.4.4 Reproducibility

Global circumferential and longitudinal strains demonstrated excellent inter-observer reproducibility with CoVs less than or equal to 5%. These compare well with previous inter-observer results for global LV strains (circumferential: 3.6%, longitudinal: 3.9%).[8] Global LV torsion demonstrated similarly excellent reproducibility, which agrees well with a previous study (CoV = 2.9%, [8]), while global RV torsion was less reproducible but still acceptable. As expected, regional mechanics were less reproducible than their global counterparts. This could be alleviated by dividing the ventricles into fewer segments and averaging the mechanics over a larger volume of tissue. Indeed, some segmentation models of the RV include only four segments (e.g. outflow, inflow, mid-ventricle, and apex).[9] RV

regional torsion was the least reproducible mechanic as measured by CoV (44%). This is likely due to the calculation of the circumferential-longitudinal shear angle, which is a combination of three components of the strain tensor, each with their own variability. In addition, there were many segments with nearly zero torsion such that a small variability leads to a high CoV. Regarding the timing of contraction, both the LV and RV dyssynchrony indices demonstrated good CoVs (6 and 10%, respectively), which is indicative of the good reproducibility of the regional delay times from which they were calculated.

6.4.5 Limitations

In this study, scan time for the 3D DENSE acquisition was 28 ± 6 minutes. This long scan time was partly due to the necessity of a respiratory navigator, which has imperfect efficiency, as well as the inherent duration of the scan. Unfortunately, this long scan duration is not clinically feasible, especially in patients with significant cardiac disease. There are several new developments in DENSE imaging including outer volume suppression,[72] parallel imaging and compressed sensing [74] which can ultimately be adapted to 3D acquisitions to reduce the scan duration by an order of magnitude.

All 3D DENSE data was obtained as a multi–slice acquisition rather than a volumetric acquisition to reduce acquisition time and allow for easy re-acquisition of images with poor image quality. This type of acquisition results in non-isotropic voxels which can potentially result in partial voluming and issues in quantifying strains particularly in the right ventricle where the geometry of the free wall is irregular. Future studies can use the proposed pipeline to better understand the effect of voxel size on the quantification of cardiac mechanics.

To perform interpolation of 3D displacements and compute strains, linear radial basis functions were used. Fitting an RBF to data, even when optimized, is a computationally expensive operation. This computational cost is offset by the fact

that linear RBFs extrapolate well and do not require post–processing such as spatial regularization which further influences the computed strains.

While this study sought to understand RV function in healthy individuals, no individuals with cardiac dysfunction were studied. Using this study as a reference, future studies can use the proposed framework to assess RV function in patients with heart disease.

6.5 Conclusion

The present study combined high–resolution displacement imaging from 3D spiral cine DENSE with a post–processing pipeline that included mesh–free strain analyses, a local coordinate system, and a flexible parameterization in order to quantify regional RV mechanics in 50 healthy individuals. Regional variations in circumferential and longitudinal strain were found throughout the RV while the RV lateral wall demonstrated torsion comparable to that observed in the LV. The RV was also found to contract more synchronously than the LV. Future studies can now investigate deviations from these healthy contraction patterns to potentially gain new insights into the manifestation and/or prognosis for a variety of diseases affecting the right ventricle.

CHAPTER 7

CONCLUSIONS

7.1 Summary

The overall goal of this project was to extend the spiral cine DENSE acquisition and image processing to be able to measure cardiac mechanics throughout the LV and RV. Five specific aims were completed to accomplish this goal.

7.1.1 Aim 1: Compare mechanics derived from spiral cine DENSE to those derived from standard clinical imaging

Background: Left ventricular (LV) mechanics provide a clinically relevant description of heart function. Feature tracking software is increasingly used to quantify mechanics from standard cine SSFP imaging, although validation against gold standard techniques (myocardial tagging or displacement encoding (DENSE)) has been limited. This study sought to compare LV mechanics from feature tracking to DENSE to determine whether feature tracking agreed well with DENSE, and thus, could be used in place of DENSE in future studies.

Methods: We reviewed our database to identify all instances where DENSE and steady state free precession (SSFP) imaging were performed at the same slice locations. Left ventricular strains and torsion were assessed with both feature tracking (TomTec) and DENSE. Agreement was assessed with Bland-Altman analyses and coefficients of variation (COV). Contour-based strains were derived from contours propagated by feature tracking and compared to feature tracking strains.

Results: We identified 88 participants with a total of 186 pairs of DENSE and SSFP images. Compared to DENSE, mid-ventricular circumferential strain from feature tracking had good agreement (bias: -0.4%, P = 0.36, COV: 10.9%). However,

feature tracking significantly overestimated the magnitude of circumferential strain at the base (bias: -4.0%, P ¡ 0.001, COV: 17.8%) and apex (bias: -2.4%, P = 0.01, COV: 14.8%), and significantly underestimated torsion (bias: -1.4 deg/cm, P ¡ 0.001, COV: 41.1%). Longitudinal strain had borderline acceptable agreement (bias: -0.2%, P = 0.77, COV: 19.3%). Contour-based strains had excellent agreement with featuring tracking (biases: -1.30.2%, COVs: 3.27.0%).

Conclusion: Circumferential strain from TomTec feature tracking approximated DENSE at the mid-ventricle, but over-estimated strain at the base and apex. Longitudinal strain demonstrated borderline acceptable agreement with DENSE. However, contour-based strain demonstrated excellent agreement with feature tracking, suggesting that feature tracking is not required to assess commonly measured strains. Finally, the agreement between DENSE and feature tracking for calculating torsion was poor. In general, mechanics estimated by feature tracking cannot be used in place of mechanics derived from DENSE.

7.1.2 Aim 2: Validate the accuracy of spiral cine DENSE at 3.0 T

Background: Displacement Encoding with Stimulated Echoes (DENSE) encodes displacement into the phase of the magnetic resonance signal. Due to the stimulated echo, the signal is inherently low and fades through the cardiac cycle. To compensate, a spiral acquisition has been used at 1.5T. This spiral sequence has not been validated at 3.0 T, where the increased signal would be valuable, but field inhomogeneities may result in measurement errors. We hypothesized that spiral cine DENSE is valid at 3.0 T and tested this hypothesis by measuring displacement errors at both 1.5 T and 3.0 T *in vivo*.

Methods: Two-dimensional spiral cine DENSE and tagged imaging of the left ventricle were performed on ten healthy participants at 3.0 T and six healthy participants at 1.5 T. Intersection points were identified on tagged images near end-systole. Displacements from the DENSE images were used to project those

points back to their origins. The deviation from a perfect grid was used as a measure of accuracy and quantified as root-mean-squared error. This measure was compared between 3.0 T and 1.5 T with the Wilcoxon rank sum test. Inter-observer variability of strains and torsion quantified by DENSE and agreement between DENSE and harmonic phase (HARP) were assessed by Bland-Altman analyses. The signal to noise ratio (SNR) at each cardiac phase was compared between 3.0 T and 1.5 T with the Wilcoxon rank sum test.

Results: The displacement accuracy of spiral cine DENSE was not different between 3.0 T and 1.5 T (1.2 ± 0.3 mm and 1.2 ± 0.4 mm, respectively). Both values were lower than the DENSE pixel spacing of 2.8 mm. There were no substantial differences in inter-observer variability of DENSE or agreement of DENSE and HARP between 3.0 T and 1.5 T. Relative to 1.5 T, the SNR at 3.0 T was greater by a factor of 1.4 ± 0.3.

Conclusions: The spiral cine DENSE acquisition that has been used at 1.5 T to measure cardiac displacements can be applied at 3.0 T with equivalent accuracy. The inter-observer variability and agreement of DENSE-derived peak strains and torsion with HARP is also comparable at both field strengths. Future studies with spiral cine DENSE may take advantage of the additional SNR at 3.0 T.

7.1.3 Aim 3: Determine the appropriate value for the spiral cine DENSE displacement encoding frequency

Background: Displacement Encoding with Stimulated Echoes (DENSE) encodes displacement into the phase of the magnetic resonance signal. The encoding frequency (k_e) maps the measured phase to tissue displacement while the strength of the encoding gradients affects image quality. 2D cine DENSE studies have used a k_e of 0.10 cycles/mm, which is high enough to remove an artifact-generating echo from k-space, provide high sensitivity to tissue displacements, and dephase the blood pool. However, through-plane dephasing can remove the unwanted echo and

dephase the blood pool without relying on high k_e. Additionally, the high sensitivity comes with the costs of increased phase wrapping and intra-voxel dephasing. We hypothesized that k_e below 0.10 cycles/mm can be used to improve image characteristics and provide accurate measures of cardiac mechanics.

Methods: Spiral cine DENSE images were obtained for 10 healthy participants and 10 patients with a history of heart disease on a 3.0 T Siemens Trio. A mid-ventricular short-axis image was acquired with different k_e: 0.02, 0.04, 0.06, 0.08, and 0.10 cycles/mm. Peak twist, circumferential strain, and radial strain were compared between acquisitions employing different k_e using Bland-Altman analyses and coefficients of variation. The percentage of wrapped pixels in the phase images at end-systole was calculated for each k_e. The dephasing of the blood signal and signal to noise ratio (SNR) were also calculated and compared.

Results: Negligible differences were seen in strains and twist for all k_e between 0.04 and 0.10 cycles/mm. These differences were of the same magnitude as inter-test differences. Specifically, the acquisitions with 0.04 cycles/mm accurately quantified cardiac mechanics and had zero phase wrapping. Compared to 0.10 cycles/mm, the acquisitions with 0.04 cycles/mm had 9% greater SNR and negligible differences in blood pool dephasing.

Conclusions: For 2D cine DENSE with through-plane dephasing, the encoding frequency can be lowered to 0.04 cycles/mm without compromising the quantification of twist or strain. The amount of wrapping can be reduced with this lower value to greatly simplify the input to unwrapping algorithms and allow 3D imaging of the RV.

7.1.4 Aim 4: Determine the effect of the number of spiral interleaves and the spiral readout duration on image quality and measured mechanics

Background: DENSE encodes tissue displacement into phase images, and spatial gradients within the phase images yield cardiac strains. With long readout durations, spiral acquisitions are prone to blurring that dampens image gradients.

The purpose of this study was to determine if image quality and measured cardiac strains are dependent on the readout duration of spiral cine displacement encoding with stimulated echoes (DENSE) at 3.0 T and 1.5 T.

Methods: Typical spiral cine DENSE acquisitions use 11.1 ms readouts. In addition to computational simulations, five healthy participants underwent 2D spiral cine DENSE at both 3.0 T and 1.5 T with several different readout durations including and below 11.1 ms.

Results: Simulations demonstrated that off-resonance and T2* decay, combined with a long readout duration, yield blurred images and underestimated strains. With the 11.1 ms readout, blurring was present in the anterior and lateral left ventricular walls of participants. Blurring was markedly reduced with shorter readout durations. Compared to the 1.9 ms readout, the 11.1 ms readout underestimated radial and circumferential strains in those cardiac segments at both field strengths by up to 19.6% and 1.5% (absolute), respectively.

Conclusion: Image quality and measured cardiac strains are dependent on the readout duration of spiral cine DENSE at both 3.0 T and 1.5 T. Using more interleaves during spiral cine DENSE imaging allows for a shorter readout duration which produces less blurring and more accurate strain measurements.

7.1.5 Aim 5: Develop and evaluate a single post-processing pipeline to quantify mechanics from both the LV and RV

Background: Mechanics of the left ventricle (LV) are important indicators of cardiac function. The role of right ventricular (RV) mechanics is largely unknown due to the technical limitations of imaging its thin wall and complex geometry and motion. Imaging at 3.0 T with a lower encoding frequency and an increased number of spiral interleaves now facilitates 3D DENSE of the RV. By combining 3D DENSE with a post-processing pipeline that includes a local coordinate system, it may be possible to quantify RV strain, torsion, and synchrony to assess normal RV mechanics for the

first time.

Methods: In this study, we sought to characterize RV mechanics in 50 healthy individuals and compare these values to their LV counterparts. For each cardiac frame, 3D displacements were fit to continuous and differentiable radial basis functions, allowing for the computation of the 3D Cartesian Lagrangian strain tensor at any myocardial point. The geometry of the RV was extracted via a surface fit to manually delineated endocardial contours. Throughout the RV, a local coordinate system was used to transform from a Cartesian strain tensor to a polar strain tensor. It was then possible to compute peak RV torsion as well as peak longitudinal and circumferential strain. A comparable analysis was performed for the LV. Dyssynchrony was computed from the standard deviation of regional activation times.

Results: Global circumferential strain was comparable between the RV and LV (-18.0% for both) while longitudinal strain was greater in the RV (-18.1% vs. -15.7%). RV torsion was comparable to LV torsion (6.2 vs. 7.1 degrees, respectively). Regional activation times indicated that the RV contracted later but more synchronously than the LV.

Conclusion: 3D spiral cine DENSE combined with a post–processing pipeline that includes a local coordinate system can resolve both the complex geometry and 3D motion of the RV. 3D cardiac mechanics can now be quantified throughout the LV and RV using spiral cine DENSE.

7.2 Implications

Cardiac mechanics can now be quantified throughout the left and right ventricles using spiral cine DENSE cardiac MRI. The availability of these sensitive measures of cardiac function may provide new insight into the dysfunction and sub-clinical progression of many cardiac conditions (*e.g.* ARVC, RV hypertrophy, pulmonary hypertension, congenital heart disease, *etc.*). In addition, given the

previously-demonstrated prognostic value of globally-averaged mechanics, like global longitudinal strain, knowledge of region-specific mechanics throughout both ventricles may further extend the predictive power of cardiac mechanics.

7.3 Future Directions

7.3.1 Accelerating Spiral Cine DENSE

One of the biggest limitations of spiral cine DENSE is the total scan time that is necessary to acquire the image data. In our study of RV mechanics from 3D DENSE, the average scan time was 28 minutes.[103] This long scan time limits clinical feasibility. Fortunately, multiple techniques that can reduce MRI scan times may be applicable to spiral cine DENSE.

One of the drivers of long total scan times is the desire to reduce the readout duration to prevent blurring and distortions. The simplest way to reduce the readout duration is to increase the number of acquired spiral interleaves. However, the total scan time increases with the number of interleaves such that there is a practical limit to how many interleaves can be acquired. Off-resonance is a substantial cause of blurring with long readout durations, and simple corrections for off-resonance are currently built into the spiral cine DENSE acquisition. However, more advanced correction algorithms exist and their implementation may allow for longer readout durations without the penalty of blurring and distortions.[68, 69, 70, 71] A future study could evaluate those algorithms to determine whether they would permit an increase in the readout duration, and thus a decrease in the required number of spiral interleaves and total scan time.

Three other techniques exist to decrease the total scan time by reducing the amount of data that must be acquired in order for the MRI to reconstruct a high quality image. Briefly, the MRI scanner reconstructs an image by first acquiring the frequency space (commonly known as k-space) of the desired image, and then

performing an inverse Fourier Transform on that acquired data, which yields the image. The total scan time is governed by how long it takes to acquire the entirety of the k-space. Importantly, these three techniques may be applied simultaneously to achieve substantial reductions in scan time.

1. Zonal excitation, or outer volume suppression, is an acquisition technique where the magnetic field gradients and radiofrequency pulses are manipulated in order to "black-out" or null the outer regions of the image. This works well for cardiac MRI, where the object of interest, the heart, is located at the center of the image. Zonal excitation effectively reduces the field of view, which then reduces the amount of k-space data that must be acquired. Zonal excitation has been introduced into 2D spiral cine DENSE and it could be extended to 3D spiral cine DENSE.[72]

2. Parallel imaging requires multiple coil elements distributed spatially around the region of interest. Fortunately, it is very common to have multiple coil elements (*e.g.* we often used 6-element chest coils). Individually, each element has a sensitivity profile such that it has a high signal to noise ratio near the element and very low or zero signal to noise ratio for regions of the image that are distant from the element. Using multiple elements provides for high signal to noise ratio throughout the image, which is the primary motivation. However, because they have different regional sensitivities, it is possible to use that information during the image reconstruction instead of relying on a fully-sampled k-space. Several algorithms such as SENSE,[104] GRAPPA,[105] and SPIRiT[106] have been created to exploit this extra information and reduce the total scan time by reducing the amount of k-space that needs to be acquired. Parallel imaging has been introduced into 2D spiral cine DENSE.[74]

3. Compressed sensing relies on a type of regularity known as sparsity that is

common among natural images including medical images.[107] Medical images are far from random collections of pixels. Rather, the images have regular patterns and structures. Some medical images, such as angiograms, are often sparse – meaning that most of the pixels are black, while there are only a few bright pixels that represent blood vessels. Other types of images, like cardiac MRI, are be sparse in certain transform domains. By making the appropriate assumption that a reconstructed MRI image should be sparse in a least some domain, it is possible to reconstruct an image without completely sampling the k-space data. Compressed sensing, in combination with parallel imaging, has been introduced to 2D spiral cine DENSE and may be adaptable to 3D acquisitions.[74]

Lastly, a significant limitation of spiral cine DENSE, and cardiac MRI in general, is the effect of respiratory motion. The act of breathing during image acquisition results in blurred cardiac images. For this reason, it is common to perform cardiac MRI during breath-holds where respiratory motion is suspended. Many standard, clinical cardiac MRI techniques can be performed within approximately 10-second breath-holds, which are feasible for most patients. However, like other advanced techniques, 3D spiral cine DENSE requires a much longer scan time that cannot be done within a typical breath-hold. As an alternative to breath-hold imaging, respiratory gating can be performed whereby the MRI scanner takes a picture of the patient's diaphragm at nearly the same instant that it is acquiring the cardiac image data. By monitoring the position of the diaphragm to track respiratory motion, the MRI computer can choose to collect cardiac image data only when the diaphragm is at a preset location. In this manner, the acquired data is substantially less corrupted by respiratory motion even if the scan time was several minutes and the patient was able to breathe normally during that time. Unfortunately, this technique results in a large amount of "wasted" scan time, since the scanner could not collect image data

while the patient was taking breaths. An advanced alternative, known as motion compensation, removes this penalty by always collecting cardiac imaging data, and then correcting that data for respiratory motion. Motion compensation has been incorporated into 2D spiral cine DENSE with some success.[108] The adaptation to 3D spiral cine DENSE is ongoing.

7.3.2 Predicting outcomes

The primary role of physicians is to make predictions about patients' outcomes and then make therapeutic decisions that offer the best probability of positive outcomes. To do this, physicians rely on the clinical data obtained from a patient and previous research or past clinical experience that suggests what that data means for the likelihood of outcomes. Thus, the clinical value of any measurement, whether it is commonly-performed measurements like ejection fraction or the newly available measures of LV and RV mechanics, should be based largely on how well it is associated with outcomes. Measurements or data that are not associated with outcomes are not useful for guiding clinical decisions.

Ultimately, it will be necessary to assess how well cardiac mechanics throughout the LV and RV relate to patient outcomes and compare the strength of that relationship to that of other measurements of cardiac function, such as ejection fraction. Because the ability to measure mechanics throughout the LV and RV is new, there is very little outcome data available. Future endeavors will attempt to build such datasets for specific patient populations. In addition, it may be possible to use a relatively small training dataset consisting of both spiral cine DENSE and standard clinical imaging in order to teach a computer to extract accurate measures of cardiac mechanics from the standard clinical imaging via machine learning algorithms. This would unlock the ability to measure cardiac mechanics from historical datasets where standard clinical imaging was acquired and the patient outcomes are known.

While the availability of datasets of cardiac mechanics throughout the LV and RV is currently too small to relate to outcomes, we have been able to assess how well current clinical measures relate to outcomes. Specifically, we have investigated the independent relationship between left ventricular ejection fraction and all-cause mortality within the Geisinger Health System. The results below provide the necessary reference of how well our current measurements relate to outcomes, which can then be compared to the relationship between cardiac mechanics and outcomes once that dataset is available.

Redefining Normal Left Ventricular Systolic Function Based on Outcomes Using Nearly 20 Years of Data from a Large Regional Health System

Background: Despite the widespread use of left ventricular ejection fraction (LVEF), no study has answered the fundamental question: *What is a normal LVEF?* Guidelines define an LVEF of 53-73% as normal based on surveys of healthy subjects, rather than on associations with outcomes. Studies that have linked LVEF to outcomes have used small sample sizes or dichotomized LVEF into reduced and preserved, which precludes their ability to define normal. We hypothesized that defining a normal LVEF based on association with all-cause mortality would lead to a new understanding of normal systolic function.

Methods: 146,706 patients with a total of 283,483 echocardiograms with physician-dictated LVEF were identified in the Geisinger electronic health record (1998-2016) along with dates of death or last living encounter, age, sex, height, weight, and active diagnoses. Change in LVEF (ΔLVEF) was measured from consecutive echocardiograms when possible. Cox Proportional Hazards Regression was used to relate LVEF to all-cause mortality while adjusting for confounders.

Results: 71,054 (25%) of the echocardiograms were associated with death in 31,492 patients. Median follow up duration was 3.7 years (IQR, 1.2-7.7). The

adjusted LVEF hazard ratios (HR) showed a u-shaped distribution with a minimum at 60-65% and all higher and lower LVEF intervals showing significantly higher HRs (Figure 7.1A). Relative to the 60-65% interval, LVEF$\geq$70% had a HR of 1.81 (95% CI, 1.73-1.90), which was similar to the HR for a reduced LVEF of 35-40% (1.83). The results were similar after additional adjustments for entities known to pathologically elevate LVEF such as mitral regurgitation, wall thickness, and anemia. In the 136,776 echocardiograms for which ΔLVEF was known, both increases and decreases in LVEF had significantly higher HRs than the minimal change interval. For LVEF<22.5% (decreasing) the HR was 1.46 (95% CI, 1.35-1.58). For LVEF>22.5% (increasing) the HR was 1.19 (95% CI 1.09-1.29).

Conclusions: Contrary to guidelines, this study shows that normal systolic function is limited to a stable LVEF of 60-65%. In an echocardiography laboratory that defines LVEF>50% as normal, 56% of all echocardiograms would be falsely interpreted as having a normal LVEF. Moreover, high LVEF may be equally important as low LVEF for predicting mortality.

7.4 Final Thoughts

In summary, after overcoming technical limitations of signal to noise ratio, phase wrapping, spatial resolution, blurring, and the complex shape of the right ventricle, cardiac mechanics can now be quantified throughout the both ventricles using spiral cine DENSE cardiac MRI. The availability of these sensitive measures of cardiac function may provide new insight into the dysfunction and sub-clinical progression of many cardiac conditions (*e.g.* ARVC). Furthermore, measures of mechanics throughout the LV and RV may relate strongly to patient outcomes. Since the primary role of physicians is to predict patients' outcomes and guide therapy based on those predictions, the measurement of cardiac mechanics may eventually become indispensable for optimal management.

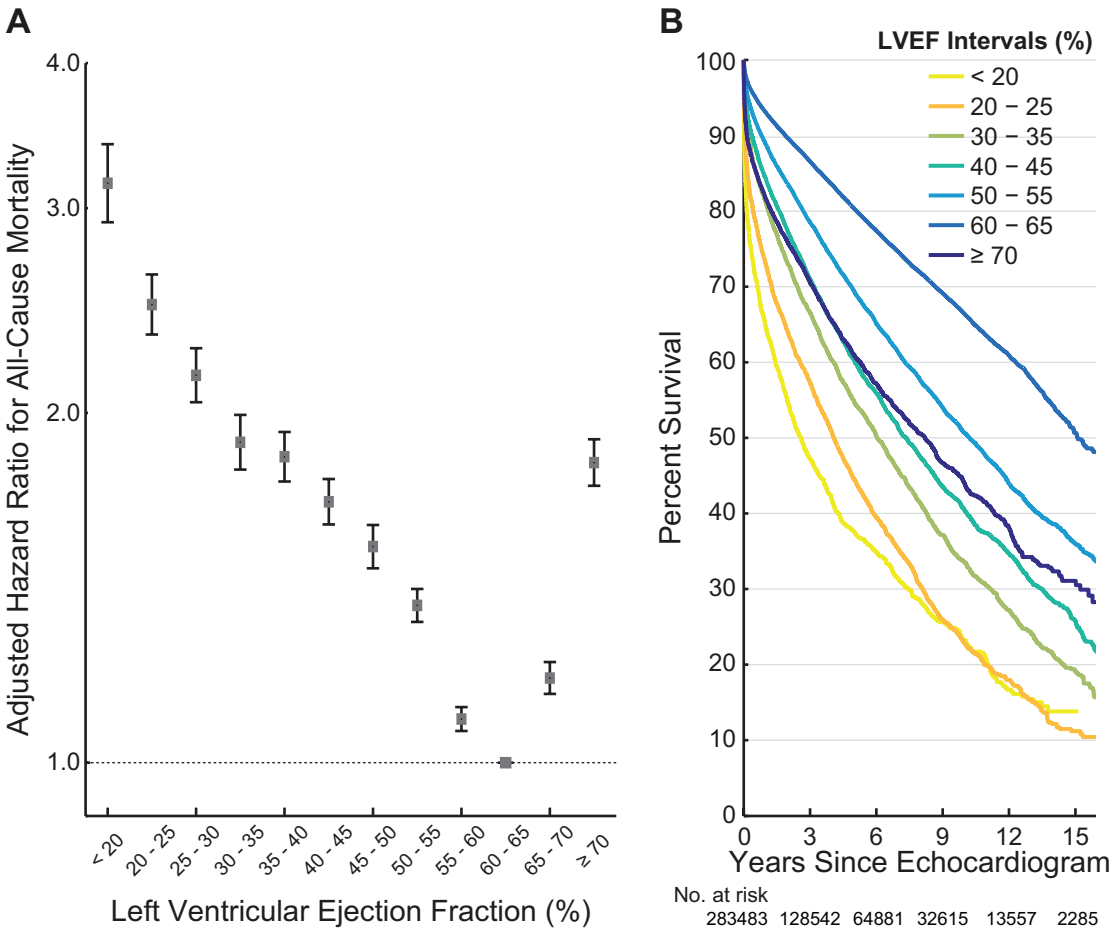

Figure 7.1: Adjusted hazard ratios and Kaplan-Meier survival curves by LVEF. (**A**)Adjusted hazard ratios showed a u-shaped distribution with a minimum at an LVEF of 60-65% Error bars represent 95% confidence intervals. (**B**) Unadjusted survival curves demonstrate the ability of LVEF to stratify survival. Selected curves are shown for clarity. LVEF intervals are inclusive of the lower endpoint.

Bibliography

[1] Solomon SD, Anavekar N, Skali H, McMurray JJV, Swedberg K, Yusuf S, Granger CB, Michelson EL, Wang D, Pocock S, and Pfeffer MA. "Influence of ejection fraction on cardiovascular outcomes in a broad spectrum of heart failure patients." *Circulation*, 2005. **112**(24):3738–3744. ISSN 00097322. doi: 10.1161/CIRCULATIONAHA.105.561423.

[2] Axel L and Dougherty L. "MR imaging of motion with spatial modulation of magnetization." *Radiology*, 1989. **171**(3):841–845. doi:10.1148/radiology.171.3.2717762.

[3] Kalam K, Otahal P, and Marwick TH. "Prognostic implications of global LV dysfunction: a systematic review and meta-analysis of global longitudinal strain and ejection fraction." *Heart (British Cardiac Society)*, 2014. **100**(21):1673–80. ISSN 1468-201X. doi:10.1136/heartjnl-2014-305538.

[4] Stanton T, Leano R, and Marwick TH. "Prediction of all-cause mortality from global longitudinal speckle strain: comparison with ejection fraction and wall motion scoring." *Circ Cardiovasc Imaging*, 2009. **2**(5):356–364. doi:10.1161/CIRCIMAGING.109.862334.

[5] Aletras AH, Ding S, Balaban RS, and Wen H. "DENSE: displacement encoding with stimulated echoes in cardiac functional MRI." *J Magn Reson*, 1999. **137**(1):247–252. doi:10.1006/jmre.1998.1676.

[6] Zhong X, Spottiswoode BS, Meyer CH, Kramer CM, and Epstein FH. "Imaging three-dimensional myocardial mechanics using navigator-gated volumetric spiral cine DENSE MRI." *Magn Reson Med*, 2010. **64**(4):1089–1097. doi: 10.1002/mrm.22503.

[7] Young AA, Li B, Kirton RS, and Cowan BR. "Generalized spatiotemporal myocardial strain analysis for DENSE and SPAMM imaging." *Magn Reson Med*, 2012. **67**(6):1590–1599. doi:10.1002/mrm.23142.

[8] Wehner GJ, Suever JD, Haggerty CM, Jing L, Powell DK, Hamlet SM, Grabau JD, Mojsejenko WD, Zhong X, Epstein FH, and Fornwalt BK. "Validation of in vivo 2D displacements from spiral cine DENSE at 3T." *Journal of cardiovascular magnetic resonance*, 2015. **17**(1):5. ISSN 1532-429X. doi: 10.1186/s12968-015-0119-z.

[9] Auger DA, Zhong X, Epstein FH, and Spottiswoode BS. "Mapping right ventricular myocardial mechanics using 3D cine DENSE cardiovascular magnetic resonance." *Journal of cardiovascular magnetic resonance : official journal of the Society for Cardiovascular Magnetic Resonance*, 2012. **14**:4. ISSN 1532-429X. doi:10.1186/1532-429X-14-4.

[10] Zhong X, Gibberman LB, Spottiswoode BS, Gilliam AD, Meyer CH, French BA, and Epstein FH. "Comprehensive cardiovascular magnetic resonance

of myocardial mechanics in mice using three-dimensional cine DENSE." *J Cardiovasc Magn Reson*, 2011. **13**:83. doi:10.1186/1532-429X-13-83.

[11] Choi EY, Rosen BD, Fernandes VR, Yan RT, Yoneyama K, Donekal S, Opdahl A, Almeida AL, Wu CO, Gomes AS, Bluemke DA, and Lima JA. "Prognostic value of myocardial circumferential strain for incident heart failure and cardiovascular events in asymptomatic individuals: the Multi-Ethnic Study of Atherosclerosis." *Eur Heart J*, 2013. **34**(30):2354–2361. doi: 10.1093/eurheartj/eht133.

[12] Ibrahim el SH. "Myocardial tagging by cardiovascular magnetic resonance: evolution of techniques–pulse sequences, analysis algorithms, and applications." *J Cardiovasc Magn Reson*, 2011. **13**:36. doi:10.1186/1532-429X-13-36.

[13] Kim D, Gilson WD, Kramer CM, and Epstein FH. "Myocardial tissue tracking with two-dimensional cine displacement-encoded MR imaging: development and initial evaluation." *Radiology*, 2004. **230**(3):862–871. doi:10.1148/radiol. 2303021213.

[14] Osman NF, Sampath S, Atalar E, and Prince JL. "Imaging longitudinal cardiac strain on short-axis images using strain-encoded MRI." *Magn Reson Med*, 2001. **46**(2):324–334.

[15] Simpson R, Keegan J, and Firmin D. "Efficient and reproducible high resolution spiral myocardial phase velocity mapping of the entire cardiac cycle." *J Cardiovasc Magn Reson*, 2013. **15**(1):34. doi:10.1186/1532-429X-15-34.

[16] Hor KN, Gottliebson WM, Carson C, Wash E, Cnota J, Fleck R, Wansapura J, Klimeczek P, Al-Khalidi HR, Chung ES, Benson DW, and Mazur W. "Comparison of magnetic resonance feature tracking for strain calculation with harmonic phase imaging analysis." *JACC Cardiovasc Imaging*, 2010. **3**(2):144–151. doi:10.1016/j.jcmg.2009.11.006.

[17] Claus P, Omar AMS, Pedrizzetti G, Sengupta PP, and Nagel E. "Tissue Tracking Technology for Assessing Cardiac MechanicsPrinciples, Normal Values, and Clinical Applications." *JACC: Cardiovascular Imaging*, 2015. **8**(12):1444–1460. ISSN 1936-878X. doi:10.1016/j.jcmg.2015.11.001.

[18] Morton G, Schuster A, Jogiya R, Kutty S, Beerbaum P, and Nagel E. "Inter-study reproducibility of cardiovascular magnetic resonance myocardial feature tracking." *Journal of cardiovascular magnetic resonance : official journal of the Society for Cardiovascular Magnetic Resonance*, 2012. **14**:43. ISSN 1532-429X (Electronic). doi:10.1186/1532-429X-14-43.

[19] Augustine D, Lewandowski AJ, Lazdam M, Rai A, Francis J, Myerson S, Noble A, Becher H, Neubauer S, Petersen SE, and Leeson P. "Global and regional left ventricular myocardial deformation measures by magnetic resonance feature tracking in healthy volunteers: comparison with tagging and relevance of

gender." *Journal of cardiovascular magnetic resonance : official journal of the Society for Cardiovascular Magnetic Resonance*, 2013. **15**:8. ISSN 1532-429X (Electronic). doi:10.1186/1532-429X-15-8.

[20] Harrild DM, Han Y, Geva T, Zhou J, Marcus E, and Powell AJ. "Comparison of cardiac MRI tissue tracking and myocardial tagging for assessment of regional ventricular strain." *International Journal of Cardiovascular Imaging*, 2012. **28**(8):2009–2018. ISSN 15695794. doi:10.1007/s10554-012-0035-3.

[21] Kuetting D, Sprinkart AM, Doerner J, Schild H, and Thomas D. "Comparison of magnetic resonance feature tracking with harmonic phase imaging analysis (CSPAMM) for assessment of global and regional diastolic function." *European journal of radiology*, 2015. **84**(1):100–107. ISSN 1872-7727 (Electronic). doi: 10.1016/j.ejrad.2014.10.011.

[22] Singh A, Steadman CD, Khan JN, Horsfield MA, Bekele S, Nazir SA, Kanagala P, Masca NGD, Clarysse P, and McCann GP. "Intertechnique agreement and interstudy reproducibility of strain and diastolic strain rate at 1.5 and 3 Tesla: a comparison of feature-tracking and tagging in patients with aortic stenosis." *Journal of magnetic resonance imaging : JMRI*, 2015. **41**(4):1129–1137. ISSN 1522-2586 (Electronic). doi:10.1002/jmri.24625.

[23] Kuetting DLR, Sprinkart AM, Dabir D, Schild HH, and Thomas DK. "Assessment of cardiac dyssynchrony by cardiac MR: A comparison of velocity encoding and feature tracking analysis." *Journal of magnetic resonance imaging : JMRI*, 2015. ISSN 1522-2586 (Electronic). doi:10.1002/jmri.25062.

[24] Kempny A, Fernández-Jiménez R, Orwat S, Schuler P, Bunck AC, Maintz D, Baumgartner H, Diller GP, Fernandez-Jimenez R, Orwat S, Schuler P, Bunck AC, Maintz D, Baumgartner H, and Diller GP. "Quantification of biventricular myocardial function using cardiac magnetic resonance feature tracking, endocardial border delineation and echocardiographic speckle tracking in patients with repaired tetralogy of Fallot and healthy controls." *Journal of cardiovascular magnetic resonance : official journal of the Society for Cardiovascular Magnetic Resonance*, 2012. **14**:32. ISSN 1532-429X. doi: 10.1186/1532-429X-14-32.

[25] Zhong X, Helm PA, and Epstein FH. "Balanced multipoint displacement encoding for DENSE MRI." *Magn Reson Med*, 2009. **61**(4):981–988. doi: 10.1002/mrm.21851.

[26] Wehner GJ, Grabau JD, Suever JD, Haggerty CM, Jing L, Powell DK, Hamlet SM, Vandsburger MH, Zhong X, and Fornwalt BK. "2D cine DENSE with low encoding frequencies accurately quantifies cardiac mechanics with improved image characteristics." *Journal of Cardiovascular Magnetic Resonance*, 2015. **17**(1):93. ISSN 1532-429X. doi:10.1186/s12968-015-0196-z.

[27] Zhong X, Spottiswoode BS, Cowart EA, Gilson WD, and Epstein FH. "Selective suppression of artifact-generating echoes in cine DENSE using through-plane dephasing." *Magn Reson Med*, 2006. **56**(5):1126–1131. doi:10.1002/mrm.21058.

[28] Gilliam AD and Suever JD. "DENSEanalysis.", 2016.

[29] Spottiswoode BS, Zhong X, Hess AT, Kramer CM, Meintjes EM, Mayosi BM, and Epstein FH. "Tracking myocardial motion from cine DENSE images using spatiotemporal phase unwrapping and temporal fitting." *IEEE Trans Med Imaging*, 2007. **26**(1):15–30. doi:10.1109/TMI.2006.884215.

[30] Wu L, Germans T, Güçlü A, Heymans MW, Allaart CP, and van Rossum AC. "Feature tracking compared with tissue tagging measurements of segmental strain by cardiovascular magnetic resonance." *Journal of cardiovascular magnetic resonance : official journal of the Society for Cardiovascular Magnetic Resonance*, 2014. **16**(1):10. ISSN 1532-429X. doi:10.1186/1532-429X-16-10.

[31] Moody WE, Taylor RJ, Edwards NC, Chue CD, Umar F, Taylor TJ, Ferro CJ, Young AA, Townend JN, Leyva F, and Steeds RP. "Comparison of magnetic resonance feature tracking for systolic and diastolic strain and strain rate calculation with spatial modulation of magnetization imaging analysis." *Journal of magnetic resonance imaging : JMRI*, 2015. **41**(4):1000–1012. ISSN 1522-2586 (Electronic). doi:10.1002/jmri.24623.

[32] Voigt JU, Pedrizzetti G, Lysyansky P, Marwick TH, Houle H, Baumann R, Pedri S, Ito Y, Abe Y, Metz S, Song JH, Hamilton J, Sengupta PP, Kolias TJ, D'Hooge J, Aurigemma GP, Thomas JD, and Badano LP. "Definitions for a Common Standard for 2D Speckle Tracking Echocardiography: Consensus Document of the EACVI/ASE/Industry Task Force to Standardize Deformation Imaging." *Journal of the American Society of Echocardiography*, 2015. **28**(2):183–193. ISSN 08947317. doi:10.1016/j.echo.2014.11.003.

[33] Moore CC, Lugo-Olivieri CH, McVeigh ER, and Zerhouni EA. "Three-dimensional systolic strain patterns in the normal human left ventricle: characterization with tagged MR imaging." *Radiology*, 2000. **214**(2):453–466. doi:10.1148/radiology.214.2.r00fe17453.

[34] Haggerty CM, Kramer SP, Binkley CM, Powell DK, Mattingly AC, Charnigo R, Epstein FH, and Fornwalt BK. "Reproducibility of cine displacement encoding with stimulated echoes (DENSE) cardiovascular magnetic resonance for measuring left ventricular strains, torsion, and synchrony in mice." *J Cardiovasc Magn Reson*, 2013. **15**:71. doi:10.1186/1532-429X-15-71.

[35] Kowallick JT, Morton G, Lamata P, Jogiya R, Kutty S, Lotz J, Hasenfuß G, Nagel E, Chiribiri A, and Schuster A. "Inter-study reproducibility of left ventricular torsion and torsion rate quantification using MR myocardial feature tracking." *Journal of Magnetic Resonance Imaging*, 2016. **43**(1):128–137. ISSN 15222586. doi:10.1002/jmri.24979.

[36] Feng L, Donnino R, Babb J, Axel L, and Kim D. "Numerical and in vivo validation of fast cine displacement-encoded with stimulated echoes (DENSE) MRI for quantification of regional cardiac function." *Magnetic resonance in medicine*, 2009. **62**(3):682–90. ISSN 1522-2594. doi:10.1002/mrm.22045.

[37] Leitman M, Lysiansky M, Lysyansky P, Friedman Z, Tyomkin V, Fuchs T, Adam D, Krakover R, and Vered Z. "Circumferential and Longitudinal Strain in 3 Myocardial Layers in Normal Subjects and in Patients with Regional Left Ventricular Dysfunction." *Journal of the American Society of Echocardiography*, 2010. **23**(1):64–70. ISSN 08947317. doi:10.1016/j.echo.2009.10.004.

[38] Donekal S, Ambale-Venkatesh B, Berkowitz S, Wu CO, Choi EY, Fernandes V, Yan R, Harouni Aa, Bluemke Da, and Lima Ja. "Inter-study reproducibility of cardiovascular magnetic resonance tagging." *Journal of cardiovascular magnetic resonance : official journal of the Society for Cardiovascular Magnetic Resonance*, 2013. **15**(1):37. ISSN 1532-429X. doi:10.1186/1532-429X-15-37.

[39] Jing L, Haggerty CM, Suever JD, Alhadad S, Prakash A, Cecchin F, Skrinjar O, Geva T, Powell AJ, and Fornwalt BK. "Patients with repaired tetralogy of Fallot suffer from intra- and inter-ventricular cardiac dyssynchrony: a cardiac magnetic resonance study." *European heart journal cardiovascular Imaging*, 2014. **15**(12):1333–43. ISSN 2047-2412. doi:10.1093/ehjci/jeu123.

[40] Andre F, Steen H, Matheis P, Westkott M, Breuninger K, Sander Y, Kammerer R, Galuschky C, Giannitsis E, Korosoglou G, Katus HA, and Buss SJ. "Age- and gender-related normal left ventricular deformation assessed by cardiovascular magnetic resonance feature tracking." *Journal of cardiovascular magnetic resonance : official journal of the Society for Cardiovascular Magnetic Resonance*, 2015. **17**:25. ISSN 1532-429X (Electronic). doi:10.1186/s12968-015-0123-3.

[41] de Siqueira MEM, Pozo E, Fernandes VR, Sengupta PP, Modesto K, Gupta SS, Barbeito-Caamaño C, Narula J, Fuster V, Caixeta A, and Sanz J. "Characterization and clinical significance of right ventricular mechanics in pulmonary hypertension evaluated with cardiovascular magnetic resonance feature tracking." *Journal of Cardiovascular Magnetic Resonance*, 2016. **18**(1):39. ISSN 1532-429X. doi:10.1186/s12968-016-0258-x.

[42] Jing L, Binkley CM, Suever JD, Umasankar N, Haggerty CM, Rich J, Nevius CD, Wehner GJ, Hamlet SM, Powell DK, Radulescu A, Kirchner HL, Epstein FH, and Fornwalt BK. "Cardiac remodeling and dysfunction in childhood obesity: a cardiovascular magnetic resonance study." *Journal of Cardiovascular Magnetic Resonance*, 2016. **18**(1):28. ISSN 1532-429X. doi:10.1186/s12968-016-0247-0.

[43] Schuster A, Stahnke VC, Unterberg-Buchwald C, Kowallick JT, Lamata P, Steinmetz M, Kutty S, Fasshauer M, Staab W, Sohns JM, Bigalke B,

Ritter C, Hasenfuß G, Beerbaum P, and Lotz J. "Cardiovascular magnetic resonance feature-tracking assessment of myocardial mechanics: Intervendor agreement and considerations regarding reproducibility." *Clinical Radiology*, 2015. **70**(9):989–998. ISSN 1365229X. doi:10.1016/j.crad.2015.05.006.

[44] Aletras AH, Balaban RS, and Wen H. "High-resolution strain analysis of the human heart with fast-DENSE." *J Magn Reson*, 1999. **140**(1):41–57. doi:10.1006/jmre.1999.1821.

[45] Budge LP, Helms AS, Salerno M, Kramer CM, Epstein FH, and Bilchick KC. "MR cine DENSE dyssynchrony parameters for the evaluation of heart failure: comparison with myocardial tissue tagging." *JACC Cardiovasc Imaging*, 2012. **5**(8):789–797. doi:10.1016/j.jcmg.2011.12.024.

[46] Kim D, Epstein FH, Gilson WD, and Axel L. "Increasing the signal-to-noise ratio in DENSE MRI by combining displacement-encoded echoes." *Magnetic resonance in medicine*, 2004. **52**(1):188–92. ISSN 0740-3194. doi:10.1002/mrm.20109.

[47] Bilchick KC, Kuruvilla S, Hamirani YS, Ramachandran R, Clarke SA, Parker KM, Stukenborg GJ, Mason P, Ferguson JD, Moorman JR, Malhotra R, Mangrum JM, Darby AE, Dimarco J, Holmes JW, Salerno M, Kramer CM, and Epstein FH. "Impact of mechanical activation, scar, and electrical timing on cardiac resynchronization therapy response and clinical outcomes." *J Am Coll Cardiol*, 2014. **63**(16):1657–1666. doi:10.1016/j.jacc.2014.02.533.

[48] Stuber M, Spiegel MA, Fischer SE, Scheidegger MB, Danias PG, Pedersen EM, and Boesiger P. "Single breath-hold slice-following CSPAMM myocardial tagging." *MAGMA*, 1999. **9**(1-2):85–91.

[49] Sigfridsson A, Haraldsson H, Ebbers T, Knutsson H, and Sakuma H. "In vivo SNR in DENSE MRI; temporal and regional effects of field strength, receiver coil sensitivity and flip angle strategies." *Magn Reson Imaging*, 2011. **29**(2):202–208. doi:10.1016/j.mri.2010.08.016.

[50] Zhong X, Spottiswoode BS, Meyer CH, and Epstein FH. "Two-dimensional Spiral Cine DENSE." In "Proceedings of the International Society for Magnetic Resonance in Medicine," volume 7. Berlin, 2007 756.

[51] Arun KS, Huang TS, and Blostein SD. "Least-Squares Fitting of Two 3-D Point Sets." *IEEE Transactions on Pattern Analysis and Machine Intelligence*, 1987. **PAMI-9**(5):698–700. ISSN 0162-8828. doi:10.1109/TPAMI.1987.4767965.

[52] Bland JM and Altman DG. "Statistical methods for assessing agreement between two methods of clinical measurement." *Lancet*, 1986. **1**(8476):307–310.

[53] Gudbjartsson H and Patz S. "The Rician distribution of noisy MRI data." *Magn Reson Med*, 1995. **34**(6):910–914.

[54] Piechnik SK, Ferreira VM, Dall'Armellina E, Cochlin LE, Greiser A, Neubauer S, and Robson MD. "Shortened Modified Look-Locker Inversion recovery (ShMOLLI) for clinical myocardial T1-mapping at 1.5 and 3 T within a 9 heartbeat breathhold." *Journal of cardiovascular magnetic resonance : official journal of the Society for Cardiovascular Magnetic Resonance*, 2010. **12**(1):69. ISSN 1532-429X. doi:10.1186/1532-429X-12-69.

[55] Li W and Yu X. "Quantification of myocardial strain at early systole in mouse heart: restoration of undeformed tagging grid with single-point HARP." *Journal of magnetic resonance imaging : JMRI*, 2010. **32**(3):608–14. ISSN 1522-2586. doi:10.1002/jmri.22256.

[56] Bilchick KC, Dimaano V, Wu KC, Helm RH, Weiss RG, Lima JA, Berger RD, Tomaselli GF, Bluemke DA, Halperin HR, Abraham T, Kass DA, and Lardo AC. "Cardiac magnetic resonance assessment of dyssynchrony and myocardial scar predicts function class improvement following cardiac resynchronization therapy." *JACC Cardiovasc Imaging*, 2008. **1**(5):561–568. doi:10.1016/j.jcmg.2008.04.013.

[57] Ernande L, Thibault H, Bergerot C, Moulin P, Wen H, Derumeaux G, and Croisille P. "Systolic myocardial dysfunction in patients with type 2 diabetes mellitus: identification at MR imaging with cine displacement encoding with stimulated echoes." *Radiology*, 2012. **265**(2):402–409. doi:10.1148/radiol.12112571.

[58] Pelc NJ, Sommer FG, Li KC, Brosnan TJ, Herfkens RJ, and Enzmann DR. "Quantitative magnetic resonance flow imaging." *Magnetic resonance quarterly*, 1994. **10**(3):125–47. ISSN 0899-9422.

[59] Nett EJ, Johnson KM, Frydrychowicz A, Del Rio AM, Schrauben E, Francois CJ, and Wieben O. "Four-dimensional phase contrast MRI with accelerated dual velocity encoding." *Journal of magnetic resonance imaging : JMRI*, 2012. **35**(6):1462–71. ISSN 1522-2586. doi:10.1002/jmri.23588.

[60] Simpson R, Keegan J, Gatehouse P, Hansen M, and Firmin D. "Spiral tissue phase velocity mapping in a breath-hold with non-cartesian SENSE." *Magnetic resonance in medicine : official journal of the Society of Magnetic Resonance in Medicine / Society of Magnetic Resonance in Medicine*, 2014. **72**(3):659–68. ISSN 1522-2594. doi:10.1002/mrm.24971.

[61] Delattre BMa, Heidemann RM, Crowe La, Vallée JP, and Hyacinthe JN. "Spiral demystified." *Magnetic resonance imaging*, 2010. **28**(6):862–81. ISSN 1873-5894. doi:10.1016/j.mri.2010.03.036.

[62] Fielden SW and Meyer CH. "A simple acquisition strategy to avoid off-resonance blurring in spiral imaging with redundant spiral-in/out k-space trajectories." *Magnetic resonance in medicine : official journal of the Society of Magnetic Resonance in Medicine / Society of Magnetic Resonance in Medicine*, 2015. **73**(2):704–10. ISSN 1522-2594. doi:10.1002/mrm.25172.

[63] Keegan J, Raphael CE, Parker K, Simpson RM, Strain S, de Silva R, Di Mario C, Collinson J, Stables RH, Wage R, Drivas P, Sugathapala M, Prasad SK, and Firmin DN. "Validation of high temporal resolution spiral phase velocity mapping of temporal patterns of left and right coronary artery blood flow against Doppler guidewire." *Journal of Cardiovascular Magnetic Resonance*, 2015. **17**(1):85. ISSN 1532-429X. doi:10.1186/s12968-015-0189-y.

[64] Suever JD, Wehner GJ, Haggerty CM, Jing L, Hamlet SM, Binkley CM, Kramer SP, Mattingly AC, Powell DK, Bilchick KC, Epstein FH, and Fornwalt BK. "Simplified post processing of cine DENSE cardiovascular magnetic resonance for quantification of cardiac mechanics." *Journal of cardiovascular magnetic resonance : official journal of the Society for Cardiovascular Magnetic Resonance*, 2014. **16**:94. ISSN 1532-429X. doi:10.1186/s12968-014-0094-9.

[65] Lang RM, Badano LP, Mor-Avi V, Afilalo J, Armstrong A, Ernande L, Flachskampf FA, Foster E, Goldstein SA, Kuznetsova T, Lancellotti P, Muraru D, Picard MH, Rietzschel ER, Rudski L, Spencer KT, Tsang W, and Voigt JU. "Recommendations for Cardiac Chamber Quantification by Echocardiography in Adults: An Update from the American Society of Echocardiography and the European Association of Cardiovascular Imaging." *Journal of the American Society of Echocardiography*, 2015. **28**(1):1–39.e14. ISSN 08947317. doi:10.1016/j.echo.2014.10.003.

[66] Reeder SB, Faranesh AZ, Boxerman JL, and McVeigh ER. "In vivo measurement of T2(*) and field inhomogeneity maps in the human heart at 1.5 T." *Magnetic Resonance in Medicine*, 1998. **39**(6):988–998. ISSN 07403194. doi:10.1002/mrm.1910390617.

[67] Jackson JI, Meyer CH, Nishimura DG, and Macovski A. "Selection of a convolution function for Fourier inversion using gridding." *IEEE Transactions on Medical Imaging*, 1991. **10**(3):473–478. ISSN 02780062. doi:10.1109/42.97598.

[68] Noll DC, Meyer CH, Pauly JM, Nishimura DG, and Macovski A. "A homogeneity correction method for magnetic resonance imaging with time-varying gradients." *IEEE transactions on medical imaging*, 1991. **10**(4):629–37. ISSN 0278-0062. doi:10.1109/42.108599.

[69] Moriguchi H, Dale BM, Lewin JS, and Duerk JL. "Block regional off-resonance correction (BRORC): A fast and effective deblurring method for spiral imaging." *Magnetic Resonance in Medicine*, 2003. **50**(3):643–648. ISSN 0740-3194. doi:10.1002/mrm.10570.

[70] Chen W and Meyer CH. "Semiautomatic off-resonance correction in spiral imaging." *Magnetic Resonance in Medicine*, 2008. **59**:1212–1219. ISSN 07403194. doi:10.1002/mrm.21599.

[71] Sutton BP, Noll DC, and Fessler JA. "Fast, iterative image reconstruction for MRI in the presence of field inhomogeneities." *IEEE Trans Med Imaging*, 2003. **22**(2):178–188. ISSN 02780062. doi:10.1109/TMI.2002.808360.

[72] Scott AD, Tayal U, Nielles-Vallespin S, Ferreira P, Zhong X, Epstein FH, Prasad SK, and Firmin D. "Accelerating cine DENSE using a zonal excitation." *Journal of Cardiovascular Magnetic Resonance*, 2016. **18**(Suppl 1):O50.

[73] Chen X, Yang Y, Salerno M, Meyer CH, and Epstein FH. "Accelerated cine DENSE MRI using compressed sensing and parallel imaging." *Journal of Cardiovascular Magnetic Resonance*, 2014. **16**(Suppl 1):W16. ISSN 1532-429X. doi:10.1186/1532-429X-16-S1-W16.

[74] Chen X, Yang Y, Cai X, Auger DA, Meyer CH, Salerno M, and Epstein FH. "Accelerated two-dimensional cine DENSE cardiovascular magnetic resonance using compressed sensing and parallel imaging." *Journal of Cardiovascular Magnetic Resonance*, 2016. **18**(1):38. ISSN 1532-429X. doi:10.1186/s12968-016-0253-2.

[75] Shin T, Nayak KS, Santos JM, Nishimura DG, Hu BS, and McConnell MV. "Three-dimensional first-pass myocardial perfusion MRI using a stack-of-spirals acquisition." *Magnetic resonance in medicine : official journal of the Society of Magnetic Resonance in Medicine / Society of Magnetic Resonance in Medicine*, 2013. **69**(3):839–44. ISSN 1522-2594. doi:10.1002/mrm.24303.

[76] Salerno M, Sica C, Kramer CM, and Meyer CH. "Improved first-pass spiral myocardial perfusion imaging with variable density trajectories." *Magnetic resonance in medicine*, 2013. **70**(5):1369–79. ISSN 1522-2594. doi:10.1002/mrm.24569.

[77] Feng X, Salerno M, Kramer CM, and Meyer CH. "Non-Cartesian balanced steady-state free precession pulse sequences for real-time cardiac MRI." *Magnetic resonance in medicine : official journal of the Society of Magnetic Resonance in Medicine / Society of Magnetic Resonance in Medicine*, 2015. **00**:1–10. ISSN 1522-2594. doi:10.1002/mrm.25738.

[78] Geva T, Powell aJ, Crawford EC, Chung T, and Colan SD. "Evaluation of regional differences in right ventricular systolic function by acoustic quantification echocardiography and cine magnetic resonance imaging." *Circulation*, 1998. **98**:339–345. ISSN 0009-7322. doi:10.1161/01.CIR.98.4.339.

[79] Nagao M, Yamasaki Y, Yonezawa M, Matsuo Y, Kamitani T, Yamamura K, Sakamoto I, Abe K, Kawanami S, and Honda H. "Interventricular Dyssynchrony Using Tagging Magnetic Resonance Imaging Predicts Right

Ventricular Dysfunction in Adult Congenital Heart Disease." *Congenital Heart Disease*, 2015. **10**(3):271–280. ISSN 17470803. doi:10.1111/chd.12217.

[80] Matsukubo H, Matsuura T, Endo N, Asayama J, and Watanabe T. "Echocardiographic measurement of right ventricular wall thickness. A new application of subxiphoid echocardiography." *Circulation*, 1977. **56**(2):278–84. ISSN 0009-7322. doi:10.1161/01.CIR.56.2.278.

[81] Meier GD, Bove aa, Santamore WP, and Lynch PR. "Contractile function in canine right ventricle." *The American journal of physiology*, 1980. **239**(6):H794–804. ISSN 0002-9513.

[82] Heermann P, Hedderich DM, Paul M, Schülke C, Kroeger J, Baeßler B, Wichter T, Maintz D, Waltenberger J, Heindel W, and Bunck AC. "Biventricular myocardial strain analysis in patients with arrhythmogenic right ventricular cardiomyopathy (ARVC) using cardiovascular magnetic resonance feature tracking." *Journal of Cardiovascular Magnetic Resonance*, 2014. **16**:75. ISSN 1532-429X. doi:10.1186/s12968-014-0075-z.

[83] Vigneault DM, te Riele ASJM, James CA, Zimmerman SL, Selwaness M, Murray B, Tichnell C, Tee M, Noble JA, Calkins H, Tandri H, and Bluemke DA. "Right ventricular strain by MR quantitatively identifies regional dysfunction in patients with arrhythmogenic right ventricular cardiomyopathy." *Journal of Magnetic Resonance Imaging*, 2016. **43**(5):1132–1139. ISSN 10531807. doi: 10.1002/jmri.25068.

[84] Haber I, Metaxas DN, and Axel L. "Three-dimensional motion reconstruction and analysis of the right ventricle using tagged MRI." *Medical image analysis*, 2000. **4**:335–355. ISSN 13618415. doi:10.1016/S1361-8415(00)00028-1.

[85] Kramer SP, Powell DK, Haggerty CM, Binkley CM, Mattingly AC, Cassis LA, Epstein FH, and Fornwalt BK. "Obesity reduces left ventricular strains, torsion, and synchrony in mouse models: a cine displacement encoding with stimulated echoes (DENSE) cardiovascular magnetic resonance study." *J Cardiovasc Magn Reson*, 2013. **15**:109. doi:10.1186/1532-429X-15-109.

[86] Hardy R. "Theory and applications of the multiquadric-biharmonic method 20 years of discovery 19681988." *Computers & Mathematics with Applications*, 1990. **19**(8-9):163–208. ISSN 08981221. doi:10.1016/0898-1221(90)90272-L.

[87] Haggerty CM, Kramer SP, Skrinjar O, Binkley CM, Powell DK, Mattingly AC, Epstein FH, and Fornwalt BK. "Quantification of left ventricular volumes, mass, and ejection fraction using cine displacement encoding with stimulated echoes (DENSE) MRI." *Journal of magnetic resonance imaging : JMRI*, 2014. **40**(2):398–406. ISSN 1522-2586. doi:10.1002/jmri.24350.

[88] Rüssel IK, Tecelão SR, Kuijer JPA, Heethaar RM, and Marcus JT. "Comparison of 2D and 3D calculation of left ventricular torsion

as circumferential-longitudinal shear angle using cardiovascular magnetic resonance tagging." *Journal of cardiovascular magnetic resonance : official journal of the Society for Cardiovascular Magnetic Resonance*, 2009. **11**:8. ISSN 1532-429X. doi:10.1186/1532-429X-11-8.

[89] Cerqueira MD, Weissman NJ, Dilsizian V, Jacobs AK, Kaul S, Laskey WK, Pennell DJ, Rumberger JA, Ryan T, Verani MS, and American Heart Association Writing Group on Myocardial Segmentation and Registration for Cardiac Imaging. "Standardized myocardial segmentation and nomenclature for tomographic imaging of the heart. A statement for healthcare professionals from the Cardiac Imaging Committee of the Council on Clinical Cardiology of the American Heart Association." *Circulation*, 2002. **105**(4):539–42. ISSN 1524-4539.

[90] Crane K, Weischedel C, and Wardetzky M. "Geodesics in heat." *ACM Transactions on Graphics*, 2013. **32**(5):1–11. ISSN 07300301. doi:10.1145/2516971.2516977.

[91] Jacobson A. "gptoolbox: Geometry Processing Toolbox.", 2015.

[92] Yezzi AJ and Prince JL. "An Eulerian PDE Approach for Computing Tissue Thickness." *IEEE Transactions on Medical Imaging*, 2003. **22**(10):1332–1339. ISSN 02780062. doi:10.1109/TMI.2003.817775.

[93] Suever JD, Fornwalt BK, Neuman LR, Delfino JG, Lloyd MS, and Oshinski JN. "Method to create regional mechanical dyssynchrony maps from short-axis cine steady-state free-precession images." *Journal of magnetic resonance imaging : JMRI*, 2014. **39**(4):958–65. ISSN 1522-2586. doi:10.1002/jmri.24257.

[94] Pan L, Stuber M, Kraitchman DL, Fritzges DL, Gilson WD, and Osman NF. "Real-time imaging of regional myocardial function using fast-SENC." *Magnetic Resonance in Medicine*, 2006. **55**(2):386–95. ISSN 0740-3194. doi:10.1002/mrm.20770.

[95] Zhong L, Gobeawan L, Su Y, Tan JL, Ghista D, Chua T, Tan RS, and Kassab G. "Right ventricular regional wall curvedness and area strain in patients with repaired tetralogy of Fallot." *AJP: Heart and Circulatory Physiology*, 2012. **302**:H1306–H1316. ISSN 0363-6135. doi:10.1152/ajpheart.00679.2011.

[96] Haber I, Metaxas DN, Geva T, and Axel L. "Three-dimensional systolic kinematics of the right ventricle." *Am J Physiol Heart Circ Physiol*, 2005. **289**(5):H1826–33. doi:10.1152/ajpheart.00442.2005.

[97] Hamdan A, Thouet T, Sebastian K, Paetsch I, Gebker R, Wellnhofer E, Schnackenburg B, Fahmy AS, Osman NF, and Fleck E. "Regional right ventricular function and timing of contraction in healthy volunteers evaluated by strain-encoded MRI." *Journal of Magnetic Resonance Imaging*, 2008. **28**(6):1379–1385. ISSN 10531807. doi:10.1002/jmri.21526.

[98] Fayad Za, Ferrari Va, Kraitchman DL, Young Aa, Palevsky HI, Bloomgarden DC, and Axel L. "Right ventricular regional function using MR tagging: Normals versus chronic pulmonary hypertension." *Magnetic Resonance in Medicine*, 1998. **39**:116–123. ISSN 07403194. doi:10.1002/mrm.1910390118.

[99] Massing GK and James TN. "Anatomical configuration of the His bundle and bundle branches in the human heart." *Circulation*, 1976. **53**(4):609–621. ISSN 0009-7322. doi:10.1161/01.CIR.53.4.609.

[100] Jurcut R, Giusca S, La Gerche A, Vasile S, Ginghina C, and Voigt JU. "The echocardiographic assessment of the right ventricle: what to do in 2010?" *European journal of echocardiography : the journal of the Working Group on Echocardiography of the European Society of Cardiology*, 2010. **11**(2):81–96. ISSN 1532-2114. doi:10.1093/ejechocard/jep234.

[101] Young AA, Fayad ZA, and Axel L. "Right ventricular midwall surface motion and deformation using magnetic resonance tagging." *Am J Physiol*, 1996. **271**(6 Pt 2):H2677–88.

[102] Rüssel IK, Götte MJ, Kuijer JP, and Marcus JT. "Regional assessment of left ventricular torsion by CMR tagging." *Journal of cardiovascular magnetic resonance : official journal of the Society for Cardiovascular Magnetic Resonance*, 2008. **10**:26. ISSN 1532-429X. doi:10.1186/1532-429X-10-26.

[103] Suever JD, Wehner GJ, Jing L, Powell DK, Hamlet SM, Grabau JD, Mojsejenko D, Andres KN, Haggerty CM, and Fornwalt BK. "Right Ventricular Strain, Torsion, and Dyssynchrony in Healthy Subjects Using 3D Spiral Cine DENSE Magnetic Resonance Imaging." *IEEE transactions on medical imaging*, 2017. **36**(5):1076–1085. ISSN 1558-254X. doi:10.1109/TMI.2016.2646321.

[104] Pruessmann KP, Weiger M, Scheidegger MB, and Boesiger P. "SENSE: sensitivity encoding for fast MRI." *Magnetic resonance in medicine*, 1999. **42**(5):952–62. ISSN 0740-3194.

[105] Griswold MA, Jakob PM, Heidemann RM, Nittka M, Jellus V, Wang J, Kiefer B, and Haase A. "Generalized autocalibrating partially parallel acquisitions (GRAPPA)." *Magnetic resonance in medicine*, 2002. **47**(6):1202–10. ISSN 0740-3194. doi:10.1002/mrm.10171.

[106] Lustig M and Pauly JM. "SPIRiT: Iterative self-consistent parallel imaging reconstruction from arbitrary k-space." *Magnetic Resonance in Medicine*, 2010. n/a–n/a. ISSN 07403194. doi:10.1002/mrm.22428.

[107] Lustig M, Donoho D, and Pauly JM. "Sparse MRI: The application of compressed sensing for rapid MR imaging." *Magnetic Resonance in Medicine*, 2007. **58**(6):1182–1195. ISSN 07403194. doi:10.1002/mrm.21391.

[108] Cai X, Chen X, Yang Y, Salerno M, Weller D, Meyer CH, and Epstein FH. "Free-breathing 2D Cine DENSE with Localized Excitation, Self-navigation and Motion Correction." *Journal of Cardiovascular Magnetic Resonance*, 2016. **18**(Suppl 1):P319. ISSN 1532-429X. doi:10.1186/1532-429X-18-S1-P319.

GREGORY J WEHNER

EDUCATION

University of Kentucky - Lexington KY, 2011-present
M.D. – College of Medicine (*in progress)*
Cumulative Average: 95.5%
Ph.D. – Biomedical Engineering (*in progress)*
GPA: 4.00

University of Cincinnati – Cincinnati, OH, 2006-2011
B.S. Chemical Engineering – College of Engineering
GPA: 3.99

RESEARCH POSITIONS

July 2013 – present. Full-time graduate student researcher
University of Kentucky – Cardiac Imaging Research Laboratory of B. Fornwalt

November 2012 – June 2013. Rotational researcher
University of Kentucky – Cardiac Imaging Research Laboratory of B. Fornwalt

June 2012 – September 2012. Rotational researcher
University of Kentucky – Ophthalmology Laboratory of J. Ambati

June 2011 – September 2011. Rotational researcher
University of Kentucky – Endocrinology Laboratory of P. Kern

January 2009 – May 2011. Undergraduate researcher.
University of Cincinnati – Chemical Engineering Laboratory of P. Smirniotis

INDUSTRY POSITIONS

June 2010 – September 2010. Full-time Engineering and Analytical Services Co-op.
Marathon Petroleum Company – Findlay Office Complex. Findlay, Ohio

September 2009 – June 2010. Full-time Technical Services Co-op.
Marathon Petroleum Company – Catlettsburg Refinery. Catlettsburg, Kentucky

January 2008-September 2008. Full-time Chemical Process Group Co-Op.
Duke Energy- Zimmer Power Station. Moscow, Ohio

HONORS & AWARDS

- 2014 Gill Heart scientific poster presentation award (1st of 40)
- 2014 Saha Award for Cardiovascular Research and Education (top MD/PhD)
- 2013 Gill Heart scientific poster presentation award (3rd of 40)
- 2013 Promoted with High Distinction to status of 3rd year Medical Student
- 2012 Promoted with High Distinction to status of 2nd year Medical Student
- 2011 College of Engr. Graduation Flag Bearer – highest GPA in College of Engineering
- 2006 Chemical Engineering Scholarship
- 2006 Cincinnatus Scholarship
- 2006 UC21 Designated Scholars Award – academic award: full tuition/housing
- 2006 National Merit Finalist

PUBLICATIONS

Zhang X, Liu Z-Q, Singh D, **Wehner GJ**, Powell D, Campbell K, Fornwalt B, Wenk J. Regional quantification of myocardial mechanics in rat using 3D cine DENSE cardiovascular magnetic resonance. *NMR Biomed*. May 2017. doi:10.1002/nbm.3733.

Hamlet SM, Haggerty CM, Suever JD, **Wehner GJ**, Andres KN, Powell DK, Charnigo RJ, Fornwalt BK. Using a respiratory navigator significantly reduces variability when quantifying left ventricular torsion with cardiovascular magnetic resonance. J Cardiovasc Magn Reson. 2017; 19(1):25. PMCID: PMC5331707.

Suever JD, **Wehner GJ**, Jing L, Powell DK, Hamlet SM, Grabau JD, Mojsejenko D, Andres KN, Haggerty CM, Fornwalt BK. Right Ventricular Strain, Torsion, and Dyssynchrony in Healthy Subjects using 3D Spiral Cine DENSE Magnetic Resonance Imaging. IEEE Trans Med Imaging. In press.

Hamlet SM, Haggerty CM, Suever JD, **Wehner GJ**, Grabau JD, Andres KN, Vandsburger MH, Powell DK, Sorrell VL, Fornwalt BK. An interactive videogame designed to improve respiratory navigator efficiency in children undergoing cardiovascular magnetic resonance. J Cardiovasc Magn Reson. 2016;18:54. PMCID: PMC5012042.

Jing L, **Wehner GJ**, Suever JD, Charnigo RJ, Alhadad S, Stearns E, Mojsejenko D, Haggerty CM, Hickey K, Valente AM, Geva T, Powell AJ, Fornwalt BK. Left and right ventricular dyssynchrony and strains from cardiovascular magnetic resonance feature tracking do not predict deterioration of ventricular function in patients with repaired tetralogy of Fallot. J Cardiovasc Magn Reson. 2016;18. PMCID: PMC4993000.

Hamlet SM, Haggerty CM, Suever JD, **Wehner GJ**, Andres KN, Powell DK, Zhong X, Fornwalt BK. Optimal configuration of respiratory navigator gating for the quantification of left ventricular strain using spiral cine displacement encoding with stimulated echoes (DENSE) MRI. J Magn Reson Imaging. 2017;45:786–794. PMCID: PMC5269554.

Jing L, Binkley CM, Suever JD, Umasankar N, Haggerty CM, Rich J, Nevius CD, **Wehner GJ**, Hamlet SM, Powell DK, Radulescu A, Kirchner HL, Epstein FH, Fornwalt BK. Cardiac remodeling and dysfunction in childhood obesity: a cardiovascular magnetic resonance study. J Cardiovasc Magn Reson. 2016;18:28. PMCID: PMC27165194.

Wehner GJ, Grabau JD, Suever JD, Haggerty CM, Jing L, Powell DK, Hamlet SM, Vandsburger MH, Zhong X, Fornwalt BK. 2D cine DENSE with low encoding frequencies accurately

quantifies cardiac mechanics with improved image characteristics. J Cardiovasc Magn Reson. 2015;17:93. PMCID: PMC4634910.

Wehner GJ, Suever JD, Haggerty CM, Jing L, Powell DK, Hamlet SM, Grabau JD, Mojsejenko WD, Zhong X, Epstein FH, Fornwalt BK. Validation of in vivo 2D displacements from spiral cine DENSE at 3T. J Cardiovasc Magn Reson. 2015;17:5. PMCID: PMC4311418.

Suever JD, **Wehner GJ**, Haggerty CM, Jing L, Hamlet SM, Binkley CM, Kramer SP, Mattingly AC, Powell DK, Bilchick KC, Epstein FH, Fornwalt BK. Simplified post processing of cine DENSE cardiovascular magnetic resonance for quantification of cardiac mechanics. J Cardiovasc Magn Reson. 2014;16:94. PMCID: PMC4246464.

ABSTRACTS (National/International, First Author)

Wehner GJ, Haggerty, CM, Suever, JD, Jing, L, Leader, JB, Kirchner, HL, Manus, JNA, Good, CW, Fornwalt, BK, "Redefining Normal Left Ventricular Systolic Function Based on Outcomes Using Nearly 20 Years of Data from a Large Regional Health System", *Submitted to* ASE Scientific Sessions, June 2017

Wehner GJ, Haggerty CM, Suever JD, Jing L, Leader JB, Fornwalt BK, "Prediction of all-cause mortality from clinical CMR-derived left ventricular ejection fraction: 15 years of data from a large regional health system", Society of Cardiovascular Magnetic Resonance Scientific Sessions, Washington, DC, January 2017.

Wehner GJ, Suever JD, Fielden SW, Powell DK, Hamlet SM, Vandsburger MH, Haggerty CM, Zhong X, Fornwalt BK, "Typical Readout Durations in Spiral Cine DENSE Produce Blurred Images and Underestimate Radial Strain at Both 3.0T and 1.5T", Society of Cardiovascular Magnetic Resonance Scientific Sessions, Washington, DC, January 2017.

Wehner GJ, Suever, JD, Haggerty, CM, Jing, L, Powell, DK, Hamlet, SM, Grabau, JD, Mojsejenko, D, Zhong, X, Epstein, FH, Fornwalt, BK, "New Method to Validate in vivo 2D Displacements from Spiral Cine DENSE at 3T", ISMRM, Toronto, Ontario, Canada, May 2015.

Wehner, GJ, Suever, JD, Haggerty, CM, Jing, L., Powell, DK, Hamlet, SM, Grabau, JD, Mojesejenko, D, Zhong, X, Epstein, FH, Fornwalt, BK. "Validation of *in vivo* 2D Displacements from Spiral Cine DENSE at 3T". Society of Cardiovascular Magnetic Resonance Scientific Sessions, Nice, France, February 2015.

Wehner, GJ, Suever, JD, Haggerty, CM, Jing, L, Powell, DK, Zhong, X, Epstein FH, Fornwalt, BK, "High Resolution Cine Displacement Encoding with Stimulated Echoes (DENSE) at 3T with Navigator Feedback for Quantification of Cardiac Mechanics," Society of Cardiovascular Magnetic Resonance Scientific Sessions, New Orleans, LA, January 2014.

Wehner, GJ, Ayoob, A., *et al.* "Identification and Management of Blunt Traumatic Bowel and Mesenteric Injury: Surgical or Nonsurgical Injury". *RSNA Annual Meeting 2012*. Chicago, IL. November 2012

ABSTRACTS (National/International, Co-Author)

Suever JD, **Wehner GJ**, Jing L, Hamlet SM, Haggerty CM, Fornwalt BK, "Polar Processing of Cine Displacement Encoding with Stimulated Echoes (DENSE) Data Provides More Accurate Quantification of Cardiac Mechanics than Traditional Cartesian Analysis", Society of Cardiovascular Magnetic Resonance Scientific Sessions, Washington, DC, January 2017.

Pulenthiran AA, Jing L, Suever JD, **Wehner GJ**, Nevius CD, Mejia-Spiegeler A, Haggerty CM, Fornwalt BK, "Right Ventricular Strain from Displacement Encoding with Stimulated

Echoes CMR is reduced in Overweight and Obese Children", Society of Cardiovascular Magnetic Resonance Scientific Sessions, Washington, DC, January 2017.

Jing L, Nevius CD, Friday CM, Suever JD, Mejia-Spiegeler A, **Wehner GJ**, Chishti AS, Haggerty CM, Fornwalt BK, "Association of ambulatory blood pressure and insulin resistance with cardiac remodeling in obese children", Society of Cardiovascular Magnetic Resonance Scientific Sessions, Washington, DC, January 2017.

Hamlet SM, Haggerty CM, Suever JD, **Wehner GJ**, Andres KN, Powell DK, Charnigo RJ, Fornwalt BK, "Using a Respiratory Navigator Significantly Reduces Variability when Quantifying Left Ventricular Torsion from CMR", Society of Cardiovascular Magnetic Resonance Scientific Sessions, Washington, DC, January 2017.

Haggerty CM, Mejia-Spiegeler A, Suever JD, **Wehner GJ**, Charnigo RJ, Fornwalt BK, Fogel MA, "Associations Between Myocardial T1-Mapping and Left Ventricular Strain, Strain Rate, and Dyssynchrony in Patients with Repaired Tetralogy of Fallot", Society of Cardiovascular Magnetic Resonance Scientific Sessions, Washington, DC, January 2017.

Haggerty CM, Mejia-Spiegeler, A, Suever, JD, **Wehner, GW**, Kim, E, Fornwalt, BK, Fogel, MA, "Association Between Myocardial T1-Mapping and Left Ventricular Mechanics in Patients With Repaired Tetralogy of Fallot", AHA Scientific Sessions, New Orleans, Louisiana, November 2016. Circulation. 2016;134:A19670

Suever JD, **Wehner GJ**, Haggerty CM, Jing L, Powell DK, Hamlet SM, Grabau JD, Mojsejenko D, Andres KN, Vandsburger MH, Fornwalt BK, "Right ventricular strain, torsion and synchrony in healthy subjects using 3D spiral cine DENSE", Society of Cardiovascular Magnetic Resonance Scientific Sessions, Los Angeles, California, January 2016.

Hamlet SM, Suever JD, Grabau JD, **Wehner GJ**, Vandsburger MH, Andres KN, Powell DK, Sorrell VL, Fornwalt BK, "An interactive videogame designed to optimize respiratory navigator efficiency in children undergoing cardiac magnetic resonance", Society of Cardiovascular Magnetic Resonance Scientific Sessions, Los Angeles, California, January 2016.

Haggerty CM, Feindt JA, Mojsejenko D, **Wehner GJ**, Suever JD, Fogel MA, Fornwalt BK, "Differences in left ventricular strain measurements between cine DENSE cardiac magnetic resonance and SSFP feature tracking", Society of Cardiovascular Magnetic Resonance Scientific Sessions, Los Angeles, California, January 2016.

Jing, L, Friday, CM, Suever, JD, Umasankar, N, Haggerty, CM, **Wehner, GJ**, Hamlet, SM, Powell, DK, Radulescu, A, Kirchner, HL, Epstein, FH, Fornwalt, BK, "Obese Children With Concentric Hypertrophy and Impaired Cardiac Strain: A Potentially High-risk Subgroup Identified With Cardiac Magnetic Resonance", AHA Scientific Sessions, Orlando, Florida, November 2015. Circulation. 2015;132:A15439

Hamlet SM, Andres K, **Wehner GJ**, Suever JD, Powell DK, Zhong X ,Epstein FH, Fornwalt BK, "The effect of respiratory gating strategy on left ventricular cardiac strains with DENSE", Society of Cardiovascular Magnetic Resonance Scientific Sessions, Nice, France, February 2015.

Hamlet SM, Andres K, **Wehner GJ**, Suever JD, Powell DK, Zhong X, Epstein FH, Fornwalt BK, "Patient-specific variability in breath-hold positions during cardiac magnetic resonance imaging has a negligible effect on measures of cardiac mechanics", Society of Cardiovascular Magnetic Resonance Scientific Sessions, Nice, France, February 2015.

Grabau JD, **Wehner GJ**, Suever JD, Haggerty CM, Jing L, Powell DK, Hamlet SM, Zhong X, Epstein FH, Fornwalt BK, "Low encoding frequencies accurately quantify cardiac mechanics while minimizing phase wrapping in 2D cine DENSE with through-plane dephasing", Society of Cardiovascular Magnetic Resonance Scientific Sessions, Nice, France, February 2015.

Binkley CM, Jing L, Suever JD, Umasankar N, **Wehner GJ**, Hamlet SM, Powell DK, Radulescu A, Epstein FH, Fornwalt BK, "Children with obesity have cardiac remodeling and

dysfunction: a cine DENSE magnetic resonance imaging study", Society of Cardiovascular Magnetic Resonance Scientific Sessions, Nice, France, February 2015.

Suever, JD, **Wehner, GJ**, Jing, L., Powell, D., Haggerty, CM, Zhong, X., Epstein F.H., Fornwalt, B.K., "Two-Dimensional Estimates of Left Ventricular Strains are Significantly Affected by Through-plane Motion," Society of Cardiovascular Magnetic Resonance Scientific Sessions, New Orleans, LA, January 2014.

Suever, JD, **Wehner, GJ**, Jing, L., Powell, D., Haggerty, CM, Zhong, X., Epstein F.H., Fornwalt, B.K., "Quantification of Right Ventricular Function from Short-Axis Displacement-Encoded Images," Society of Cardiovascular Magnetic Resonance Scientific Sessions, New Orleans, LA, January 2014.

Hamlet, SM, **Wehner, GJ**, Suever, JD, Powell, DK, Haggerty, CM, Jing, L., Zhong, X., Epstein F.H., Fornwalt, B.K., "Effect of Variable Breath-hold Positions During Cardiac Magnetic Resonance on Measures of Left Ventricular Mechanics," Society of Cardiovascular Magnetic Resonance Scientific Sessions, New Orleans, LA, January 2014.

ABSTRACTS (Local, First Author)

Wehner GJ, Suever, JD, Powell, DK, Hamlet, SM, Vandsburger, MV, Haggerty, CM, Fornwalt, BK, "Off-resonance distorts images, corrupts displacement measurements, and alters quantifications of cardiac strains in 2D spiral cine DENSE MRI at 3T and 1.5T", University of Kentucky AOA-MD/PhD Research Day. Lexington, KY. February 2016

Wehner GJ, Suever, JD, Haggerty, CM, Jing, L, Powell, DK, Hamlet, SM, Grabau, JD, Mojsejenko, D, Zhong, X, Epstein, FH, Fornwalt, BK, "Validation of in vivo Cardiac Motion from Spiral Cine DENSE MRI at 3 Tesla", University of Kentucky AOA-MD/PhD Research Day. Lexington, KY. February 2015

Wehner GJ, Suever, JD, Haggerty, CM, Jing, L, Powell, DK, Hamlet, SM, Grabau, JD, Mojsejenko, D, Xiaodong, Z, Esptein, FH, Fornwalt, BK, "Validation of in vivo Myocardial Displacements from Spiral Cine DENSE MRI at 3T", Saha Cardiovascular Research Day, Lexington, KY, October, 2014

Wehner GJ, Suever, JD, Haggerty CM, Jing, L, Powell, DK, Zhong, X, Esptein, FH, Fornwalt, BK, "High resolution magnetic resonance imaging of cardiac motion and mechanics in humans", University of Kentucky AOA-MD/PhD Research Day. Lexington, KY. February 2014

Wehner, GJ., Gelfand, B., Ambati, J. "Free iron increases the stability of toxic *Alu* RNA transcripts". University of Kentucky AOA-MD/PhD Research Day. Lexington, KY. February 2013